Modelling vesicle dynamics in extended geometries and in micro-fluidic devices

Badr Kaoui

UNIVERSITÉ JOSEPH FOURIER - GRENOBLE I
UNIVERSITÉ HASSAN II - MOHAMMEDIA - CASABLANCA II

THÈSE

pour obtenir le grade de

Docteur de l'UNIVERSITÉ JOSEPH FOURIER - GRENOBLE I
et de l'UNIVERSITÉ HASSAN II - MOHAMMEDIA - CASABLANCA II

Spécialité : Physique pour les sciences du vivant
préparée au Laboratoire de Spectrométrie Physique
dans le cadre de l'École Doctorale de physique
présentée et soutenue publiquement
par

Badr Kaoui

le 7 juillet 2009

Titre:

Modelling vesicle dynamics in extended geometries and in micro-fluidic devices

Modélisation de vésicules en géométrie étendue et dans des systèmes micro-fluidiques

Jury

M. Jacques Prost	Président du jury
M. Abdelilah Benyoussef	Rapporteur
M. Walter Zimmermann	Rapporteur
M. Gerhard Gompper	Examinateur
M. Emmanuel Maître	Examinateur
Mme Miglena Angelova	Examinatrice
M. Chaouqi Misbah	Directeur de thèse
M. Yahia Boughaleb	Co-directeur de thèse

Modelling vesicle dynamics in extended geometries and in micro-fluidic devices

Badr KAOUI

I dedicate this thesis to my family,
my friends
and all the people
who helped me to achieve this work

Modelling vesicle dynamics in extended geometries and in micro-fluidic devices

Badr KAOUI

July 7$^{\text{th}}$, 2009

ABSTRACT

Dynamical behavior and deformation of a single neutrally buoyant suspended vesicle (a closed phospholipid membrane), as a response to external applied flows (simple shear and Poiseuille flows), is studied in the limit of small Reynolds numbers. Unbounded and confined geometries are both considered here. For this purpose we use three-dimensional analytical calculation (small deformation theory) as well as two-dimensional simulations (lattice-Boltzmann and boundary integral methods) to solve the corresponding hydrodynamical equations and to track explicitly the vesicle dynamics.

The small deformation theory is used to draw the phase-diagram summarizing the known vesicle dynamical regimes (tank-treading, tumbling and vacillating-breathing), under shear flow. Impact of varying controlling parameters on the evolution of various quantities characterizing each vesicle dynamical regime is reported.

We present also how we adapted the lattice Boltzmann method to simulate dynamics of vesicles in confined geometries (e.g. a micro-channel). As benchmarkings, the vesicle equilibrium shapes in a fluid at rest are recovered together with dynamical behavior of a vesicle under simple shear flow - tank-treading -. The effect of confinement on the vesicle dynamics is investigated.

Lateral migration of a vesicle placed in unbounded and semi-bounded Poiseuille flow is investigated using the boundary integral method simulations. In the unbounded geometry we find that the nonlinear character of the Poiseuille flow, together with the vesicle deformability, causes a lateral migration of the vesicles towards the flow centerline. In the presence of a bounding wall an additional lift force appears. In this situation we investigate the interplay between the wall- and the Poiseuille flow curvature- induced lift forces. A similarity law for the lateral migration velocity (as a function of relevant structural and flow parameters) that is consistent with experimental results is proposed.

Key words: Membranes, vesicles, complex fluids, Stokes flow, simple shear flow, Poiseuille flow, modelling, simulation, non linear dynamics, blood rheology, lateral migration, microfluidic.

RÉSUMÉ

La déformation et le comportement dynamique d'une vésicule sous l'action d'un écoulement externe appliqué (cisaillement simple et Poiseuille) est étudié dans la limite de faibles nombres de Reynolds. Les cas de géométries non-confinée et confinée sont considérés.

On fait usage de plusieurs méthodes: (i) un calcul analytique tridimensionnelle (théorie de faible déformation) (ii) des simulations bidimensionelle (méthodes de Boltzmann sur réseau et intégrale de frontière) dans le but de résoudre les équations hydrodynamiques correspondantes et de suivre explicitement la dynamique de la vésicule.

La théorie analytique de faible déformation est utilisée pour construire le diagramme de phase résumant tous les régimes dynamiques connus pour une vésicule (chenille de char, bascule et vacillation-respiration) sous un écoulement de cisaillement. L'impacte de la variation des paramètres, contrôlant la dynamique, sur l'évolution de différentes quantités caractérisant chaque régime dynamique d'une vésicule est présenté. On utilise également la méthode de Boltzmann sur réseau afin de simuler la dynamique d'une vésicule dans une géométrie confinée (e.g. un micro-canal). Comme cas test, les formes d'équilibre d'une vésicule et son mouvement de chenille de char sous cisaillement ont été analysés. L'effet du confinement sur la dynamique de la vésicule a été examiné. La migration latérale d'une vésicule placée dans un écoulement de Poiseuille non-confiné et semi-confiné est traité en utilisant des simulations basées sur la méthode d'intégrale de frontière. Pour le cas de la géométrie non-confinée, on a trouvé que le caractère non linéaire de l'écoulement de Poiseuille combiné à la déformabilité de la vésicule, induit une migration latérale des vésicules vers le centre de l'écoulement. La présence d'une paroi délimitant le fluide externe induit également une force de portance. On a analysé la compétition entre la force de portance due à la paroi et celle du la courbure de l'écoulement de Poiseuille. Une loi donnant la vitesse de migration latérale (en fonction des paramètres caractérisant la vésicule et l'écoulement) est proposée et est en accord avec les résultats expérimentaux .

Mots clés: Membranes, vésicules, fluides complexes, écoulement de Stokes, écoulement de cisaillement simple, écoulement de Poiseuille, modélisation, simulation, dynamique non linéaire, rhéologie du sang, migration latérale, micro-fluidique

CONTENTS

1. A BRIEF SUMMARY ON MAIN PROPERTIES OF DEFORMABLE PARTICLES

1.1 Deformable particles

By the term *deformable particles* we mean all kinds of suspending particles with ability to change their shape when they are subject to external applied forces, mainly hydrodynamical stresses due to their suspending fluid flow.

Among the known classical deformable particle is a *droplet*, that has been extensively studied in literature a long time ago, its wetting on a substrate [1], its deformation and break-up under shear flow [2]. There are other biological and artificial deformable particles that have also attracted the interest of scientists and engineers. An old biological system that fascinated scientists and in particular physicians is the *red blood cell*. A considerable literature has been devoted to this topic. Artificial deformable particles such as *capsules* or *vesicles* emerged in the recent decades and have attracted several scientific communities [3–5]. This is due partly to the simplicity and the ability of these models to reproduce some dynamical behaviors observed for living cells (such as red blood cells) together with the interest in exploiting them in the pharmaceutical industry as drug delivery carriers (carrying and releasing a drug in a targeted specific site in the human body).

Understanding the dynamical behavior (orientation, deformation and migration) of such deformable entities in a flow (e.g. shear flow or Poiseuille flow), presents both fundamental (a non trivial out-of-equilibrium and non-linear system) and biomedical engineering interests. Not only is the biomedical interest motivated by in vivo questions (like understanding blood rheology), but also in vitro understanding has become an increasing demand in the lab-on-chip technologies. Indeed, the advent of microfluidic devices and their abilities to sort out and separate entities based on their mechanical properties (size, deformability, encapsulated fluid...etc) [6–8] are regarded as promising tools in medical diagnostic research (Fig. 1.1). Thus the understanding of transport properties of deformable particles has known an upsurge of interest in recent years.

Below a very brief description of the structure and properties of each

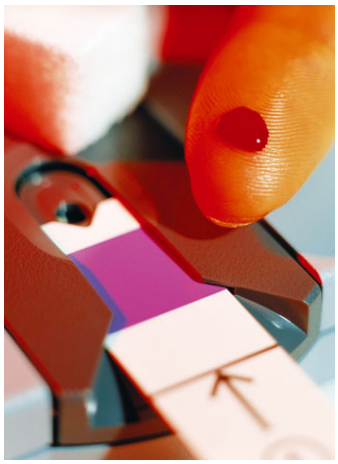

Fig. 1.1: A lab-on-chip makes it possible to quickly perform medical diagnostic on a drop of blood. Picture taken form the CNRS web site: *http://www2.cnrs.fr/*

above cited deformable particle is given. For the vesicle system, an entire chapter is dedicated to it since it is the subject of interest of the present thesis.

Droplet

It is an amount of a liquid immersed in another fluid matrix of different nature and immiscible with the suspended liquid drop. The fluid matrix can be another liquid or a gas (air for example). The liquid droplet and the suspending fluid are separated by an interface that changes its shape depending on the condition of the forces exerted upon it. A free isolated droplet has a spherical equilibrium shape.

Red blood cell

Red blood cells (RBCs) constitute the major component of the blood, about 45% in a given volume of the whole human blood, while white blood cells and platelets occupy less than 1%. The rest is filled with plasma (the large part of it is water). RBCs are among the simplest living cells in the human organism, since they are devoid of a nucleus and organelles. A RBC consists of a closed phospholipid membrane enclosing a hemoglobin solution (a newtonian fluid) and it is suspended in the blood plasma. A two-dimensional cytoskeleton network is sticked to the membrane (called spectrin network). Under physiological conditions a healthy red blood cell has a biconcave shape

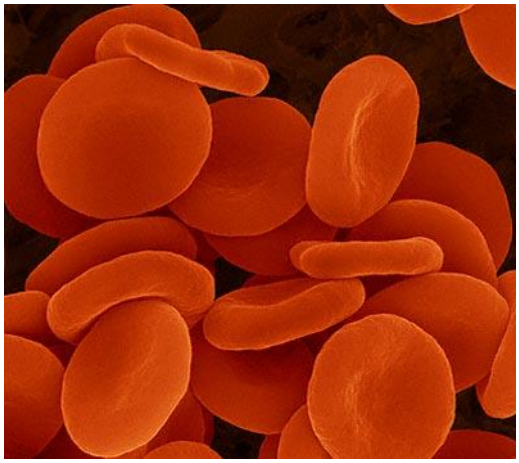

Fig. 1.2: A scanning electron micrograph of red blood cells

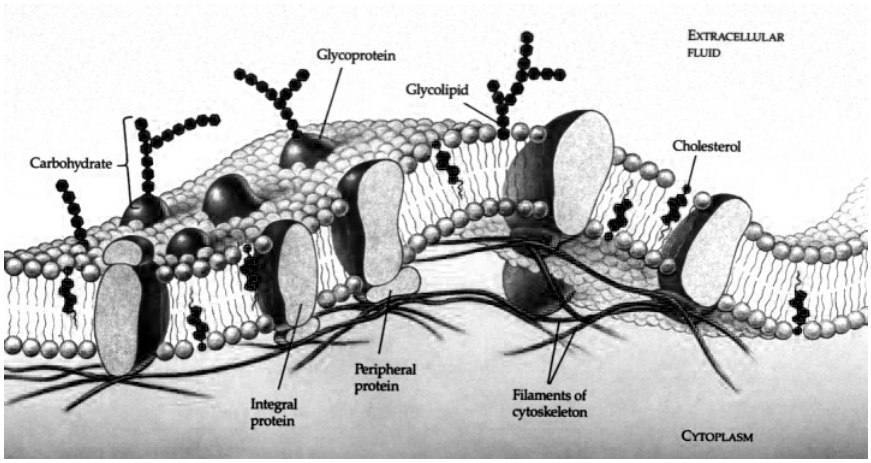

Fig. 1.3: Cartoon presenting the components of which a red blood cell membrane is made.

(see Figure 1.2) with a size of about $8\mu m$ and a thickness of about $2\mu m$ (see Figure 1.3 for the complex structure of the red blood cell membrane). Its has a life time of about 120 days during which its task consists in transporting and delivering oxygen to living tissues.

Vesicle

Vesicles are closed lipid membranes, encapsulating internal substances and are usually suspended in another external aqueous solution (Fig. 1.4). Their typical diameter varies from some dozen of nanometres to hundreds of micrometers. For example vesicles which are present inside the cytoplasm of real cells (and which have transport functions of substances such as protein) are quite small in size, typically of the order of $100nm$. While vesicles made and studied experimentally (in our group) are quite large in size, typically 10 - $100\mu m$, and are called Giant unilamellar vesicles (GUV). We will be interested in this system in this thesis, albeit we shall often use simply the denomination vesicles. Vesicles may be viewed as a first approximation to red blood cell (they are somehow red blood cells without cytoskeleton network and having a membrane made mainly and only of phospholipid molecules). Despite the simplicity of the structure of vesicles compared to the red blood cells one, many features observed for RBCs were also observed for vesicles. The known biconcave shape of RBCs as well as their dynamical behaviour under flow can be reproduced by the vesicles model as it will be shown in the present thesis. Vesicles, like RBCs, have a conserved volume (due to the fact that the enclosed fluid is incompressible) and a conserved surface (the membrane is a two dimensional incompressible fluid) under certain conditions. We shall back later to a more precise discussion of these notions.

Capsule

Capsules are closed hyper-elastic polymeric shell. Like vesicles, capsules are used to enclose an internal fluid and are suspended in an other fluid. However, due to the elasticity of their shell, their surface is not a conserved quantity. This marks a difference with vesicles and RBCs.

1.2 Complex fluids

In recent decades considerable research has been dedicated to understand the mechanical behaviors of deformable particle suspensions (we talk about *emulsion* for the case of many droplets) at both microscopic and macroscopic levels. In most cases the ultimate desire is to account for the observable

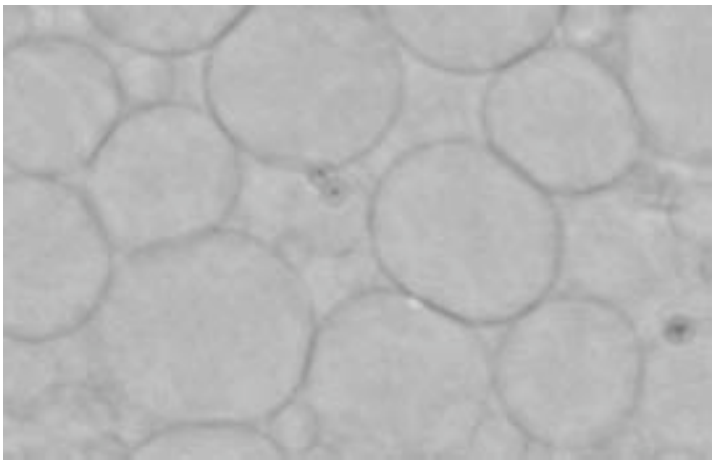

Fig. 1.4: A phase-contrast micrpgraph of vesicles

macroscopic behavior of such systems (rheology) based on what happens at the micro-scale, i.e. at the level of each single particle (orientation, deformation and migration, and so on..). The deformable particles together with their suspending fluid constitute what we call a *complex fluid*. It is a class of fluids for which the classical existing models of continuum mechanics are not sufficient to describe the complex mechanical behaviors exhibited by such fluids when they are subject to stresses. They can, for example, switch from a fluid- to a solid-like behavior by increasing the strength of the applied stresses. There exists to date no universal law (if any) for complex fluids. The ultimate law should in principle emerge from understanding of micro/macro link of the considered fluid. This is why it is essential to understand microscopic dynamics before dealing with rheology, as will be documented in this thesis.

1.3 Microfluidic devices

Microfluidic devices are small devices consisting of a labyrinth of channels with dimension of tens to hundreds of micrometers. Designed to manipulate small amount of fluids (10^{-9} to 10^{-18} liters) [9, 10]. The idea is to perform chemical reactions in such devices in order to decrease the costs by using inexpensive devices (small sized circuits made of cheap materials like PDMS) and very small quantities of reactions (that are maybe hard to acquire or toxic and need to be handled carefully [11]). Another promising application of microfluidc devices to which we would like to contribute in this thesis, is to separate and sort-out deformable particles based on their size, deformability

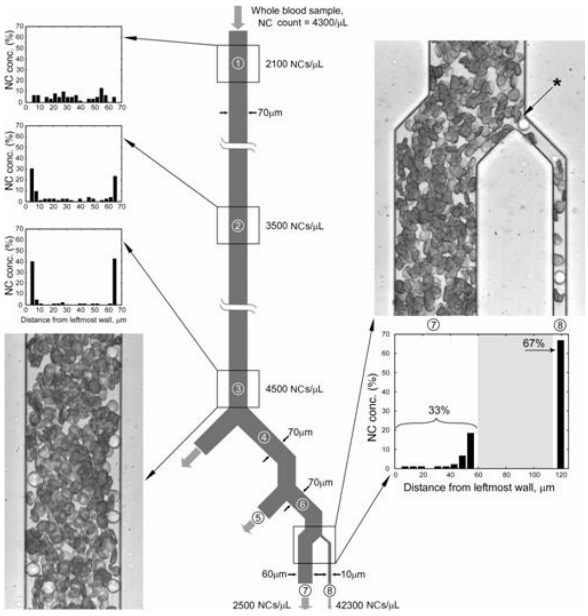

Fig. 1.5: A microfluidic devices desgined to separate WBCs from a whole blood sample [6].

and their enclosed fluid. Figure 1.5 shows a microfluidic device designed to separate white blood cells from a whole blood sample based on the mechanical properties of the WBCs. In this device the trick used is that WBCs and RBCs have different degrees of deformability, a RBC is more deformable than a WBC.

1.4 Contribution of the present thesis

Vesicles dynamics under an external applied simple shear flow has been the subject of extensive studies, both in unbounded geometries [12–17] as well as in the presence of a bounding wall [18–22]. In order to identify without ambiguity the real contribution of the present work, we have felt it worthwhile to list the main contributions achieved during the past three years during this Phd work.

First contribution

For the unbounded geometries, it is known that vesicles under shear flow exhibit three different types of dynamical regimes:

- *Tank-treading* (steady inclination angle and fixed shape, while the fluid membrane undergoes a tank-tread like motion),

- *Vacillating-breathing* (oscillation around the flow direction, while the shape undergoes large deformations),
- *Tumbling* (flipping like a rigid body albeit a certain degree of membrane tank-treading is preserved). This flipping pay occur in the shear plane, or in a plane inclined with respect to shear.

Which dynamical mode prevails over the others depends on a set of three dimensionless parameters:

- The *excess area* (the vesicle's degree of deflation),
- The *viscosity contrast* (between the enclosed and the suspending fluids),
- The *capillary number* (ratio between the flow characteristic time scale over that needed for the vesicle to relax to its equilibrium shape after cessation of flow (this time depends on membrane rigidity)).

In the present thesis we make use of the dynamical equations, describing the evolution in time of the vesicle orientation and its shape deformation, derived in [23] for the higher order expansion of the small deformation theory reported in [17] (i.e. for a shape close enough to a sphere). A phase-diagram including the three mentioned vesicle dynamical regimes, in terms of the viscosity contrast and the capillary number, is drawn. The location of the borders, separating between the three dynamical regimes in our phase-diagram, differs from the one reported in [24] since in [23] the hydrodynamical problem is solved consistently up to higher order. We complete this phase-diagram by bringing additional information associated to each dynamical regime. More precisely, we investigate how varying one parameter, while keeping the two others fixed, affects various physical quantities:

- The steady inclination angle for the tank-treading regime,
- The amplitude and the period of oscillation as well as the shape deformation for the vacillating breathing regime,
- The period of the flipping for the tumbling regime.

Emphasis is put on the vacillating-breathing mode (VB), which is less known than the two other regimes, namely tank-treading (TT) and tumbling regimes (TB). There are only few experimental papers in literature in which vacillating-breathing is briefly discussed [14, 16]. It seems that an early experimental discovery of the VB mode has been overlooked in the literature. This is due to de Haas et al. [25] where a quite clear discussion of this mode was reported. Quite recently an experimental determination of the phase-diagram

has been reported [26], and these results are discussed in the light of the present study. Here, importance is payed to quantifying this regime and analyzing how associated physical quantities evolve with relevant parameters. The major goal is to have a complete analysis at our disposal with the aim of guiding future experiments.

Second contribution

For the wall bounded geometry, only the situation of a vesicle under shear flow placed initially near (or adhered to) a substrate has been considered so far [18–21, 27]. These studies revealed that the presence of a wall induces a lift force upon the vesicle even in the Stokes limit (see the discussion below). However these studies have not treated yet an important effect, namely the effects of *degree of confinement* (ratio between the vesicle size and the width of the channel) on the vesicle dynamics and its rheology under shear flow. We have decided in order to treat this situation to make use of the lattice-Boltzmann method (LBM) simulation. This method is quite versatile and it allows us to explore quite naturally complex geometries (like bifurcations, for examples). In the present thesis we expose how we achieved the vesicle dynamics and fluid flow coupling in the framework of this method. Preliminary results concerning dynamics and rheology of confined tank-treading vesicle are reported, namely:

- How the steady-inclination angle and vesicle membrane tank-treading velocity is affected by the degree of confinement.
- The hydrodynamical stresses exerted by the external fluid, in the presence of the vesicle, on the bounding walls as a function of the vesicle reduced volume and the degree of confinement,
- The pressure field and the streamlines inside and outside the vesicle when it undergoes tank-treading motion in confined channel,
- Measuring the effective viscosity of the composite fluid for different values of the vesicle reduced volume and degree of confinement.

The LBM method is now being used for different situations, and opens a promising avenue for studies of concentrated suspensions.

Third contribution

A vesicle placed in an unbounded fluid subject to simple shear (in the Stokes limit) does not exhibit a lateral migration with respect to the flow direction.

If the suspended fluid is bounded by a wall, then this leads to breaking of the translational symmetry perpendicular to the flow direction as well as the upstream-downstream symmetry. As a consequence a tank-treading vesicle migrates away from the wall. This viscous lift force is caused by the flow induced fore-aft symmetry breaking of the vesicle shape [19]. In the present thesis we found that even in unbounded geometry (no bounding walls) a vesicle can exhibit lateral migration, perpendicular to the flow direction, when subject to a Poiseuille flow. The deformability of the vesicle and the non linear character of the Poiseuille velocity profile (non uniform shear rate) cause the lateral migration of a vesicle towards the Poiseuille flow center-line. Studies have been performed on the vesicle dynamics in Poiseuille flow [28–31] but these concern vesicles flowing in small capillaries with no ability to observe such lateral migration since the size of the vesicle is of the same order as the width of the capillaries. In the present thesis we report how the vesicle shape deforms during the lateral migration until reaching the Poiseuille flow center-line. A tentative to extract a law for the vesicle lateral migration in unbounded Poiseuille flow is also reported.

Fourth contribution

The last contribution of the present thesis is to study the interplay between the Poiseuille flow- and the wall-induced lift forces. For this purpose we performed boundary integral method simulation in a semi-infinite fluid bound by a wall. We identify regimes where one mechanism (either wall-induced or curvature-induced lift force) dominates over the other. Simulations data in the case of larger distances from the wall to the Poiseuille center-line are used to derive a similarity law for the vesicle lateral migration velocity as a function of the flow parameters and intrinsic properties of the vesicle. This law is then used to fit experimental data. A good agreement is found between simulations and experiments.

2. VESICE MODEL AND HYDRODYNAMICAL EQUATIONS

Here we describe in more details the system of *vesicle* whose dynamics under flow is studied along the present thesis. First we present the vesicle, its structure, what is made of and its mechanical properties. Then we present its mathematical description and the equations governing the flow of both its internal and external fluids, together with the boundary conditions at the membrane.

2.1 What is a vesicle?

Vesicles are closed lipid membranes, encapsulating an internal fluid and are usually suspended in an external aqueous solution. Thier typical size ranges from the order of $100nm$ to the order of $10\mu m$. In the latter case we call them *Giant unilamellar vesicles* (GUV). Figure 2.1 shows a phase-contrast micrograph of a vesicle.

The membrane of vesicles can be made of phospholipid molecules. Each molecule has a hydrophilic phosphate head (polar) and two hydrophobic fatty acid tails (non polar), see Fig. 2.2. In our experiments two types of phospholipids molecules are commonly used, the dioleoyl-phosphatidilcholine (DOPC) or the dimyristoyl-phosphatidylcholine (DMPC).

For a vesicle with a given radius of about $10\mu m$, the membrane contains about 10^{10} molecules. These phospholipid molecules, when hydrated, assemble themselves spontaneously into a bilayer (with a thickness of the order of $5nm$) in which all the hydrophilic heads of the molecules are in contact either with the internal or the external aqueous solutions, as it is depicted in Fig. 2.2.

Vesicles are widely used as a mimicking model to study biological cells. They can be artificially produced in the laboratory and they can be easily handled compared to the living cells that need much more precaution and care. Vesicles have shown many features observed for living cells. As a way of example, the known biconcave equilibrium shapes of red blood cells, as well as and several of their dynamics under flow are also exhibited by vesicles, as

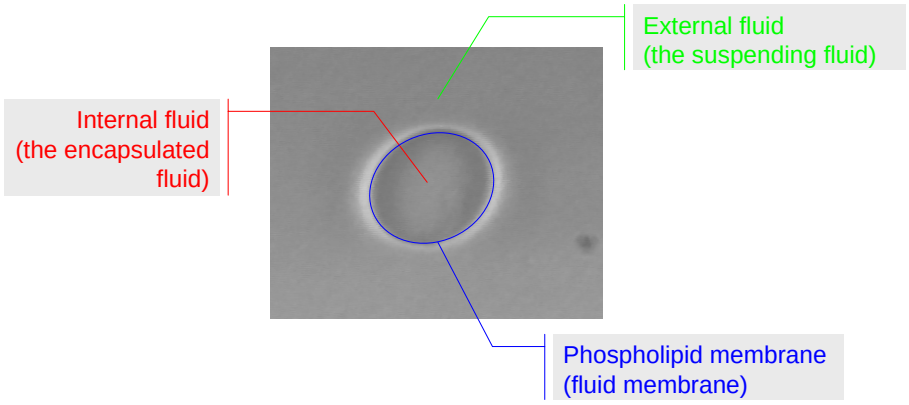

Fig. 2.1: A phase-contrast micrograph of a vesicle with a size of $50\mu m$.

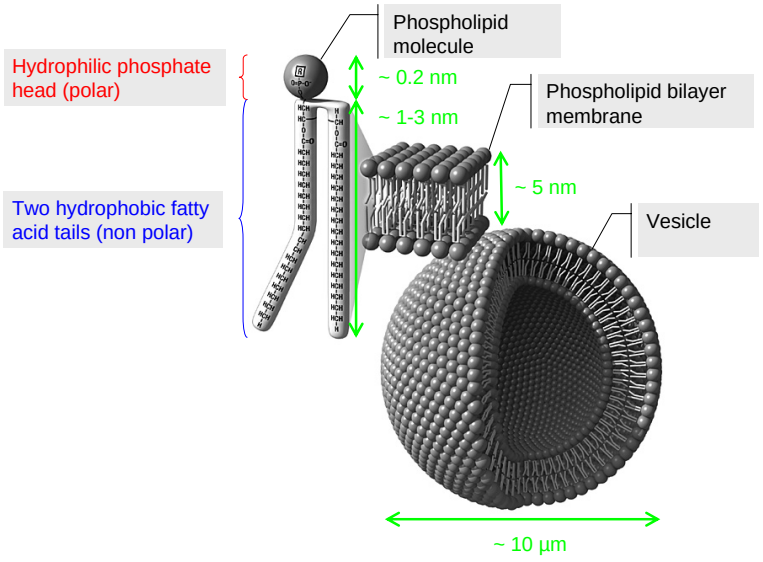

Fig. 2.2: A cartoon showing a vesicle and the molecular structure of its membrane (here is the SOPC molecule). Picture taken from the web site of the Nasa Astrobiology Institute: *http://astrobiology.nasa.gov/nai/*

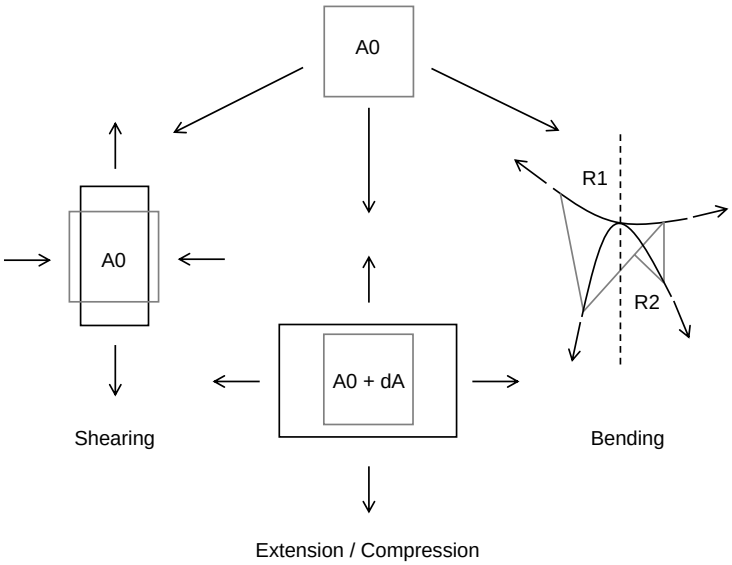

Fig. 2.3: Schematic representation of different deformation modes that a portion of the vesicle membrane surface (the gray colored open square with initial surface A0) can undergo: shearing, extension / compression and bending.

will be discussed in the next chapters.

2.2 Vesicle mechanical properties

A vesicle membrane can undergo three different basic modes of deformation: 1 - *Shearing* (by keeping the membrane surface conserved), 2 - *Extension or compression* (inducing a variation in both the area and the thickness of the membrane) and 3 - *Bending*. Figure. 2.3 illustrates these three different deformation modes.

At room temperature (and at physiological temperature as well) the membrane is at liquid phase. At this phase shearing a portion of the membrane surface does not cost much energy. This is so because the phospholipid molecules are free to move and so to reorganize into a new configuration to relax the applied forces. However the energy required to expand or to compress a portion of it without breaking it off, is very high (surface compressibility modulus $\backsim 100mN/m$ [3]). Therefore, the membrane is considered as a two-dimensional incompressible Newtonian fluid and this implies local and global conservation of the vesicle surface, which will be denoted A. Such conservation of the surface is not observed for other deformable particles, such as

capsules or droplets. This is one of the intrinsic properties of a vesicle which is shared with red blood cells. Moreover, since the water permeability of the membrane is very small (permeability is of the order of $10^{-3} cm/s$ [32]), and that the membrane encloses an incompressible Newtonian fluid (an aqueous solution), the volume V is also a conserved quantity. Both of these properties of vesicles have to be taken into consideration in modelling and simulation. The basic deformation is bending. The amount of energy stored when the membrane ($\partial\Omega$) is bent is given by the so-called Helfrich energy [33]:

$$E = \frac{\kappa}{2} \int_{\partial\Omega} (2H)^2 dA + \int_{\partial\Omega} \zeta dA \tag{2.1}$$

where κ is the membrane rigidity (which is of the order of $10^{-19} J$ [3]) and H the local membrane mean curvature: $H = (1/R_1 + 1/R_2)/2$ where R_1 and R_2 are two radii characterizing locally a curved surface, please refer to Fig. 2.3, in the case of bending mode, for a geometrical interpretation. dA is a surface element on the membrane domain $\partial\Omega$. Note that for the sake of simplicity, we do not account for a spontaneous curvature (a constant spontaneous curvature H_0 may be included by substituting $2H$ by $2(H - H_0)$). The last term $\int_{\partial\Omega} \zeta dA$, where ζ is a Lagrange multiplier, is introduced in order to fulfill the vesicle *local* area dA (perimeter P in 2D) conservation constraint. ζ may be viewed as a two dimensional (on the membrane) pressure-like field that enforces this local area constraint. The enclosed volume V (area A in 2D) conservation constraint is automatically conserved, owing to the divergence-free condition of the velocity field in the fluid (incompressible fluid), and absence of permeation. Indeed, the volume is conserved only if we do not allow for fluid flow across the membrane (exchange or leaking of fluid), as assumed here according to the conventional wisdom.

2.3 Membrane forces

The membrane tries to release excess of bending energy by exerting a reaction force $\mathbf{f}$ upon its surrounding fluid. This force is obtained as a functional derivative of the energy with respect to a membrane elementary displacement:

$$\mathbf{f} = -\frac{\delta E}{\delta \mathbf{r}}, \tag{2.2}$$

where $\delta\mathbf{r}$ is a small displacement of a point belonging to the membrane surface. This is the natural extension of the force definition to an extended entity (in opposition with a material point).

2.3.1 In two-dimension

Numerical studies explored in this thesis have focused on a two dimensional case, for simplicity and for computational time reasons that preclude from having extensive quantitative results on a reasonable time scale in three dimensions. In a two-dimensional space a vesicle is represented by a closed contour. Details of the derivation steps of the membrane force in this case is given in Appendix A and the resulting expression is:

$$\mathbf{f} = \left[\kappa\left(\frac{\partial^2 H}{\partial s^2} + \frac{H^3}{2}\right) - H\zeta\right]\mathbf{n} + \frac{\partial \zeta}{\partial s}\mathbf{t} \ , \tag{2.3}$$

where $\mathbf{t}$ and $\mathbf{n}$ are respectively the tangent and the normal vectors to the membrane contour. s is the curvilinear coordinate along this contour.

This force is composed of a normal as well as a tangential contribution. If ζ is constant along the membrane, then only the normal part survives because of the following reason. If ζ is constant, the tension-like force (which is a vector) associated with ζ is tangential to the curve, and has the same magnitude at both extremities of an arc element ds (which can be taken to be a portion of a circle, provided that ds is small enough). It follows, that the sum of the two forces is directed in the normal direction. If, on the contrary, ζ changes along the contour, then the two values at the extremities of ds are different, and the force has, besides a normal part, a tangential one, which is given by $(\partial\zeta/\partial s)\mathbf{t}$. On the other hand, the bending energy depends on the curvature (which is a geometrical quantity). It follows that the only force that is able to change the shape of a geometrical surface (i.e. a mathematical boundary having no internal physical structure) must be normal to the surface. Finally, note that the term $-\zeta H\mathbf{n}$ has the same structure as the force due to surface tension of a droplet $\mathbf{f} = -\sigma H\mathbf{n}$ where σ is the droplet surface tension. There is, however, a significant physical difference: for a droplet σ is an intrinsic uniform quantity which represents the cost in energy for moving a molecule from the bulk (surrounded by other molecules) to the surface (and thus it looses some neighbors). In the present problem ζ is a Lagrange multiplier which must be determined a posteriori locally at each time by requiring a constant local area. ζ is not an intrinsic quantity, but rather it depends on other parameters (like κ, the vesicle radius, etc...).

2.3.2 In three-dimension

The analytical work presented in this thesis is made in three dimensions, and therefore we need to express the corresponding membrane force. The

three-dimensional version of the membrane force is given by [34]:

$$\mathbf{f} = \left(\kappa \left[2H\left(2H^2 - 2K\right) + 2\Delta_s H\right] - 2\zeta H\right)\mathbf{n} + \nabla_s \zeta, \tag{2.4}$$

where H and K are the mean and the Gaussian curvatures respectively, Δ_s is the Laplace-Beltrami operator and ζ a Lagrange multiplier which is introduced, as it is discussed above, in order to fulfill the local surface conservation of the vesicle membrane, and $\mathbf{n}$ is the normal vector.

$$H = \nabla.\mathbf{n}, \tag{2.5}$$

while the Gaussian curvature K by:

$$2K = H^2 - \nabla\mathbf{n} : \nabla\mathbf{n}^T. \tag{2.6}$$

Note that the above expression for K is nothing but the determinant of the tensor $\nabla\mathbf{n}$, while H is the trace of the same quantity. As these two quantities are invariant under a membrane reparametrisation, it is natural to expect that the energy can depend only on these invariants, as does the Helfrich energy. We have introduced in (2.4) the surface gradient defined as:

$$\nabla_s \equiv (I - \mathbf{n} \otimes \mathbf{n})\nabla. \tag{2.7}$$

The quantity $(I - \mathbf{n} \otimes \mathbf{n})$ is the projector operator. The Laplace-Beltrami operator is defined as:

$$\Delta_s f = \nabla_s.(\nabla_s f) \tag{2.8}$$

where f is any scalar function. A recent concise and self-contained derivation of the force in three dimensions has been given in Ref. [35].

2.4 Vesicle equilibrium shapes

A vesicle does not have a spherical shape as an equilibrium shape in contrast to a droplet. It exhibits other non spherical equilibrium shapes when it is placed in a fluid at rest. Such equilibrium shapes can be computed by minimizing the Helfrich energy Eq. (2.1) while imposing the two constraints of vesicle area S and volume V conservation [36]. Figure 2.4 shows different obtained vesicle equilibrium shapes. An equivalent way for energy minimization is to impose a vanishing force. The only parameter controlling the shape of a vesicle, in the absence of an external applied flow, is the *reduced volume*. This parameter quantifies the degree of deflation of a vesicle, it is given by

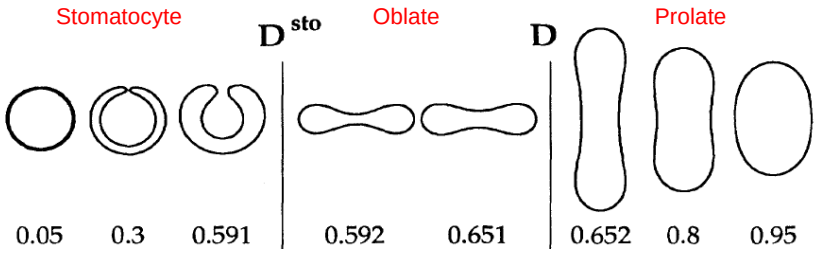

Fig. 2.4: Different vesicle equilibrium shapes as a function of its reduced volume [36].

the ratio of the volume of the vesicle V to the volume of a sphere V_S having the same surface A as the vesicle:

$$\tau = \frac{V}{V_S} = \frac{V}{\frac{4\pi}{3}\left(\frac{A}{4\pi}\right)^{3/2}}, \tag{2.9}$$

it has a value 1 for a spherical vesicle (a maximally swollen vesicle) and less than 1 for a deflated one. In Fig. 2.4 we can see that at the reduced volume of 0.65 the vesicle has a biconcave shape, a similar shape as the one observed for healthy red blood cells.
For a two-dimensional vesicle the reduced volume is defined as the ratio of the area of the vesicle A to the area of a circle having the same perimeter P as the vesicle:

$$\tau_{2D} = \frac{4\pi A}{P^2} \tag{2.10}$$

2.5 Hydrodynamical equations

Since in the next chapters we deal with the dynamical behavior of a vesicle when it is subject to flow, it is worthwhile to mention briefly the corresponding hydrodynamical equations.

2.5.1 Navier-Stokes equations and dimensionless numbers

The flow of the internal and the external fluids, that are considered to be incompressible Newtonian fluids with viscosity η and density ρ (here for simplicity we consider the fluids to be of the same nature), is governed by the known Navier-Stokes equations:

$$\begin{aligned} \rho\left(\frac{\partial \mathbf{v}(\mathbf{r})}{\partial t} + \mathbf{v}(\mathbf{r})\cdot\nabla\mathbf{v}(\mathbf{r})\right) &= -\nabla p(\mathbf{r}) + \eta\nabla^2\mathbf{v}(\mathbf{r}) + \mathbf{f}(\mathbf{r})\delta(\mathbf{r}-\mathbf{r}'), \\ \nabla\cdot\mathbf{v}(\mathbf{r}) &= 0. \end{aligned} \tag{2.11}$$

where $\mathbf{v}$ and p are the velocity and the pressure fields, respectively. $\mathbf{f}$, which appears in the RHS of Eq. (2.11), represents the membrane force applied on the fluid. The flow at a point $\mathbf{r}$ belonging to bulk fluid, or at the membrane, is disturbed by a force (the above membrane force) exerted by a point $\mathbf{r}'$ belonging to the vesicle membrane.
The above Navier-Stokes equations can be rewritten in a dimensionless form (refer to Appendix B for the procedure of dimensionlization):

$$\begin{aligned} \mathrm{Re}\left(\frac{\partial \mathbf{v}^*}{\partial t^*} + \mathbf{v}^*\cdot\nabla^*\mathbf{v}^*\right) &= -\nabla^* p^* + \nabla^{*2}\mathbf{v}^* \\ &+ \frac{1}{Ca}\left(\frac{\partial^2 H^*}{\partial s^{*2}} + \frac{H^{*3}}{2}\right)\delta(\mathbf{r}^*-\mathbf{r}'^*)\mathbf{n} \\ &+ \frac{1}{Ca_s}\left(\frac{\partial \zeta^*}{\partial s^*}\mathbf{t} - H^*\zeta^*\mathbf{n}\right)\delta(\mathbf{r}^*-\mathbf{r}'^*). \end{aligned} \tag{2.12}$$

where dimensionless variables are defined as follows:

- $\mathbf{r}^* = \mathbf{r}/R_0$,
- $t^* = t/T$,
- $\mathbf{v}^* = \mathbf{v}/U$,
- $p^* = pR_0/\eta U$,
- $H^* = H/H_0 = HR_0$,
- $s^* = s/R_0$,
- $\zeta^* = \zeta/\Gamma$ with Γ is the spring-like constant (see discussion below in the summary of dimensionless numbers). In two-dimensional simulations the membrane contour is discretized into points interconnected by elastic spring, see the next chapter for more details.

- $\delta(\mathbf{r}-\mathbf{r}') = \delta(R_0(\mathbf{r}^*-\mathbf{r}'^*)) = \delta(\mathbf{r}^*-\mathbf{r}'^*)/R_0$.

where R_0 is the effective radius of a vesicle taken here as a characteristic length scale, T is a characteristic time scale and U a characteristic velocity of the flow.

Summary about the dimensionless numbers

In summary the adimensional numbers appearing in Eq. (2.12) are:

- The *Reynolds number*:
$$\mathrm{Re} = \frac{\rho U R_0}{\eta}, \tag{2.13}$$
associated to the applied external flow and that measures the importance of the inertial forces upon the viscous ones,

- The *capillary number*:
$$Ca = \frac{\eta\gamma R_0^3}{\kappa} \tag{2.14}$$
associated to the vesicle and measures the ratio between the shear time $1/\gamma$ (γ can be expressed as $\gamma = U/R_0$) and the characteristic time ($\frac{\eta R_0^3}{\kappa}$) needed by a vesicle (at an out-of-equilibrium state) to relax to its equilibrium shape after cessation of flow.

These two numbers are to be supplemented by two other numbers which are:

- The *reduced volume* in 3D (or area in 2D):
$$\tau = \frac{V}{V_S}, \qquad \text{(3D)} \qquad \text{or} \qquad \tau_{2D} = \frac{A}{A_s} \qquad \text{(2D)}, \tag{2.15}$$
V_s (A_s) is the volume (area) of a sphere (circle) having the same area (perimeter) as the vesicle.

- The *viscosity ratio* between the internal and external fluids:
$$\lambda \equiv \frac{\eta_{int}}{\eta_{ext}}. \tag{2.16}$$

We have thus above four independent quantities, and in the small Reynolds number limit (see next section) we shall be left with only three independent dimensionless parameters.

Finally, note that the Lagrange multiplier ζ is not an intrinsic quantity, since it is related to other physical parameters via the constraint of surface free divergence $\nabla_s.\mathbf{v} = 0$. In practice (and especially in numerical treatments) it is useful (see later) to view the membrane incompressibility as achieved thanks to a a quite stiff-spring force between material points on the membrane. In that case it will be needed in the numerics to estimate another dimensionless parameter, namely

- The *tension number*:
$$Ca_s = \frac{\eta\gamma R_0}{\Gamma} \tag{2.17}$$
which is the ratio between the spring relaxation time (recall that Γ is the spring constant) and the shear time.

2.5.2 The Reynolds number and the Stokes flow limit

The flow of an incompressible Newtonian fluid with viscosity η and density ρ is characterized by the dimensionless Reynolds number,

$$\mathrm{Re} = \frac{\rho U R_0}{\eta}, \tag{2.18}$$

where U is a characteristic velocity and R_0 a characteristic length of the studied system. Along the present thesis we take the size of a vesicle, which is of the order of $10 - 100\mu$m [37], as the characteristic length. For such length and for vesicles suspended in an aqueous solution subject to shear, with moderate applied shear rates ($\gamma = U/R_0$) that are usually of the order of $10s^{-1}$, the Reynolds number is rather small, $\mathrm{Re} \sim 10^{-3} - 10^{-2} \ll 1$. At such small Reynolds number limit (Stokes flow), the fluid flow is well approximated by the Stokes equations:

$$\begin{aligned} -\nabla p(\mathbf{r}) + \eta\nabla^2\mathbf{v}(\mathbf{r}) &= -\mathbf{f}(\mathbf{r})\delta(\mathbf{r}-\mathbf{r}'), \\ \nabla\cdot\mathbf{v}(\mathbf{r}) &= 0. \end{aligned} \tag{2.19}$$

In this limit, which is the typical situation in microfluidic devices, for example, the viscous forces are dominant over the inertial ones, the flow is almost laminar, and no turbulence can be observed, at least in the absence of vesicle. Moreover the fluid flow does not depend on its previous history (because of the absence of the term $\partial\mathbf{v}/\partial t$ in the Stokes equation), it depends only on the boundary conditions and it is generated and maintained by external applied forces. When the driven forces are switched off the fluid stop flowing [38]. The Stokes equations enjoy an important symmetry: they are symmetric upon time reversal. This has several consequences, like no lift

can be experienced close to a substrate for a spherical suspended entity, the flow is symmetric past a symmetric obstacle, the absence of swimming for swimmers having only one degree of freedom (the Scallop theorem) and so on [38, 39].

2.6 Boundary conditions on the membrane

The dynamics require specifying boundary conditions on the vesicle membrane $\partial\Omega$:

- Because of the (largely adopted) assumption of non-slip at the membrane, together with non permeability of the membrane, the velocity at the vesicle membrane is continuous [40]:

$$\mathbf{v}^{\text{ext}}(\mathbf{r}_{\text{m}}) = \mathbf{v}^{\text{int}}(\mathbf{r}_{\text{m}}) = \mathbf{v}(\mathbf{r}_{\text{m}}) \qquad \text{where} \qquad \mathbf{r}_{\text{m}} \in \partial\Omega. \tag{2.20}$$

  where $\mathbf{v}^{\text{ext}}$ and $\mathbf{v}^{\text{int}}$ are the velocity of the external and the internal fluids, respectively.

- The hydrodynamical stresses due to the external and the internal fluids flow are balanced by the membrane force $\mathbf{f}$:

$$\left(\sigma^{\text{ext}}(\mathbf{r}_{\text{m}}) - \sigma^{\text{int}}(\mathbf{r}_{\text{m}})\right)\mathbf{n} = -\mathbf{f}(\mathbf{r}_{\text{m}}) \qquad \text{where} \qquad \mathbf{r}_{\text{m}} \in \partial\Omega. \tag{2.21}$$

  where $\sigma_{ij} = -p\delta_{ij} + \eta(\partial_i u_j + \partial_j u_i)$ is the stress tensor.

- At large distances from the location of the vesicle membrane the external fluid (Ω_{ext}) flow tends to its undisturbed state:

$$\mathbf{v}^{\text{ext}}(\mathbf{r}) \underset{|\mathbf{r}-\mathbf{r}_{\text{m}}|\to\infty}{\longrightarrow} \mathbf{v}^{\infty}(\mathbf{r}) \qquad \text{where} \quad \mathbf{r}_{\text{m}} \in \partial\Omega \quad \text{and} \quad \mathbf{r} \in \Omega_{ext}. \tag{2.22}$$

  where $\mathbf{v}^{\infty}$ is the undisturbed external applied flow.

3. THE USED METHODS FOR SOLVING VESICLE DYNAMICS

In the present chapter methods used to solve the hydrodynamical equations (Eqs. 2.11 in Ch. 2), to capture dynamics and deformation of vesicles, are presented. Each method presents advantages and drawbacks for given situation. Advantages and drawbacks of each method are discussed.

3.1 The boundary integral method

The boundary integral method (BIM) - also named the boundary elements method (BEM) - is an adequate numerical method to simulate dynamics of free deformable interfaces moving under Stokes flows in unbounded or semi-bounded geometries. Physical quantities of interest are directly computed on the interface; therefore, there is no need to solve for the fluid flow throughout the whole computational domain in order to capture the dynamics of the membrane. The Stokes equations, which are linear partial differential equations, can be converted into an integral equation form (see Appendix C). For more details about the method see [41] and [42]. The method has been adapted to the problem of vesicle dynamics by several groups [19, 20, 43].

Integral equation

The unknown solutions of the Stokes equations are written in the form of integral equations (see Appendix C). Here we give the expression of the velocity which is valid everywhere in the fluid domains, and in particular at the membrane. Knowledge of membrane velocity is sufficient in order to ascertain the subsequent vesicle evolution. The velocity at any point of the fluid domains takes the form

$$\begin{aligned}\Delta v_j(\mathbf{r}) &= \frac{1}{4\pi}\oint_{\partial\Omega} G^S_{ji}(\mathbf{r},\mathbf{r}')f_i(\mathbf{r}')ds(\mathbf{r}') \\ &\quad + \frac{(\eta_{\text{ext}}-\eta_{\text{int}})}{4\pi}\oint_{\partial\Omega} v_i(\mathbf{r}')T^S_{ijk}(\mathbf{r}',\mathbf{r})n_k(\mathbf{r}')ds(\mathbf{r}') \\ &\quad + \eta_{\text{ext}}v^\infty_j(\mathbf{r}) \end{aligned} \tag{3.1}$$

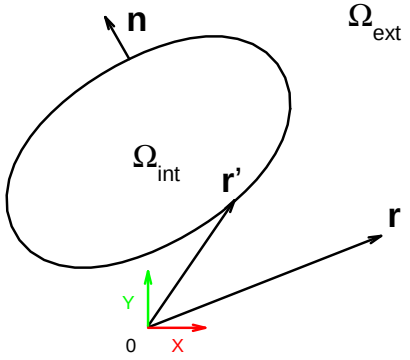

Fig. 3.1: A schematic representation of a vesicle membrane contour $\partial\Omega$ (in 2D), the internal fluid Ω_{int} and the external fluid Ω_{ext} domains. $\mathbf{r}$ is a location where the velocity is evaluated and $\mathbf{r}'$ a point belonging to the vesicle membrane.

with

$$\Delta = \begin{cases} \eta_{\text{int}} & \mathbf{r} \in \Omega_{\text{int}} \\ \eta_{\text{ext}} & \mathbf{r} \in \Omega_{\text{ext}} \\ \frac{1}{2}(\eta_{\text{int}} + \eta_{\text{ext}}) & \mathbf{r} \in \partial\Omega \end{cases} \tag{3.2}$$

where $\mathbf{v}^{\infty}$ is the applied undisturbed flow velocity, the first integral with the kernel $\mathbf{G}^S$ is known as the *single-layer potential* and the second one with the kernel $\mathbf{T}^S$ is known as the *double-layer potential*. The unknown solution $\mathbf{v}$ appears on the LHS of Eq. 3.1 and as well as on its RHS under the integral sign. Because the domain of integration is well defined, the integral equation is a *Fredholm integral equation of the second kind*.
In the absence of viscosity contrast ($\eta_{\text{int}} = \eta_{\text{ext}} = \eta$), Eq. 3.1 reduces to the simpler expression:

$$v_j(\mathbf{r}) = \frac{1}{4\pi\eta} \oint_{\partial\Omega} G_{ji}(\mathbf{r}, \mathbf{r}') f_i(\mathbf{r}') ds(\mathbf{r}') + v_j^{\infty}(\mathbf{r}) \tag{3.3}$$

This equation is valid for any point $\mathbf{r}$ in the whole computational domain: at the membrane $\partial\Omega$ as well as in both fluids Ω_{int} and Ω_{ext}.

Green's functions

The integral kernels, $\mathbf{G}$ and $\mathbf{T}$, appearing in both integral equations 3.1 and 3.3 are Green's functions.
For a two-dimensional infinite fluid (unbounded geometry), they have the

following expressions:

$$G_{ij}^S = -\delta_{ij}\ln r + \frac{r_i r_j}{r^2} \qquad T_{ijk}^S = -4\frac{r_i r_j r_k}{r^4} \tag{3.4}$$

Stokeslet Stresslet

where $r \equiv |\mathbf{r}-\mathbf{r}'|$ and r_i is the i^{th} component of the vector $\mathbf{r}-\mathbf{r}'$. Physically the Stokeslet represents the induced fluid velocity in the i-direction at the position $\mathbf{r}$ due to a unit singular force exerted locally at $\mathbf{r}'$ and has the j-direction.
The Green's functions have the following properties:

$$G_{ij}(\mathbf{r},\mathbf{r}') = G_{ji}(\mathbf{r},\mathbf{r}'), \tag{3.5}$$
$$G_{ij}(\mathbf{r},\mathbf{r}') = G_{ij}(\mathbf{r}',\mathbf{r}), \tag{3.6}$$
$$T_{ijk}(\mathbf{r},\mathbf{r}') = -T_{ijk}(\mathbf{r}',\mathbf{r}). \tag{3.7}$$

In the case of a two-dimensional fluid bounded by an infinite solid plane wall (half-space) located at $y = w$, the Green's functions are given by:
The velocity Green's function can be presented as a sum of the following elementary Green's functions

$$\begin{aligned}\mathbf{G}_{ij}^W(\mathbf{r},\mathbf{r}') &= \mathbf{G}_{ij}^S(\hat{\mathbf{r}}) - \mathbf{G}_{ij}^S(\hat{\mathbf{R}}) \\ &\quad +2h_0^2\mathbf{G}_{ij}^D(\hat{\mathbf{R}}) - 2h_0\mathbf{G}_{ij}^{SD}(\hat{\mathbf{R}})\end{aligned} \tag{3.8}$$

where $\hat{\mathbf{r}} = \mathbf{r}-\mathbf{r}'$ and $\hat{\mathbf{R}} = \mathbf{r}-\mathbf{r}'_{IM}$ with $\mathbf{r}'_{IM} = (r'_x, 2w - r'_y)$ is the image of $\mathbf{r}'$ with respect to wall. $h_0 = r'_y - w$ is the distance of the point force from the wall. The other terms are:

- Stokeslet doublet
$$\mathbf{G}_{ij}^D(\mathbf{r}) = \pm\left(\frac{\delta_{ij}}{r^2} - 2\frac{r_i r_j}{r^4}\right) \tag{3.9}$$

- Source doublet
$$\mathbf{G}_{ij}^{SD}(\mathbf{r}) = r_y\mathbf{G}_{ij}^D(\mathbf{r}) \pm \frac{\delta_{jy}r_i - \delta_{iy}r_j}{r^2} \tag{3.10}$$

  with " + " for x-direction and " − " for y-direction

The stress Green's function

$$\mathbf{T}^W(\mathbf{r},\mathbf{r}') = \mathbf{T}^S(\hat{\mathbf{r}}) - \mathbf{T}^S(\hat{\mathbf{R}}) + 2h_0^2\mathbf{T}^D(\hat{\mathbf{R}}) - 2h_0\mathbf{T}^{SD}(\hat{\mathbf{R}}) \tag{3.11}$$

where

$$\begin{aligned} T^D_{ijk} &= \frac{\partial G^D_{ij}}{\partial r_k} + \frac{\partial G^D_{kj}}{\partial r_i}, \\ &= \pm 4\left(-\frac{\delta_{ij}r_k + \delta_{ik}r_j + \delta_{jk}r_i}{|\mathbf{r}|^4} + 4\frac{r_i r_j r_k}{|\mathbf{r}|^6}\right) \end{aligned} \tag{3.12}$$

$$\tag{3.13}$$

and

$$\begin{aligned} T^{SD}_{ijk} &= \frac{G^{SD}_{ij}}{\partial r_k} + \frac{\partial G^{SD}_{kj}}{\partial r_i} - \delta_{ik}p^{SD}_j \\ &= r_y T^D_{ijk} \pm 2\left(\frac{\delta_{jy}\delta_{ki}}{|\mathbf{r}|^2} - \frac{\delta_{jy}r_k r_i}{|\mathbf{r}|^4}\right) - \delta_{ik}p^{SD}_j \end{aligned} \tag{3.14}$$

with the vector $\mathbf{p}^{SD}$ having the components:

$$\mathbf{p}^{SD} = -\frac{2}{|\mathbf{r}|^4}\left(2r_x r_y, r_x^2 - r_y^2\right). \tag{3.15}$$

Thus, depending on the geometry of the studied problem (unbounded or bounded by a wall) we substitute $\mathbf{G}^S$ (respectively $\mathbf{T}^S$) into Eq. 3.1 with the appropriate function. More precisely, for the study of dynamics of a vesicle suspended in an unbounded flow (situation corresponding to infinite fluid) we use the couple $\left(G^S_{ij}, T^S_{ij}\right)$ given by Eqs. 3.4. This is used in chapter 5 in order to study the lateral migration of a vesicle in unbounded Poiseuille flow. For a vesicle placed in a semi-bounded flow (a fluid bounded by infinite plane wall), we use the couple $\left(G^W_{ij}, T^W_{ij}\right)$ that take into consideration the existence of the wall (via the notion of images, like in electrostatics). This is used in order to simulate the lateral migration of a vesicle under the influence of both the wall and the Poiseuille flow, see chapter 5.

Numerical procedure steps

In general, nonlinear integral equations (as those encountered here) have no available exact analytical solution. The shape of the vesicle obeys such nonlinear integral equation. The shape of a vesicle is not known a priori (not a fixed shape) and has not a simple geometry, in general, except in the very special situation of a sphere. Thus, in general, one has to resort to numerical techniques. For that purpose the vesicle membrane contour (in 2D) is discretized and the integral equation takes a dicretized form, which can, in principle, be handled numerically . After evaluating the membrane force

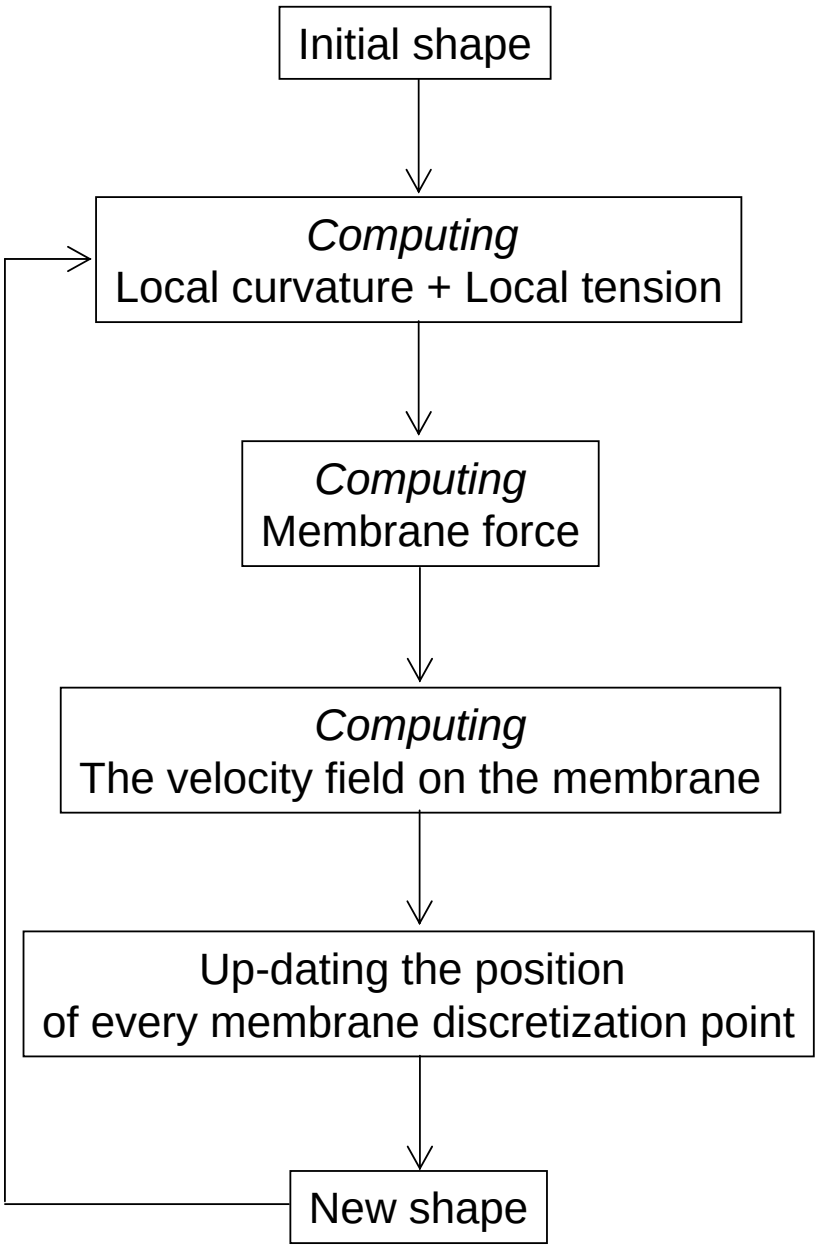

Fig. 3.2: Organigram giving the main steps performed to get the vesicle dynamics.

which enters the right hand side of Eq. (3.3), the velocity is then evaluated at each discretization point using Eq. (3.3). The displacement in the course of time of the vesicle membrane is obtained by updating the discretization points after each time iteration, using a Euler scheme (See the organigram in Fig. 3.2):

$$\mathbf{r}(t+dt) = \mathbf{v}(\mathbf{r},t)dt + \mathbf{r}(t). \tag{3.16}$$

Fulfilling local membrane area

In principle, from Eq.(3.3) we can determine the membrane velocity, if the force and the initial shape are given. The force (2.3) contains geometrical quantities (like the normal vector and mean curvature H) which are determined from the initial shape, plus a function $\zeta(s,t)$, which is unknown a priori. Numerically, the following method has been tested. An initial shape (typically an ellipse) and an initial ζ (typically a constant along the contour) have to be chosen. Then the geometrical quantities appearing in the force can be calculated (the method of discretization of the integral equation (3.3) has been discussed in [40]). This allows one to evaluate the right hand side of (3.3) at initial time. The membrane velocity at this time is thus fixed. We then displace each membrane element according to the computed velocity, and by this way we obtain a new shape. However, the new shape does not fulfill, in general, the local membrane incompressibility. A local stretching (or compression) of the membrane takes place as long as the projected divergence of the velocity field of the fluid adjacent to the membrane is non zero. We thus must adjust the appropriate function $\zeta(s)$ in order to fulfill this condition. The condition that the projected divergence must vanish reads

$$(\mathbf{I} - \mathbf{nn}) : \nabla\mathbf{v} = 0 \tag{3.17}$$

where $\mathbf{I}$ is the identity tensor, and $\mathbf{nn}$ stands for the tensor product ($\mathbf{I} - \mathbf{nn}$ is the projector on the contour). The above relation can be viewed as an implicit equation for $\zeta(s)$, similar to $\nabla.\mathbf{v} = 0$ which fixes the pressure field in 3D fluids. This way of reasoning is quite practical in the analytical study of vesicles [17]. From the numerical point of view, this way has suffered from several numerical instabilities. We have thus introduced another approach [40] as outlined below.

In a 2D simulation, when discretizing the vesicle membrane contour, the vesicle perimeter conservation constraint could be achieved without dealing with the local Lagrange multiplier entering the membrane force given by Eq. (2.3). This constraint could be fulfilled in another and more convenient way. For that purpose we have used a straightforward method based on the fact that two material representative points on the membrane are attached to

each other by strong cohesive forces which we describe by quasi-rigid springs, so that we can achieve in numerical studies less than 1% variation of the area. By this way an additional parameter k_s is introduced, which is the spring constant [40], $\zeta^N(i) = \Gamma(ds(i) - ds^0(i))$. By choosing Γ large enough (in order to keep the membrane quasi-incompressible) the discretization step $ds(i)$ is kept as close as possible to its initial value $ds^0(i)$. Typically in units where $\eta = \kappa = 1$ and where the typical radius of vesicles is of order unity, a value of $\Gamma = 10^3$ has proven to be sufficient.

Advantages of the boundary integral formulation

- Reducing the problem dimensionality from 2D to 1D,
- Computing directly the vesicle membrane velocity (i.e. we do not need to solve the problem in the fluid bulk),
- Tracking high deformations of the vesicle membrane,
- Incorporating easily the vesicle membrane force.

Drawbacks

- Evaluating integral equations with integrands exhibiting singularities (logarithmic for $\mathbf{G}$ and $1/r$ for $\mathbf{T}$),
- Limited geometrical configurations for which the Green's functions exist (an unbounded and semi-bounded media). Note, however, that the Green's function for an unbounded domain can be used in the presence of any typpe of bounding walls. This is done at certain price; one has to integrate over bounding boundaries terms of the form $\int_{\text{Boundary}} \mathbf{G}\sigma$ and $\int_{\text{Boundary}} \mathbf{T}\mathbf{v}$ where σ is the total stress at the boundary and $\mathbf{v}$ the velocity on that boundary.
- Spurious buckling of the membrane is observed for long time simulations (in particular in 3D).

3.2 The lattice-Boltzmann method

3.2.1 Fluid flow

In the limit of small Mach M (ratio of the speed of a particle in a medium to the speed of sound in that medium) and Knudsen K (ratio of the molecular mean free path to the macroscopic characteristic length scale) numbers

(smaller than 0.15 the hydrodynamic limit of the kinetic theory) the lattice-Boltzmann methods recover with good approximation, using Chapman-Enskog procedure [44], the solutions of the known Navier-Stokes equations:

$$\rho\left(\frac{\partial \mathbf{u}}{\partial t}+\mathbf{u}\cdot\nabla\mathbf{u}\right) = -\nabla p+\eta\nabla^2\mathbf{u}+\mathbf{f}, \tag{3.18}$$

$$\nabla\cdot\mathbf{u} = 0. \tag{3.19}$$

governing the fluid flow of an imcompressible Newtonian fluid. Where ρ and η are respectively the mass density and the dynamic viscosity of the studied fluid, $\mathbf{u}$ and p are respectively its velocity and pressure fields (which are the unknown quanities). $\mathbf{f}$ in the right-hand side of Eq. (3.18) is a bulk force (e.g. gravity) or the membrane forces as it is used here and discussed below. In the recent decades, the lattice-Boltzmann method has been introduced and widely used to simulate at the mesoscopic scale fluid flow in more complex situations, such as fluid flow with complex bounding geometries (e.g. in porous media), flow of multi-components and multi-phases fluid (e.g drops and binary fluids), for a general review see Refs. [45–47]). Popularity of the LB method among scientists and engineers has been gained because of its straightforward implementation and its locality that allows for parallel programming.

Lattice-Boltzmann method approach

In the spirit of the lattice-Boltzmann method, a fluid is seen as a cluster of pseudo-fluid particles (or packets of this fluid), that can collide with each other when they spread under the influence of external applied forces. The main quantity associated to a pseudo-fluid particle is the distribution function:

$$f_{\mathrm{i}}(\mathbf{r},t), \tag{3.20}$$

that gives the probability to find the pseudo-fluid particle at the position $\mathbf{r}$ and with the velocity $\mathbf{c}_{\mathrm{i}}$, in the i-direction, at the time t. In the lattice-Blotzmann method context, not only the position space is discretized but also the velocity space too. This implies that every pseudo-fluid particle can move just to given discrete directions with given discrete velocities.
There are many LB lattices in which the position and the velocity spaces are discretized (in different ways). It is then demanded that the method should fulfill the following constraints:

- Mass conservation,
- Momentum conservation,

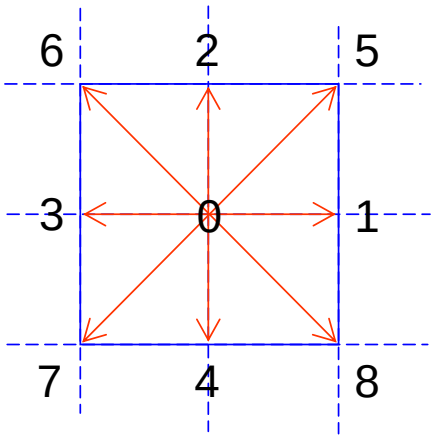

Fig. 3.3: The lattice Boltzmann D2Q9.

- Galilean and rotational invariance

Here, the D2Q9 lattice is used, D2 means two-dimensional space and Q9 the number of possible discrete velocity vectors (that means a pseudo-particle can move just to 9 given possible directions), see Fig. 3.3. The choice of 9 directions is due to the constraints that the continuum limit of the LBM provides the Navier-Stokes equations. If, for example, only the first neighbors are included in Fig. 3.3, then we would not have the isotropic Laplacian in the Navier-Stokes equations.
The evolution in time of the distribution f_i is governed by the so-called lattice Boltzmann equation:

$$f_\mathrm{i}^{\mathrm{new}}(\mathbf{r}+\mathbf{c}_\mathrm{i}\Delta t, t+\Delta t) - f_\mathrm{i}^{\mathrm{old}}(\mathbf{r},t) = \Delta t\,(\Omega_\mathrm{i}+F_\mathrm{i}) \qquad (i=0...8), \tag{3.21}$$

where $f_\mathrm{i}^{\mathrm{old}}(\mathbf{r},t)$ is the old distribution of the pseudo-fluid particle when it was at the position $\mathbf{r}$ at the previous time t, $f_\mathrm{i}^{\mathrm{new}}(\mathbf{r}+\mathbf{c}_\mathrm{i}\Delta t, t+\Delta t)$ is the new distribution of the same pseudo-fluid particle after it moved in the direction $\mathbf{c}_\mathrm{i}$ to the new location $\mathbf{r}+\mathbf{c}_\mathrm{i}\Delta t$ during the ellapsed time Δt, with Δt is the time step. The left-hand side of Eq. (3.21) alone gives the spreading of the pseudo-fluid particles freely under no external applied forces. In the right-hand side of Eq. (3.21), F_i is an external applied force and Ω_i is the collision operator. Here the Bhatnagar-Gross-Krouk (BGK) approximation is used for the operator (which is valid for $Re << 1$ Stokes limit) [48]:

$$\Omega_\mathrm{i} = -\frac{1}{\tau}\left(f_\mathrm{i}^{\mathrm{old}}(\mathbf{r},t) - f_\mathrm{i}^{\mathrm{eq}}(\mathbf{r},t)\right), \tag{3.22}$$

that describes the relaxation of the pseudo-fluid particle distribution $f_\mathrm{i}^{\mathrm{old}}(\mathbf{r},t)$ to an equilibrium distribution $f_\mathrm{i}^{\mathrm{eq}}(\mathbf{r},t)$ (to be defined below) with a relaxation

time τ. This relaxation time is related to an intrinsic macroscopic quantity characterizing the fluid which is the kinematic viscosity ν via the relation:

$$\nu = c_{\mathrm{S}}^2 \Delta t \left(\tau - \frac{1}{2} \right), \tag{3.23}$$

where c_{S} is the speed of the sound. For the LB lattice model used here (D2Q9) $c_{\mathrm{S}} = 1/\sqrt{3}$ (in lattice units). The viscosity is then given by:

$$\nu = \frac{2\tau - 1}{6}, \tag{3.24}$$

in our simulations we used the value $\tau = 1$ for the method to be stable and for the particle density and viscosity to be positive. The equilibrium distribution $f_{\mathrm{i}}^{\mathrm{eq}}(\mathbf{r}, t)$ - which is given as an approximation of the Maxwell-Boltzmann equilibrium distribution - is given by:

$$f_{\mathrm{i}}^{\mathrm{eq}}(\mathbf{r}, t) = \omega_{\mathrm{i}} \rho(\mathbf{r}, t) \left[c_1 + c_2 \left(\mathbf{c}_i \cdot \mathbf{u} \right) + c_3 \left(\mathbf{c}_{\mathrm{i}} \cdot \mathbf{u} \right)^2 + c_4 \left(\mathbf{u} \cdot \mathbf{u} \right) \right] \tag{3.25}$$

where c_1, c_2, c_3 and c_4 are lattice constants and ω_{i} are the weight factors, see Fig. 3.3. For the D2Q9 lattice, $c_1 = 1$, $c_2 = 1/c_{\mathrm{S}}^2$, $c_3 = 1/(2c_{\mathrm{S}}^4)$, $c_4 = -1/c_{\mathrm{S}}^2$ and ω_{i} equals 4/9 for 0 velocity vector, 1/9 in the directions of nearest neighbors, and 1/36 in the diagonal directions.
$\rho(\mathbf{r}, t)$ is the local density defined in term of f_i as:

$$\rho(\mathbf{r}, t) = \sum_{\mathrm{i}=0}^{8} f_{\mathrm{i}}(\mathbf{r}, t) \tag{3.26}$$

and,

$$\mathbf{u}(\mathbf{r}, t) = \frac{1}{\rho(\mathbf{r}, t)} \sum_{\mathrm{i}=0}^{8} f_{\mathrm{i}}(\mathbf{r}, t) \mathbf{c}_{\mathrm{i}} \tag{3.27}$$

is the fluid local velocity. In our simulations we always check and try to keep $\mathbf{u}$ smaller than a value of 0.1 (by choosing appropriate simulation parameters) in order to stay in the limit of small Mach numbers (usual liquid regime, besides sound propagation). The LBM are weakly-compressible methods. In the BGK approximation we used, the method is valid for small values of M and smaller values of the Reynolds number.
The fluid local pressure is given by:

$$p(\mathbf{r}, t) = \rho(\mathbf{r}, t) c_{\mathrm{S}}^2. \tag{3.28}$$

The boundary conditions

On the bounding walls The fluid is represented by a fixed mesh. The simulation box is a rectangular box with width L and height $2W$. Periodic boundary conditions are imposed on the right and on the left side of the box, i.e. the inlet and the outlet of the fluid flow. Care has to be taken when choosing the value of L. The physics of the problem can be dramatically affected when values of L are chosen without caution. This value has to be chosen large enough in a such way that the disturbance of the presence of the vesicle on the external applied flow can not be felt at the boundaries of the simulation box. If a smaller value of L is chosen, the simulations will produce results corresponding to a periodic suspension array of vesicles separated by a distance L, therefore the inclination angle and other measured physical quantities will be affected by the nearest neighboring vesicles.
Bounceback boundary conditions are implemented on the two walls [49]:

$$f_{-i}(\mathbf{r}, t + \Delta t) = f_i(\mathbf{r}, t) + 2\frac{\rho w_i}{c_s^2}(\mathbf{u}_{wall} \cdot c_1), \tag{3.29}$$

where $\mathbf{u}_{wall}$ is the velocity of the displacement of the wall. The shear flow is generated by moving the two walls with the same velocity but in the opposite directions. At the steady regime we obtain (for a fluid which is free of vesicles) a linear shear velocity profile of the form $\mathbf{u}^{\infty} = \gamma y \mathbf{c}_1$ where $\gamma = u_{wall}/W$ is the shear rate.

On the vesicle membrane Because of the non-slip boundary condition and the non permeability of the membrane the velocity across the vesicle membrane is continuous:

$$\mathbf{v}^{\text{ext}}(\mathbf{r}_{\text{m}}) = \mathbf{v}^{\text{int}}(\mathbf{r}_{\text{m}}) = \mathbf{v}(\mathbf{r}_{\text{m}}) \qquad \text{where} \qquad \mathbf{r}_{\text{m}} \in \partial\Omega. \tag{3.30}$$

The hydrodynamical stresses due to the external and the internal fluids flow are balanced by the membrane force $\mathbf{f}$:

$$\left(\sigma^{\text{ext}} - \sigma^{\text{int}}\right)\mathbf{n} = -\mathbf{f} \qquad \text{where} \qquad \mathbf{r}_{\text{m}} \in \partial\Omega. \tag{3.31}$$

At large distances from the location of the vesicle membrane the external fluid flow tends to its undisturbed shape:

$$\mathbf{v}^{\text{ext}}(\mathbf{r}) \underset{|\mathbf{r}-\mathbf{r}_{\text{m}}|\to\infty}{\longrightarrow} \mathbf{v}^{\infty}(\mathbf{r}) \qquad \text{where} \qquad \mathbf{r}_{\text{m}} \in \partial\Omega \quad \text{and} \quad \mathbf{r} \in \Omega_{ext}. \tag{3.32}$$

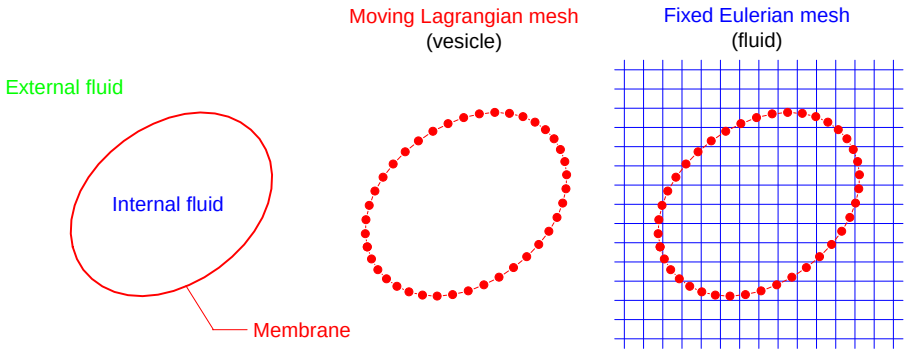

Fig. 3.4: Schematic showing a Lagrangian mesh representing a two-dimensional vesicle (where the membrane is represented by a contour) immersed in a Eulerian mesh representing a fluid.

Fluid flow parameters

In the framework of the lattice-Boltzmann simulations we take the viscosity $\eta = 1/6$, the mass density $\rho = 1$ and fluid flow velocity always smaller than 0.1. The choice of the parameters are also dictated by the fact that the low Reynolds and low Mach numbers limits are respected.

3.2.2 Fluid-vesicle interaction

The immersed boundary approach

It remains to be shown now how the membrane is coupled with the flow. For that purpose we make us of the so-called *immersed boundary method*. The immersed boundary method (IBM) was developed first by C. S. Peskin to simulate some aspect of blood flow in heart [50]; for a review see Ref. [51]. Within the framework of this method an interface (separating two regions occupied by two fluids) is discretized into points interconnected by elastic springs (as it is illustrated in Fig. 3.4 for the vesicle case). This interface is represented by a moving Lagrangian mesh immersed in a fixed Eulerian mesh representing the fluid. The fluid flow is computed, using a Navier-Stokes equations solver, in the whole computational domain by ignoring the existence of the interface. The fluid feels the existence of the interface due

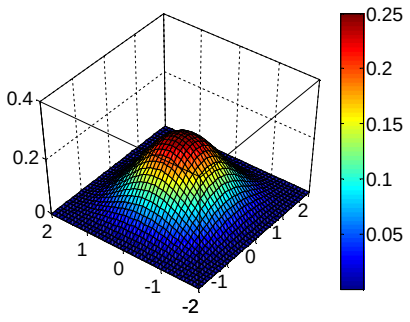

Fig. 3.5: The discrete delta function

to point singular forces exerted by the membrane nodes on their respective surrounding fluid nodes. Physical quantities computed on every mesh are linked to each others via a discrete delta function suggested by C. S. Peskin [52].

$$\Delta(\mathbf{x}) = \begin{cases} \frac{1}{16l_s^2}\left(1+\cos\frac{\pi x}{2l_s}\right)\left(1+\cos\frac{\pi y}{2l_s}\right) & \text{for} \quad |x| \leqslant 2l_s \quad \text{and} \quad |y| \leqslant 2l_s, \\ 0 & \text{otherwise,} \end{cases} \tag{3.33}$$

where l_s is the lattice spacing. Here, in the context of the lattice-Boltzmann method, it has a fixed value $l_s = 1$. The function Δ has non zero values on a square of an area $4l_s \times 4l_s$ (see Fig. 3.5). In the present work the same strategy as in IBM is used to simulate vesicle dynamics under a flow computed here by the lattice-Boltzmann method.

Fluid flow action on the vesicle

The velocity at a given membrane node $\mathbf{r}_m$ is evaluated by interpolating the velocities at its nearest fluid nodes $\mathbf{r}_f$, which are already computed by the lattice Boltzmann procedure, using the Δ function:

$$\mathbf{v}(\mathbf{r}_m) = \sum_f \Delta(\mathbf{r}_f - \mathbf{r}_m)\mathbf{u}(\mathbf{r}_f) \qquad \mathbf{r}_m \in \partial\Omega. \tag{3.34}$$

Such a procedure of deducing the velocity of membrane nodes from fluid nodes velocity is possible since we considered that velocity is continuous across the membrane. After evaluating every membrane node velocity we update its position using a Euler scheme:

$$\mathbf{r}_m(t+dt) = \mathbf{r}_m(t) + \mathbf{v}(\mathbf{r}_m(t)). \tag{3.35}$$

and so the shape deformation and dynamics of the vesicle is computed. The same procedure steps as for the boundary integral method simulation is used here, except that the velocity involved in Eq. (3.35) is computed using the lattice Bolzmann procedure.

Vesicle action on the fluid flow

The vesicle membrane is not a passive interface but an active one that induces disturbance on the applied flow. It exerts a reaction force as a response to the applied hydrodynamical stresses that try to bend it. This force is given by the following formula:

$$\mathbf{f}(\mathbf{r}_m) = \left[\kappa_B \left(\frac{\partial^2 H}{\partial s^2} + \frac{H^3}{2}\right) - H\zeta\right]\mathbf{n} + \frac{\partial \zeta}{\partial s}\mathbf{t} + \kappa_A \left(A - A_0\right)\mathbf{n}, \qquad (3.36)$$

where H is the local curvature of the membrane, κ is its rigidity, $\mathbf{n}$ and $\mathbf{t}$ are respectively the normal and the tangential unit vectors. The additional last term in Eq. (3.36) is added to force area conservation, since numerically a slight variation of area is observed as it is discussed in Ref. [40]. A detailed derivation of this force can be found in Appendix A. This force has a non zero value only at the membrane. Therefore, a given fluid point localized at $\mathbf{r}_f$ is subject to the force:

$$\mathbf{F}(\mathbf{r_f}) = \int_{\partial\Omega} \mathbf{f}(\mathbf{r_m})\delta(\mathbf{r_f} - \mathbf{r_m})ds(\mathbf{r_m}) \qquad \text{with} \qquad \mathbf{r_m} \in \partial\mathbf{\Omega} \qquad (3.37)$$

However, since the membrane is discretized and thus presented by a cluster of points, this integral is rather a sum of the singular forces localized on the membrane nodes:

$$\mathbf{F}(\mathbf{r_f}) = \sum_m \mathbf{f}(\mathbf{r_m})\delta(\mathbf{r_f} - \mathbf{r_m})ds(\mathbf{r_m}) \qquad (3.38)$$

In addition, writing the force felt by a fluid node in term of an ordinary Dirac's delta function is not suitable here, since the membrane nodes are off-lattice and do not necessarily coincide with the fluid lattice nodes. The Dirac's delta function in Eq. (3.38) has to be replaced by a function that takes into account the discrete nature of the fluid medium in order to distribute membrane force on the nearby fluids nodes. We use the Δ function suggested above which has a peak on the membrane node and it decays to zero at a distance equal to twice the lattice spacing (Fig. 3.5). The choice of a such shape of the function Δ has to smooth out the presence of the Eulerian lattice as much as possible. It is required to avoid jumps in velocity or in

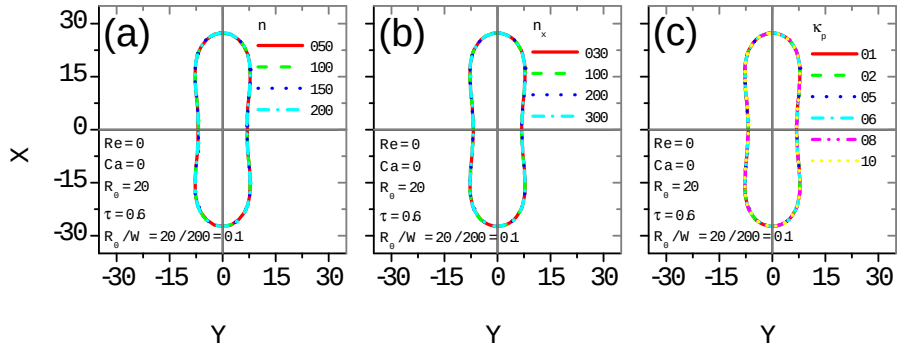

Fig. 3.6: LBM computed equilibrium shapes of a vesicle for different values of the numerical parameters : (a) the discretization points on the vesicle membrane n, (b) the half width of the simulation box n_x and (c) the spring constant κ_p. Here the vesicle has an effective radius of $R_0 = 20$, a reduced volume of $\tau = 0.60$ and is placed in a fluid at rest ($Re = Ca = 0$) bounded by two walls at a distance of $2W = 401$.

applied force as the Lagrangian membrane points cross over the Eulerian grid axes [52]. In this way the membrane force has no zero value only in a squared area of size $4l_s \times 4l_s$ centered on the membrane node.

3.2.3 Convergence and benchmarking tests

As a convergence test computed equilibrium shapes of a vesicle, with reduced volume of $\tau = 0.6$, for different values of the numerical parameters are performed and are shown in Fig. 3.6. In each case we vary one of the three numerical parameters: the discretization points on the vesicle membrane n, the half width of the simulation box n_x and the spring constant κ_p. In all cases the physical parameters are kept the same: $Re = Ca = 0$, $R_0 = 20$ and $R_0/W = 0.1$. All the obtained curves, corresponding to the equilibrium shapes, collapse onto one curve as it is illustrated in Figs. 3.6a, 3.6b and 3.6c. For the range of the numerical parameters used for Figs. 3.6 the code gives a convergent solution. In all the simulations the enclosed area and the perimeter are well conserved. A good conservation is achieved for higher κ_p and smaller n. n_x does not affect the vesicle area and perimeter conservation.

Fig. 3.7 shows the computed equilibrium shape for different reduced volumes. Here again we used the same physical parameters as in Fig. 3.6:

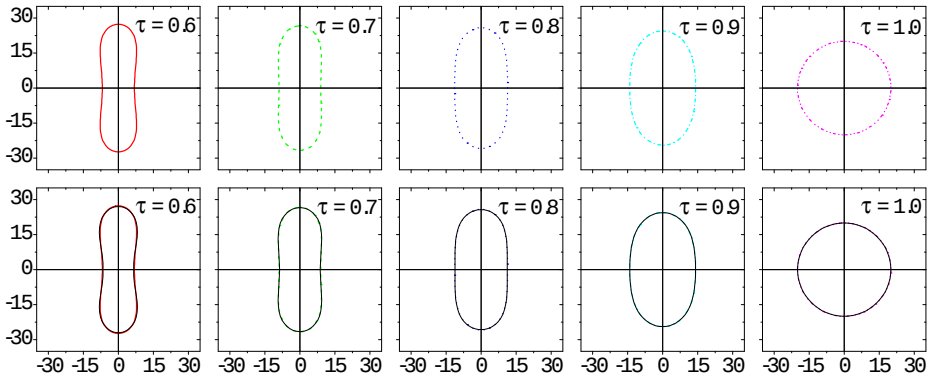

Fig. 3.7: Computed vesicle equilibrium shapes for different values of the reduced volume. On the top row the shapes computed using the lattice-Boltzmann method for each vesicle reduced volume. On the bottom row, for comparison purpose, the same vesicle shapes and their corresponding shapes computed using the boundary integral method (the black solid line).

$Re = Ca = 0$, $R_0 = 20$ and $R_0/W = 0.1$. For the numerical parameters we use: $n = 100$, $n_x = 200$ and $\kappa_p = 8$. The obtained shape for each given reduced volume is compared to its corresponding shape obtained by the boundary integral method (the black solid lines in Fig. 3.7). For a given reduced volume, the computed equilibrium shapes obtained by the two numerical methods are undistinguishable, especially at higher values of the reduced volumes.

Advantages

- Simplicity of the algorithm compared to other classical computation fluid dynamics (CFD) methods based on finite element methods,
- Straightforward implementation steps,
- Ability to simulate fluid flow in microfluidic devices since complex geometries can be easily implemented,
- Ability to be parallelised because of its local aspect.

Drawbacks

- Time consuming simulations.

3.3 Small deformation theory

We introduce now another interesting alternative to solve the vesicle problem analytically in some situations. Solutions are obtained approximately if one assumes that the shape is close to a sphere. Having analytical results is important in order to guide numerical results. On the other hand they provide an attractive basis for understanding underlying physical phenomena. In the small deformation theories, dynamics and deformation of a particle, due to an external applied flow, are obtained by performing an expansion around a simple geometry, namely a spherical shape (vesicles [17, 25, 53], droplets [54, 55] and capsules [56, 57]).

3.3.1 The vesicle shape

The surface of the vesicle, in the spherical coordinates ($\theta \in [0, \pi]$ and $\phi \in [0, 2\pi[$), is determined by the vector position [17]:

$$\mathbf{R}(\theta, \phi) = R_0 \left[1 + \epsilon f(\theta, \phi)\right] \mathbf{e}_\mathrm{r}, \tag{3.39}$$

where ϵ is a small parameter related to the vesicle excess area Δ by the relation $\epsilon = \sqrt{\Delta}$, and which is used as an expansion parameter for the vesicle shape deviation from a sphere [23, 58]. The excess area is defined as $\Delta = A - 4\pi R_0^2$, and measures the excess area from a sphere. It is related to the reduced volume τ (see Eq.2.9) by

$$\Delta = 4\pi[\tau^{-2/3} - 1] \tag{3.40}$$

$\Delta = 0$ ($\tau = 1$) corresponds to a sphere. Small Δ corresponds to the quasi-spherical limit.

The shape function f is decomposed on spherical harmonics $Y_n^m(\theta, \phi)$ as:

$$f(\theta, \phi) = \sum_{n=0}^{+\infty} \sum_{m=-n}^{n} F_{n,m}(t) Y_n^m(\theta, \phi), \tag{3.41}$$

where $F_{n,m}$ is a time-dependent amplitude of the corresponding mode, the evolution equations of which will be analyzed.
Exapnding the geometrical quantities associated to the vesicle around a sphere, we get [53]:

- *Vesicle surface*

$$A = R_0^2 \left(4\pi \left(1 + \frac{F_{0,0}}{\sqrt{4\pi}} \right)^2 + \sum_{n=1}^{+\infty} \sum_{m=-n}^{n} |F_{n,m}|^2 \left(1 + l(l+1)/2 \right) \right), \tag{3.42}$$

- *Vesicle volume*

$$V = R_0^3 \left(\frac{4\pi}{3} \left(1 + \frac{F_{0,0}}{\sqrt{4\pi}} \right)^3 + \sum_{n=1}^{+\infty} \sum_{m=-n}^{n} |F_{n,m}|^2 \right). \tag{3.43}$$

The amplitude $F_{0,0}$ can be expressed in terms of the other amplitudes, via the vesicle volume conservation constraint [17, 23, 53]:

$$F_{0,0} = -\sum_{n=1}^{+\infty} \sum_{m=-n}^{n} \frac{|F_{n,m}|^2}{\sqrt{4\pi}}, \tag{3.44}$$

inserting this into Eq. 3.42 the excess area becomes:

$$\Delta = \sum_{n=1}^{+\infty} \sum_{m=-n}^{n} |F_{n,m}|^2 \frac{(l+2)(l-1)}{2}. \tag{3.45}$$

Later the mode Y_1^m is omitted, since we are not interested in the translation of the vesicle. Since we consider a vesicle under simple linear shear flow only the spherical harmonics of order $n = 2$ survive [17]. This is sufficient in order to capture the basic features of dynamics. Indeed, as shear flow is linear its normal projection on a sphere (normal $\mathbf{n} \equiv \mathbf{R}/|\mathbf{R}|$; actually only normal displacement matter for shape modification) of radius unity provides quadratic forms in x, y and z. This quadratic form can be written on a second harmonics basis like

$$f(\theta, \phi) = \sum_{m=-2}^{2} F_{2,m}(t) Y_2^m = F_{2,-2} Y_2^{-2} + F_{2,0} Y_2^0 + F_{2,2} Y_2^2, \tag{3.46}$$

with,

$$Y_2^{-2}(\theta, \phi) = \frac{1}{4} \sqrt{\frac{15}{2\pi}} \sin^2 \theta e^{-2i\phi}, \tag{3.47}$$

$$Y_2^0(\theta, \phi) = \frac{1}{4} \sqrt{\frac{5}{\pi}} \left(3\cos^2 \theta - 1 \right), \tag{3.48}$$

$$Y_2^2(\theta, \phi) = \frac{1}{4} \sqrt{\frac{15}{2\pi}} \sin^2 \theta e^{2i\phi}. \tag{3.49}$$

The amplitude $F_{2,m}(t)$ are time-dependent quantities whose determination is achieved by solving the flow equations together with boundary conditions at the membrane. The knowledge of the equations obeyed by these amplitudes determines the instantaneous shape of a vesicle, and its subsequent evolution. Since these amplitudes depend on time only (the spatial dependence on shape is encoded in the spherical harmonics), the corresponding evolution equations are ordinary non linear differential equations. In some cases these equations can be solved analytically, otherwise we have resort to a numerical solution which is quite straightforward manner, as discussed below.

Note that we have omitted in Eq. (3.46) harmonics $Y_2^{\pm 1}$ since we analyze dynamics only in the plane of the shear flow, that is to say $Y_2^{\pm 1} = 0$ at $\theta = \pi/2$; the shear plane is the $x - y$ one.

3.3.2 Hydrodynamical equations

We briefly recall the flow equations. We consider the small Reynolds number limit which is consistent with most of available experimental data on vesicles. Hence, the internal (Ω_{int}) and the external (Ω_{ext}) fluids flow is governed by the Stokes equations:

$$\begin{cases} \eta_{\text{int}} \nabla^2 \mathbf{u}_{\text{int}}(\mathbf{r}) - \nabla p_{\text{int}}(\mathbf{r}) = 0, \\ \nabla \cdot \mathbf{u}_{\text{int}}(\mathbf{r}) = 0, \end{cases} \quad \mathbf{r} \in \Omega_{\text{int}} \tag{3.50}$$

and

$$\begin{cases} \eta_{\text{ext}} \nabla^2 \mathbf{u}_{\text{ext}}(\mathbf{r}) - \nabla p_{\text{ext}}(\mathbf{r}) = 0, \\ \nabla \cdot \mathbf{u}_{\text{ext}}(\mathbf{r}) = 0, \end{cases} \quad \mathbf{r} \in \Omega_{\text{ext}} \tag{3.51}$$

respectively. Moreover, since the membrane is considered as an incompressible fluid its velocity field has to fulfill the condition (free surface divergence condition):

$$(\delta_{ij} - n_i n_j)\, \partial_i u_j(\mathbf{r}) = 0, \quad \mathbf{r} \in \partial\Omega, \tag{3.52}$$

where η is the viscosity, p is the pressure and $\mathbf{u}$ the velocity. The subscripts "int" and "ext" are used to distinguish between quantities associated with the internal and the external fluids, respectively.
Equations. (3.50), (3.51) and (3.52) are solved by taking into consideration the boundary conditions: 1 - The stress jump $\left(\sigma_{ij}^{\text{ext}} - \sigma_{ij}^{\text{int}}\right) \mathbf{n} + \mathbf{F} = 0$ ($\sigma_{ij} = -p\delta_{ij} + \eta(\partial_i u_j + \partial_j u_i)$ is the stress tensor) and 2 - The continuity of the velocity $\mathbf{u}_{\text{ext}} = \mathbf{u}_{\text{int}}$ across the membrane and 3 - The external fluid flow, at distances far from the location of the vesicle membrane, is undisturbed. Solutions are obtained following the Lamb's procedure [59], their expression are given by:

- For the external fluid as:

$$\mathbf{u}_{\text{ext}}(\mathbf{r}) = \sum_{n=0}^{\infty} \left[\nabla \chi^{\text{ext}}_{-n-1} \times \mathbf{r} + \nabla \phi^{\text{ext}}_{-n-1} - \frac{n-2}{2n(2n-1)} r^2 \nabla p^{\text{ext}}_{-n-1} + \frac{n+1}{n(2n-1)} \mathbf{r} p^{\text{ext}}_{-n-1} \right]. \tag{3.53}$$

  where $\chi^{ext}_{-n-1} = r^{-n-1} Q_n$, with Q_n depend on the angular variables only and are decomposed, in the most general case, on an infinite series of surface spherical harmonics. However, as stated above, in a linear shear flow, only second order harmonics are excited. Similar expressions hold for ϕ^{ext}_{-n-1} and p^{ext}_{-n-1}.

- For the internal fluid as:

$$\mathbf{u}_{\text{int}} = \sum_{n=0}^{\infty} \left[\nabla \chi^{\text{int}}_{n} \times \mathbf{r} + \nabla \phi^{\text{int}}_{n} + \frac{n+3}{2(n+1)(2n+3)} r^2 \nabla p^{\text{int}}_{n} - \frac{n}{(n+1)(2n+3)} \mathbf{r} p^{\text{int}}_{n} \right] \tag{3.54}$$

  where for χ^{int}_n, ϕ^{int}_n and p^{int}_n the r-depedence is r^n with angular functions.

The pressure distribution is represented by $p = \sum_n p_n$ with p_n are solid spherical harmonics. The coefficeint of the expansion on spherical harmonics of the functions Q_n, and so on, are determined from velocity and forces boundary conditions on the membrane.

3.3.3 Shape evolution equations

The evolution in time of the vesicle shape configuration, under an applied shear flow, is given by the evolution of the $F_{i,j}$ modes (see Ref. [23]). In the present work we make use of the so-called post-expansion theory which consists in keeping in the full evolution equations the leading terms in a consistent manner [23]. We set [17] $F_{2,2} = \mathcal{R} e^{-2i\Psi}$, Ψ coincides with the orientation angle of the vesicle long axis with respect to the flow direction, and $\mathcal{R}$ is the amplitude of the vesicle deformation. It may be convenient, instead of using $\mathcal{R}$, to use Θ [24] defined by $2\mathcal{R} = \cos\Theta$ with $0 \leqslant \Theta < \pi$. But hereafter we use the expression $R = \frac{\sqrt{\Delta}}{2} \cos\Theta$, to absorb ϵ appearing in Eq. 3.39, in order to quantify the shape deformation (since this corresponds to the entire amplitude deformation). Following the post-expansion theory [23] we have

$$\begin{aligned} T \frac{\partial \Theta}{\partial t} &= -S \sin\Theta \sin 2\Psi + \cos 3\Theta \\ &\quad + \Lambda_1 S \sin(2\Psi)(\cos 4\Theta + \cos 2\Theta), \end{aligned} \tag{3.55a}$$

$$T\frac{\partial \Psi}{\partial t} = \frac{S}{2}\left[\frac{\cos 2\Psi}{\cos \Theta} - \Lambda\right], \tag{3.55b}$$

with

$$S = \frac{7\sqrt{3}\pi}{9}\frac{Ca}{\Delta}, \tag{3.56}$$

$$T = \frac{7\sqrt{10\pi}}{720}\frac{(23\lambda + 32)\, Ca}{\gamma\sqrt{\Delta}}, \tag{3.57}$$

$$\Lambda = \frac{1}{240}\sqrt{\frac{30}{\pi}}\,(23\lambda + 32)\,\sqrt{\Delta}, \tag{3.58}$$

$$\Lambda_1 = \frac{1}{28}\sqrt{\frac{10}{\pi}}\frac{\lambda - 2}{23\lambda + 32}\sqrt{\Delta}. \tag{3.59}$$

The above coefficients are related to the three independent parameters Δ, λ and Ca already introduced before. We can rescale time by T, so we are left with three independent parameters S, Λ and Λ_1. Below, we shall use either of the two sets (Δ, λ, Ca) or (S, Λ, Λ_1). Equations. (3.55a) and (3.55b) are symmetric under the transformations:

$$\left\{\begin{array}{l}\Theta \longrightarrow \Theta \\ \Psi \longrightarrow \Psi + \pi\end{array}\right. \quad \text{and} \quad \left\{\begin{array}{l}\Theta \longrightarrow \pi - \Theta \\ \Psi \longrightarrow \Psi + \frac{\pi}{2}\end{array}\right. \tag{3.60}$$

The first term on the right hand side of Eq. (3.55a) is of order $1/\epsilon^2$ (recall that $\epsilon = \sqrt{\Delta}$), the second one of order 1 and the final one of order $1/\epsilon$. The first contribution $(1/\epsilon^2)$ arises in the leading theory [17], the second (of order 1) is the additional term added in [24], while the full calculation shows the need for the third term $(1/\epsilon)$. The reason for this has been discussed at length in [23]. Below the relevance of this term for the dynamics of the vesicle is presented and discussed.

Equation (3.55b) provides the evolution of the vesicle inclination angle Ψ $(-\pi \leq \Psi \leq \pi)$. For a given set of solutions $\{\Theta(t), \Psi(t)\}$ we obtain $F_{2,2} = |R|e^{(-i2\Psi)}$, $F_{2,-2} = |R|e^{(i2\Psi)}$ and also $F_{2,0}$ via the area conservation constraint (see Eq.(3.45)), $2F_{2,0}^2 + 4|F_{2,2}|^2 = 1$, and this leads us to the determination of the vesicle shape configuration.

Advantages

- Ability to get analytical expressions and thus capture the physics,
- Fast time calculations (only ordinary differential equations (ODE) are solved numerically).

Drawbacks

- Limited to the small deformation regimes,
- Implementing bounding walls is not easy in practice.

4. VESICLE DYNAMICS UNDER SHEAR FLOW

The last chapter has dealt with different ways of solving the vesicle problem. Now we present the outcomes. We first begin with the analytical results based on the small deformation theory presented in the previous chapter. Then dynamics in confined geometries is studied on the basis of the lattice Boltzmann simulation discussed also in the previous chapter.

Regarding the first part of the study dynamics of a single neutrally buoyant vesicle, as a response to an external applied shear flow, is studied analytically in the limit of low Reynolds number. In particular we are interested to investigate how the vesicle dynamics (its orientation and its shape deformation) is related to three key dimensionless parameters: the excess area (the degree of deflation), the viscosity contrast (between the internal and external fluids) and the capillary number (the ratio of the time scales needed by the vesicle to relax to its equilibrium shape after cessation of the flow and the one of the imposed flow; inverse of shea rate). Secondly we study numerically the effect of the confinement on the vesicle dynamics. In particular we investigate how the vesicle's steady inclination angle in the tank-treading regime and the rheology depend on the degree of confinement (the ratio of the effective radius of the vesicle divided by the half width of the channel). These studies will shed light on vesicle dynamics at the individual level and their impact on rheology.

4.1 Unbounded geometry

The following results are obtained by solving numerically Eqs. (3.55a) and (3.55b), that are non-linear ordinary differential equations of first-order, using Maple. The phase-diagram (Fig. 4.1a) contains three domains corresponding to the three known vesicle hydrodynamical regimes, under shear flow: tank-treading (blue area), vacillating-breathing (violet area) and tumbling (red area). The phase diagram is drawn using Eqs. (3.55a) and (3.55b). Steady (tank-treading) to unsteady (tumbling or vacillating-breathing) transition border, in the phase-diagram, is captured as follows: (i) The bifurcation from tank-treading to tumbling (which happens at low Ca) corresponds to a saddle node bifurcation. (ii) The bifurcation from tank-treading

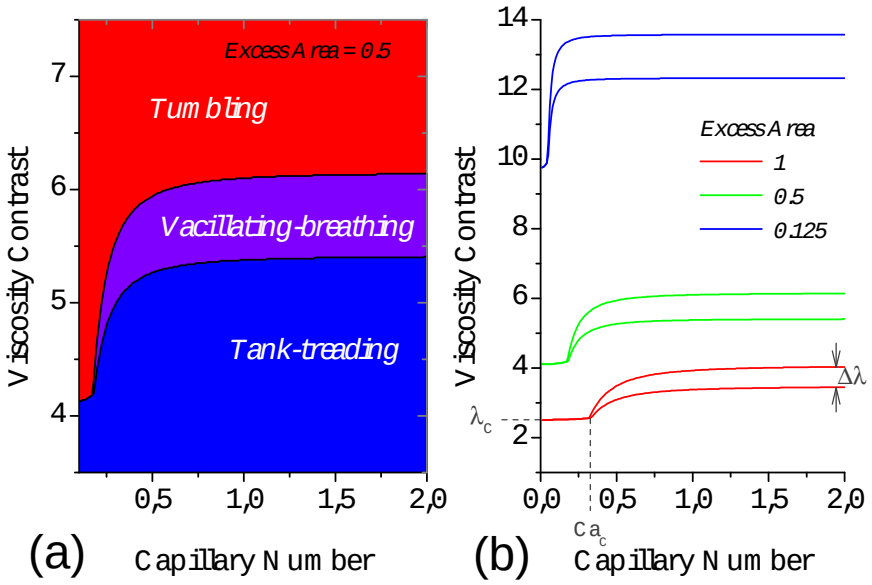

Fig. 4.1: (a) Phase diagram giving the known vesicle dynamical regimes, exhibited under shear flow, as a function of the capillary number and the viscosity contrast, (b) Evolution of the phase diagram borders location under the effect of varying the value of the vesicle excess area.

to vacillating-breathing is of Hopf type, and is captured when at least one eigenvalue ω of the stability matrix of the set of fixed points has a real part which becomes positive (we look for perturbation of the fixed point as $\sim e^{\omega t}$). Since the occurrence of vacillating-breathing mode corresponds to a Hopf bifurcation, the real part of ω vanishes, while it imaginary part is non zero.

The border separating the two unsteady regimes (tumbling and vacillating-breathing) is obtained numerically. Tumbling is the continuation of the vacillating-breathing mode when Ψ reaches $\pm\pi/4$.
At low deformation regime ($Ca < 1$) the transition from tank-treading to tumbling is direct and it occurs via a saddle-node bifurcation (in this range of Ca no vacillating-breathing mode). At higher deformation regime ($Ca > 1$), there exist a vacillating-breathing regime between tank-treading and tumbling regions.

The phase-diagram, for the parameters ranges used in Fig. 4.1a, looks simple and it can be characterized by three quantities: the critical viscosity contrast (λ_C), the critical capillary number (Ca_C) and the thickness of the

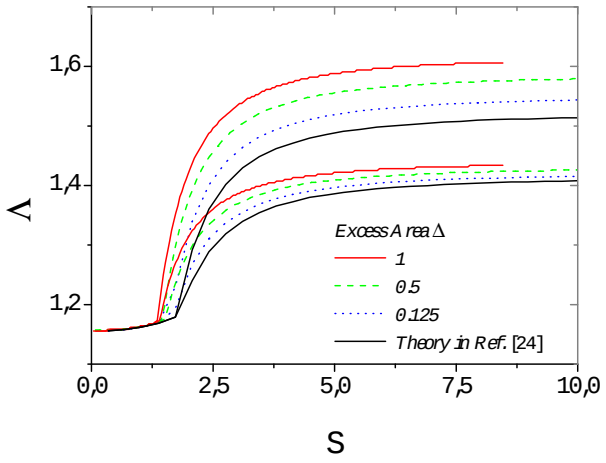

Fig. 4.2: Comparison between the two phase diagrams obtained by the present theory and the one reported in [24] for three different values of the excess area. Here, in both cases, the phase-diagram is drawn in the $S - \Lambda$ plane (as in [24] for comparison purposes).

vacillating-breathing domain ($\Delta\lambda$) at higher capillary numbers (as it is shown in Fig. 4.1b).

Figure 4.1b shows the evolution of the domains border location, in the phase-diagram, when varying the value of the excess area. Decreasing the excess area towards vanishing values (towards the spherical vesicle limit) induces a shift of Ca_C to the left of the phase-diagram (i.e. to smaller values) and to an increase of both λ_C and $\Delta\lambda$. The increase of λ_C when decreasing Δ was already reported in literature [12–14]. The decrease of Ca_C and the shift of the vacillating-breathing domain to higher viscosity (as it can be seen in Fig. 4.1b), when decreasing Δ were also observed by Noguchi and Gompper [60]. The increase of $\Delta\lambda$ for smaller values of Δ does not mean that vacillating-breathing mode becomes important for quasispherical vesicles (in comparison with more deflated ones) as it will be shown and discussed below (in the subsection *vacillating-breathing*).

Figure 4.2 shows a comparison between the phase-diagram of the present work and that obtained in Ref. [24]. The location of the borders, separating the three vesicle dynamical regimes under shear flow, is different in both works. In fact the additional term (with Λ_1) appearing in the right-hand side of Eq. (3.55a) makes the border location, in the phase-diagram, sensitive to the excess area parameter. This contrasts with the result of Lebedev *et al* [24] according to which vesicle dynamics, under shear flow, depends only

on two dimensionless parameters S and Λ. In Figure 4.2 it can be seen that when decreasing Δ, the borders obtained by the present theory (the colorful curves) shift towards the ones obtained in [24] (the solid black curves).

Note that a value of $\Delta = 1$ corresponds to only 8% of relative excess area. We could thus, legitimately, use the relative excess area as a dimensionless small parameter in the expansion in order to stress the validity of a perturbative scheme. This is more visible when using the reduced volume ν to quantify the deflation. This is defined as the ratio between the actual volume V and the volume of a sphere having the same area as the actual shape, that we denote as V_0. Thus $\nu = V/V_0$, or

$$\nu = \frac{V}{\frac{4\pi}{3}[A/4\pi]^{3/2}}, \tag{4.1}$$

and its relation to the excess area is $\Delta = 4\pi[\nu^{-2/3} - 1]$. $\Delta = 1$ corresponds to $\nu \sim 0.93$. Thus, when considering $\Delta = 1$ we must keep in mind that in a perturbative sense this is a small quantity. Most of available experimental data are in the range [14, 15, 25] $\Delta = 0.5 - 1.5$. It will be seen later that the effect of the third parameter Λ_1 (when keeping S and Λ fixed) has a more dramatic effect on the amplitude of the vacillating-breathing mode.

4.1.1 Tank-treading

We found that the steady inclination angle decreases with increasing the viscosity contrast (Fig. 4.3a), an already known phenomenon reported in literature [13, 16, 61, 62]. Moreover, we observed that at high deformation regime, i.e. when the capillary number is greater than unity, the steady inclination angle continues to decrease until reaching small negative angles. This effect was briefly observed in [23] by using equation (52) in the same reference.

Figure 4.3b shows, for a given set of viscosity ratios, the variation of the steady inclination angle when varying the capillary number (or shear rate). At low shear rate ($Ca \ll 1$), the steady inclination angle decreases with increasing the capillary number. This decrease is quite important (see Figure 4.3b for $\lambda = 2$) where it can attain a factor of about two. This behavior was briefly commented in the experiments of Ref. [25]. A systematic experimental analysis of this fact is lacking.

At higher deformation ($Ca \gg 1$), the variation of the steady inclination angle with increasing the capillary number, becomes smaller and smaller until reaching a saturation state. For a vesicle without viscosity contrast ($\lambda = 1$), its steady inclination angle has already reached a plateau for the range of the capillary numbers used in Fig. 4.3. This is in good agreement

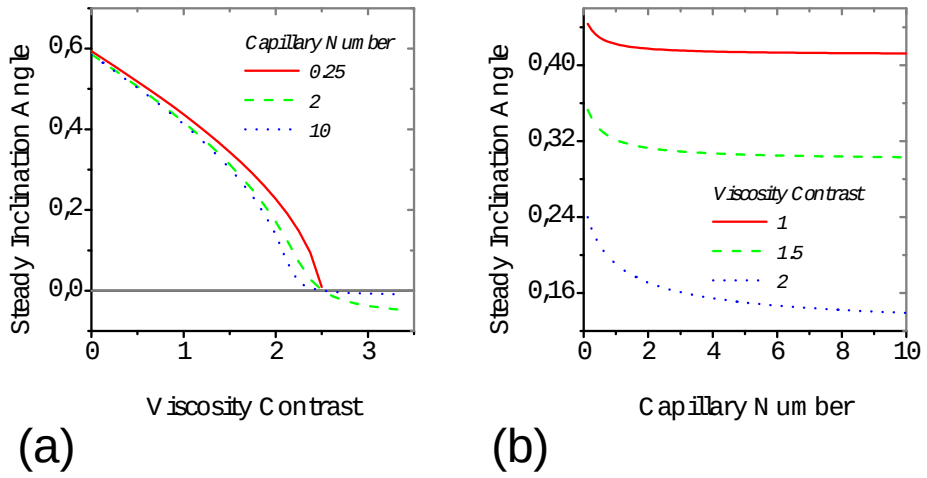

Fig. 4.3: The steady inclination angle in radian of a vesicle, performing tank-treading, (a) versus the viscosity contrast for different values of the capillary number and (b) versus the capillary number for different values of the viscosity contrast. Here $\Delta = 1$.

with numerical simulations results reported in [43]. In that wok it is stated that the inclination angle of a tank-treading vesicle, under shear flow, is independent of the applied shear rate value; however, in that work, tank-treading of vesicles having a viscosity contrast and under smaller shear rates was not reported.

This behavior (decrease of the angle with C_a) is revealed in the context of the higher order expansion [23] dealt with here. This effect is not captured in the leading order theory [17], where it was found that the steady inclination angle does not depend on the capillary number ($\Psi_0 = \pm\frac{1}{2}\cos^{-1}\left[\frac{23\lambda+32}{120}\sqrt{\frac{15\Delta}{2\pi}}\right]$).

4.1.2 Tumbling

At large enough Ca (i.e. when a vacillating-beathing mode exists, owing to a significant vesicle deformation; see Figure 4.1) the tumbling period decreases slowly with increasing the viscosity contrast (Fig. 4.4a; cases with $Ca = 1$ and 2; see phase-diagram for $\Delta = 1$ in Fig.4.1). It is only in the small Ca regime (i.e. when there is direct bifurcation from TT to TB; see Fig.4.1) that the period varies abruptly with λ (with infinite period at the transition point). To our knowledge, such behavior of the tumbling angular period (of a vesicle)

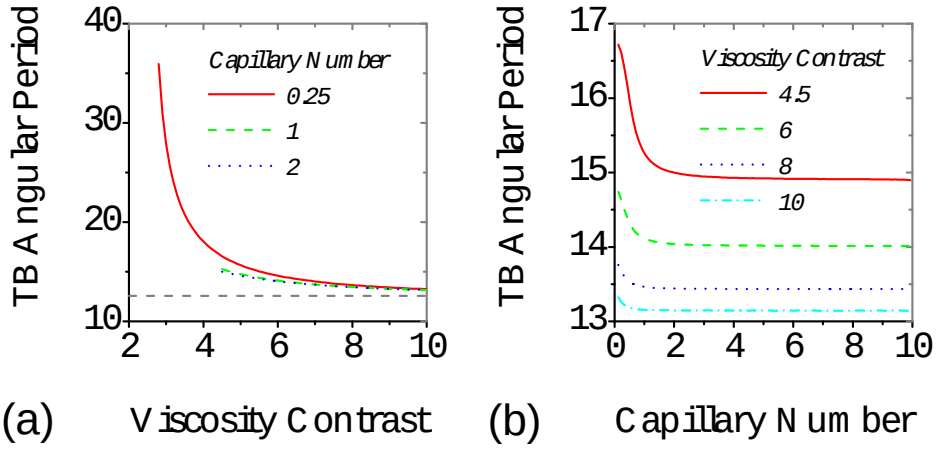

Fig. 4.4: The period of vesicle tumbling (rescaled by γ), (a) versus the viscosity contrast for different values of the capillary number. The measurements are taken starting from the viscosity contrast, corresponding to the threshold of the transition to tumbling regime. The dash gray line corresponds to the period of a rotating rigid body [63]; and (b) versus the the capillary number for different values of the viscosity contrasrt. Here $\Delta = 1$.

with varying the viscosity contrast was not reported so far in literature. The dash gray line in Fig. 4.4a corresponds to the period of a rotating rigid body with the frequency $\Omega = \gamma/2$ [63], all TB angular period curves tend to this value at higher values of the viscosity contrast. Deformation of vesicles, with small viscosity contrast, slows down their tumbling motion.

Variation of the tumbling period when varying the capillary number, for different values of the viscosity contrast, has also been investigated (Fig. **??**b). At lower deformation regime ($Ca \ll 1$), a decrease of the tumbling period with increasing the capillary number is observed for all values of the viscosity contrast, but that decrease is quite small, it varies in a range of 6 to 11%. At a higher deformation regime ($Ca \gg 1$) more precisely in the range of 2 and for $\Delta = 1$, the period ceases to depend on the capillary number and it becomes practically constant, whatever the value of the viscosity contrast is. Noguchi and Gompper [60] have also measured numerically the period (the frequency in their paper), but they observed an increase of this quantity when increasing the capillary number, which disagrees with our observation. The non-variation of the period when increasing the capillary number to higher values is also observed numerically using boundary integral method in three

dimensions (to be reported elsewhere).

4.1.3 Vacillating-breathing

Vacillating-breathing period

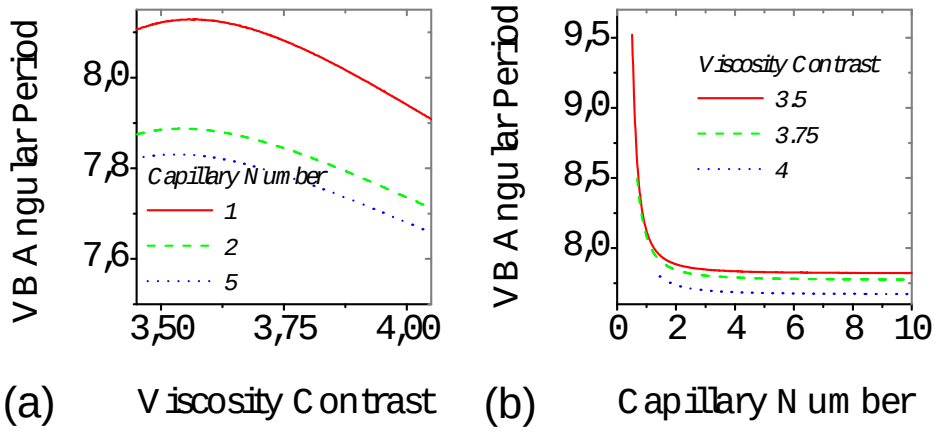

Fig. 4.5: The period of vacillating-breathing (rescaled by γ), (a) versus the viscosity contrast for different values of the capillary number and (b) versus the capillary number for different values of the viscosity contrast. Here $\Delta = 1$.

The vacillating-breathing period decreases with increasing the viscosity contrast, after exhibiting a maximum (Fig. 4.5a) in the vicinity of the transition from the tank-treading regime to the vacillating-breathing one.

Fig. 4.5b shows the vacillating-breathing angular period versus the capillary number, for different values of the viscosity contrast. Only in the vicinity of the transition from tumbling to the vacillating-breathing (please refer to Fig.4.1 for $\Delta = 1$ when looking to data in Fig. 4.5b in order to locate the various regimes) does the period undergoes an abrupt fall. Upon increasing Ca beyond a typical value of about 2 the period exhibits a plateau. Thus here again, we observe that the angular period has a plateau for higher values of Ca. This is in disagreement with the observation in Ref. [60] in which the period of the vacillating-breathing (the frequency in the paper) where significant decreases with increasing the capillary number is reported. In our case, a significant decrease is only observed in the vicinity of the tumbling-vacillating-breathing transition, but no significant variation is found beyond

$Ca \sim 2$. The fact that the period is insensitive to Ca (for Ca of order of, or higher than, 2) is confirmed by full three dimensional simulations based on the boundary integral formulation, to be reported elsewhere.

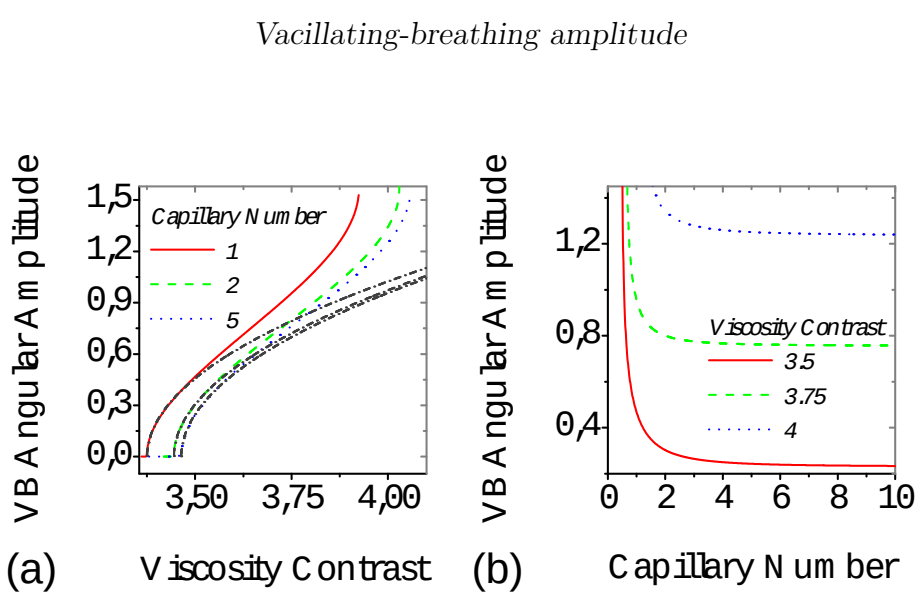

Fig. 4.6: The angular amplitude, in radian, of vacillating-breathing, versus the viscosity contrast for different values of the capillary number. The dashed-dotted lines are fits of the angular amplitude with a square root law ($\backsim \sqrt{\lambda - \lambda_C}$) (a); and versus the capillary number for different values of the viscosity contrast (b). Here $\Delta = 1$

Let us investigate now a quantity which is quite sensitive to the three dimensionless parameters, namely the amplitude of the vacillating-breathing mode. The vacillating-breathing angular amplitude $\Delta\Psi$ increases with increasing the viscosity contrast, as it is depicted in Fig. 4.6a. It tends to the limit $\pi/2$ (in the right side in Fig. 4.6a) when the viscosity contrast tends to the threshold of the transition to the tumbling regime. Note that the amplitude is defined here as the absolute value of difference between the maximum and the minimum of $\Psi(t)$. Tumbling occurs when the minimum Ψ_{min} or the maximum angles Ψ_{max} tend to the values $-\pi/4$ and $+\pi/4$, respectively. When the viscosity contrast tends to the threshold value of the transition to the tank-treading regime (in the left side in Fig. 4.6a), the minimum and the maximum angles values both tend to zero, and therefore the amplitude vanishes.

The fact that amplitude goes to zero at the tanktreading and vacillating-breathing when decreasing λ (at fixed C_a) in a continuous manner is observed for all the parameter values explored so far. That is to say, the bifurcation from tank-treading to vacillating-breathing is supercritical (in contrast to a subcritical bifurcation; a dynamical analogue of a first order transition). This feature is further investigated by plotting the amplitude as a function of λ. A typical behavior is shown in Fig. 4.6a. The amplitude is well fitted with a square root law ($\Delta\Psi \backsim \sqrt{\lambda - \lambda_C}$) in the vicinity of the bifurcation, a prototypical result for a supercritical (or pitchfork) bifurcations.

We also found that the absolute values of the maximum and the minimum angles are different $|\Psi_{min}| \neq |\Psi_{max}|$ with $|\Psi_{min}| > |\Psi_{max}|$. In fact, during vacillating-breathing, the vesicle longest axis oscillates around a small negative angle (in contrast to RBCs that oscillate with respect to a positive angle [64]). This angle has the value of the steady inclination angle measured in the tank-treading regime, just before the vacillating-breathing threshold, for the same capillary number. Eigenvalues analysis of the stability matrix of the non-linear equations (3.55a) and (3.55b) shows that this angle corresponds to a fixed point that changes its nature from stable (in the tank-treading regime) to an unstable spiral when the vacillating-breathing threshold is crossed. This is a typical situation of a supercritical Hopf bifurcation. Figure 4.6b shows the vacillathing-breathing angular amplitude versus the capillary number for different values of the viscosity contrast. At smaller values of the capillary number, the amplitude decreases with increasing the capillary number until it reaches a plateau, at higher values of the capillary number. The same behavior was also reported in [60].
Figure 4.7 presents the variation of the angular and the deformation amplitudes with the excess area for the vacillating-breathing regime. The values of the parameters S and Λ used in Fig. 4.7 are chosen in a such way to be in the vacillating-breathing regime domain, in the phase-diagram (Fig. 4.2), for different values of Δ belonging to the range between 0.125 and 1 (a typical range in experiments [14–16, 25, 26]). The angular amplitude decreases, while the deformation amplitude increases, when increasing the excess area. That means that for more deflated vesicles the deformation variation is important compared to the angular oscillations. The opposite situation occurs for quasi-spherical vesicles (more swollen vesicle).

These results confirm again the importance of the excess area as a third control parameter, on the vesicle dynamics, besides S and Λ. The present analysis shows that for a fixed set of S and Λ, varying the excess area induces ample variations in the deformation and the angular amplitudes of a vacillating-breathing mode.

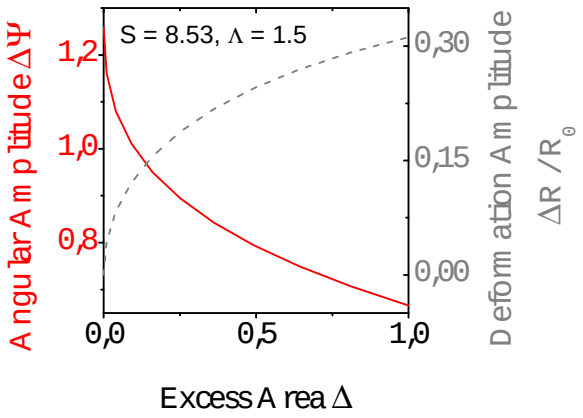

Fig. 4.7: Variation of both the angular in radian (the left axis) and the deformation rescaled by R_0 (the right axis) amplitudes with the excess area, for a given set of S and Λ parameters.

Vacillating-breathing limit-cycles

Figure 4.8 shows the limit-cycles of a vesicle performing vacillating-breathing, under shear flow, for different sets of parameters. A point belonging to a limit cycle (e.g. the point A in Fig. 4.8a) represents the instantaneous vesicle inclination angle and the respective deformation.

In Fig. 4.8a we show a typical limit cycle for the vacillating-breathing obtained when varying Δ, while keeping S and Λ fixed, as in Fig. 4.7. Increasing the excess area induces a shift of the limit cycle to higher deformation regions, and to small amplitude angular oscillations.

It must be noted that when varying the capillary number, in the range used in Fig. 4.8b, while keeping λ and Δ fixed, the configuration of the limit-cycle does not exhibit a dramatic change. Only small variations in the deformation and the angular amplitudes are observed.

Figure 4.8c shows the evolution of the limit cycle when varying only the viscosity contrast. Increasing the viscosity contrast induces an increase of the deformation and the angular amplitudes. The same information is presented in Fig. 4.8d, in the $\Theta - \Psi$ Atlas.

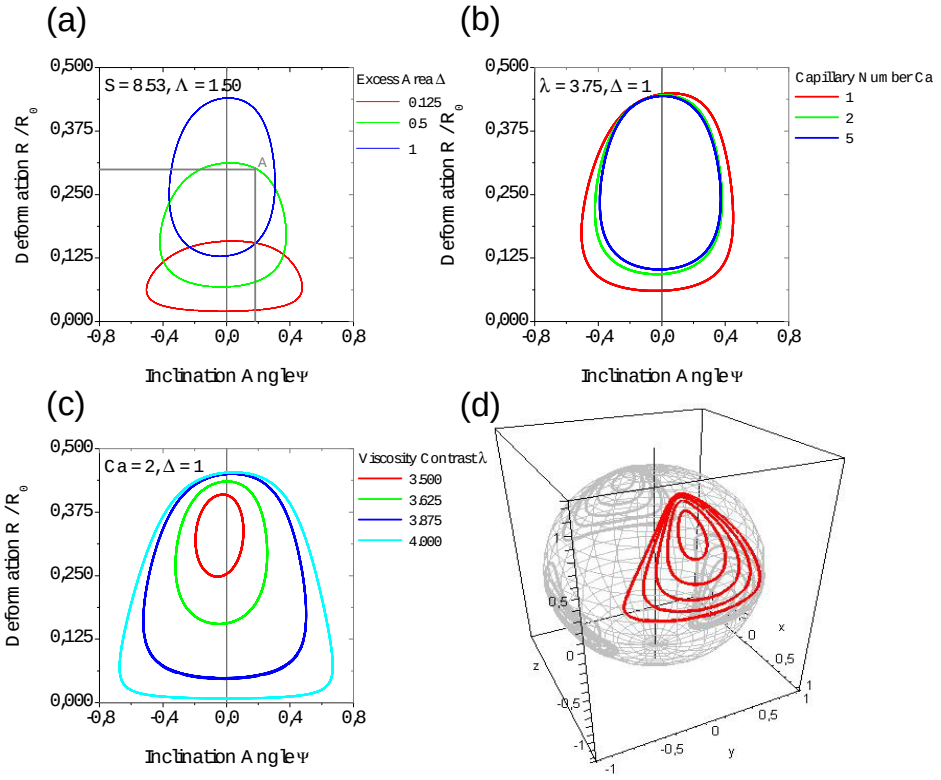

Fig. 4.8: Evolution of the limit-cycle configuration (in the $R - \Psi$ plane) of a vacillating-breathing vesicle, under shear flow, when varying either the excess area (a), the capillary number (b) or the viscosity contrast (c). Evolution of the limit-cycle configuration in the Atlas $\Theta - \Psi$ when varying the viscosity contrast.

4.2 Tank-treading of a confined vesicle

The analytical work presented above was made possible at small deviation from a sphere. Also the flow was taken as unbounded. In confined geometries we need to resort to numerical methods. Now we would like to illustrate one of the presented methods, namely the LBM (Lattice-Boltzmann Method).

4.2.1 Effect of the reduced volume

A single isolated vesicle placed in an external suspending fluid subject to a simple shear induced by the motion of the bounding walls with the same ve-

locity but in opposite directions is simulated. Here we set the vesicle effective radius $R_0 = 30$ to acheive higher resolution and to have enough fluid nodes between the wall and the membrane in more confined situations. The width of the simulation box is set to $L = 2 \times n_x + 1 = 601$ to avoid any unphysical effects induced by the periodic boundary conditions.
In a such condition and in the absence of a viscosity contrast (between the internal and the external fluids) a vesicle performs tank-treading motion [12, 15, 43]. It deforms until reaching a steady fixed shape (deformed compared to the initial shape) with a long axis having a steady inclination angle with respect to the applied flow direction. The membrane of the vesicle undergoes a tank-treading like motion and so it generates a rotational flow of the internal enclosed fluid. Fig. 4.9 shows different physical quantities measured during tank-treading of a vesicle. The reached steady shapes for different values of the vesicle reduced volume is shown in Fig. 4.9a. The resulting streamlines inside and outside the vesicle, with reduced volume of $\tau = 0.90$, is shown in Fig. 4.9b. The internal fluid rotates due the tank-treading of the vesicle membrane that transfer motion to it. The external fluid flow exhibits recirculations in the right and in the left sides of the vesicle. Such recirculations do not occur and are not observed in the unbounded geometry case. They are observed for confined rotating hard spheres [65] and for hard ellipsoides [66]. Their pattern configuration evolution with the shape of the vesicle and degree of confinement is reported below. In Fig. 4.9c the steady inclination angle of the vesicle versus its reduced volume for two different given values of the degree of confinement is shown. The steady inclination (for both values of R_0/W) increases with increasing the reduced volume until reaching almost the value 45° which is the value of the steady inclination angle of a spherical vesicle in unbounded geometry. Such behavior is observed also for the unbounded geometry case [12, 15, 43]. For the values of the degree of confinement used here, the measured values of the steady angle are quantitatively different from the one that can be obtained using the boundary integral method simulations for the unbounded geometry case [13] (in a two-dimensional space). In Ref. [67] they report a good quantitative agreement between steady inclination angles computed both by the BIM and the LBM. But such collapse of data, with a slight deviation observed at small values of the reduced volumes, can be achieved by choosing a small width of the simulation box, but in such conditions we simulate accidentally the situation of an array of vesicles, seeing each other, and that results in a decrease of the measured inclination angle.
The membrane tank-treading velocity versus the reduced volume is shown in Fig. 4.9d. For the degree of confinement $R_0/W = 0.40$ the tank-treading velocity increases with increasing the reduced volume as this is also observed

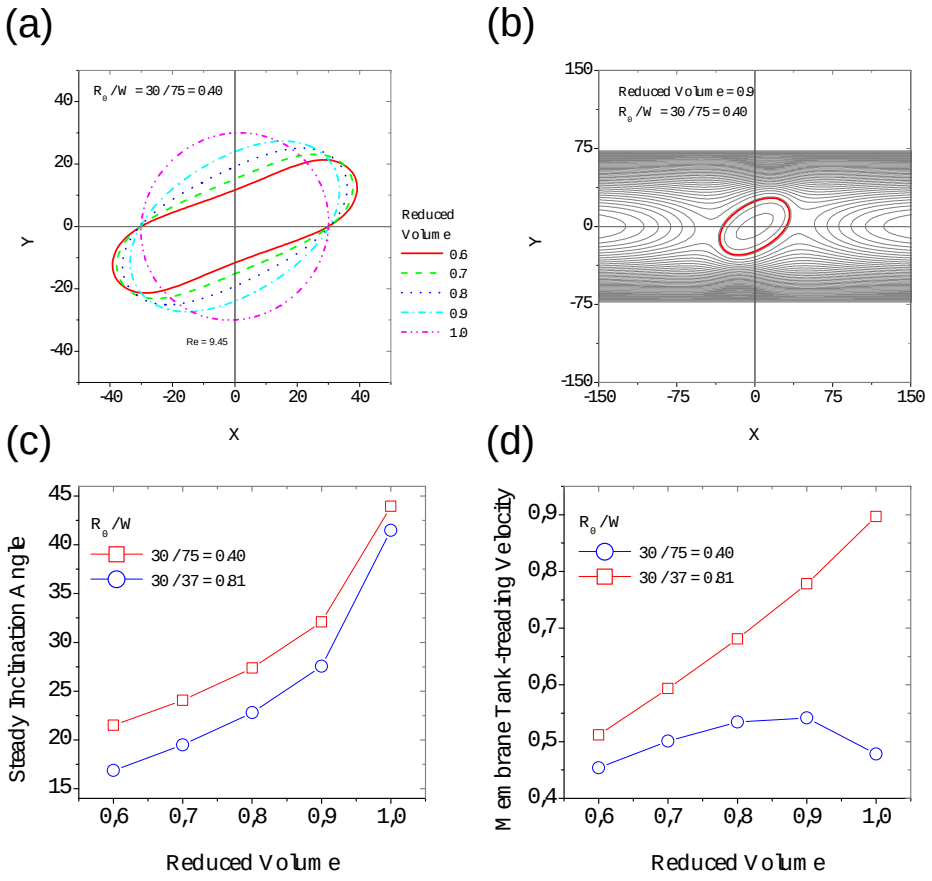

Fig. 4.9: Tank-treading of vesicles (with $R_0 = 30$) under shear flow ($Re = 9.45 \times 10^{-2}$ and $Ca = 1$) induced by two walls sliding with the same velocity but in opposite directions (a) final steady shapes of vesicles, with different reduced volumes, under shear flow. (a) streamlines inside and outside a vesicle ($\tau = 0.9$) performing a tanktreading motion in a fluid bounded by two walls at a distance $W = 151$, (c) tank-treading inclination angle verus the vesicle reduced volume for two degrees of confinement $R_0/W = 0.40$ and 0.81. (d) membrane tank-treading velocity (scaled with $2R_0/2$ the analytical solution of the rotation of a cylinder under shear flow in unbounded geometry) versus the reduced volume.

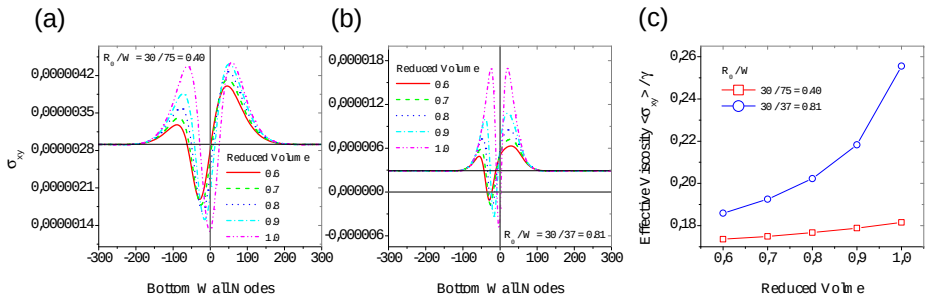

Fig. 4.10: The hydrodynamical stress exerted on the bottow wall and the viscosity of the system (vesilce and the suspending fluid). The hydrodynamical stress exerted on the bottom wall for different values of the vesicle reduced volume for two values of the degree of confinement R_0/W: 0.40 in (a) and 0.81 in (b). (c) the viscosity versus the vesicle reduced volume for the both values of the degree of confinement.

in the unbounded geometry case [12, 15, 43]. However for higher degrees of confinement $R_0/W = 0.81$, the tank-treading velocity does not vary anymore monotonously as in the previous case. It has a maximum around the value of $\tau = 0.85$ and gets lower value for $\tau = 1$. This behavior can be explained by the fact that at higher degrees of confinement, the amount of the external fluid able to flow from one side (the left) to the other side (the right) of the box by crossing the narrow region between the wall and the membrane is very small. Therefore, the external fluid flow does not participate much to generate the tank-treading motion of the vesicle.

The modified bounce back boundary condition of Ladd [49] implemented on the walls allows to measure the hydrodynamical stress field exerted by the fluid. Fig. 4.10 gives the measured hydrodynamical stress and the effective viscosity. The latter is defined as the ratio between the shear stress on the wall divided by the imposed shear rate. For a given shear rate, the presence of a vesicle modifies the applied shear stress on the wall. For a given value of the degree of confinement Figs. 4.10a or 4.10b, the hydrodynamical stress is important when placing vesicles with higher reduced volume, since the membrane approaches more and more the wall. For the reduced volume $\tau = 1$, the stress is symmetrical with respect to the vertical axis perpendicular to the walls and crossing the center of mass of the vesicle. Such symetrical shape of the stress curves for circular vesicles is observed for confined hard spheres. For deflated vesicles ($\tau \neq 1$) their corresponding stress curve has two unequal maxima and one minimum. The values of these maxima and

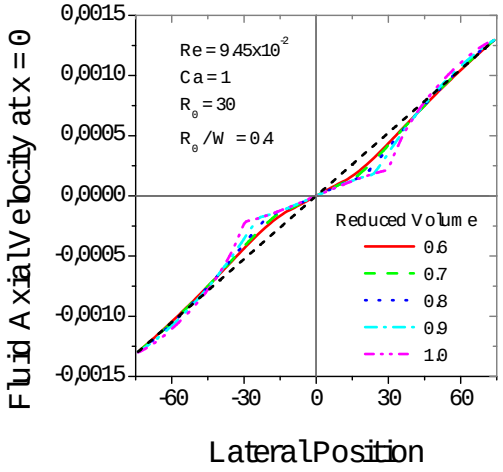

Fig. 4.11: Distubed flow velocity profile measured at $x = 0$ for different values of the vesicle reduced volume. The black solid line is the undisturbed applied shear flow profile $v_x = \gamma y$

minimum significatly deviates from the value $\eta\gamma$ (the black solid line) - the hydrodynamical stress in the absence of the vesicle - when increasing the reduced volumes. By comparing Figs. 4.10a and 4.10b, we conclude that the stress is important at higher degrees of confinement. At higher R_0/W we observe local region with negative hydrodynamical stress. Whether this is a physical fact or is rather related to the LBM is not completly understood. This question require more refined analysis before drawing a conclusive answer.

In Figs. 4.10c the viscosity of the suspending fluid in the presence of a vesicle is measured for different vesicle reduced volume. The viscosity increases when increasing the reduced volume. Higher viscosities for a given reduced volume is observed at higher degree of confinement. Below we pay a special attention to the effect of confinement on the dynamics and the rheology.

In Fig. 4.11 we show the disturbed velocity profile for different values of the reduced volume. The vesicle with $\tau = 1$ disturbs much the applied external flow. For this case in the region between the wall and the vesicle membrane (near $x = 0$) an almost parabolic velocity profile is developed. This is due to the birth of a pressure gradient as it is shown in Fig.4.12, showing the pressure field for $\tau = 1$.

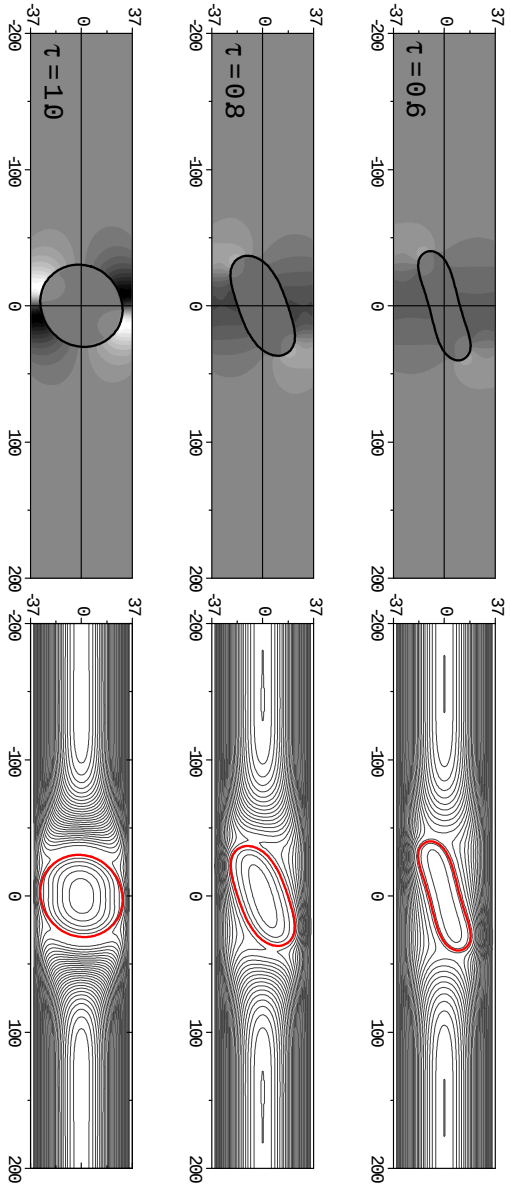

Fig. 4.12: Induced pressure field and streamlines for different values of the reduced volume

4.2.2 Effet of the degree of confinement

Fig.4.13 shows the variation of several physical quantities measured for a tank-treading vesicle when varying the degree of confinement of the channel. The steady inclination angle decrease when increasing R_0/W. We expect that by decreasing farther R_0/W, we reach the unbounded geometry limit. Here we explored the confinement values up to $R_0/W = 0.4$. For $R_0/W > 0.4$ we need to increase W and also L to avoid unphysical effects induced by the periodic boundary conditions. The decrease of the inclination angle when increasing the degree of confinement is observed for droplet too [68]. The membrane tank-treading velocity decreases when increasing R_0/W. At higher degrees of confinement, just a small layer of the external fluid is able to cross the narrow region between the membrane and the wall. For hard spheres a decrease of the rotation velocity when increasing the degree of confinement [69] is also observed.
The stress exerted on the channel walls, increases when increasing R_0/W. The deduced viscosity also increases when increasing R_0/W. In fact increasing R_0/W, induces an increase in the flow resistance and to dissipation.

Fig.4.14 shows the pressure field and the streamlines developped inside and outside a vesicle with reduced volume $\tau = 0.9$ for three degrees of confinement.

4.3 Conclusions

- A two-dimensional tank-treading of a vesicle in a confined geometry is simulated using the technique of lattice-Boltzmann,
- The immersed boundary method approach is used to couple vesicle dynamics and fluid flow computed by lattice-Boltzmann method,
- The steady inclination angle and the vesicle membrane tank-treading velocity decreases when increasing the degree of confinement (the ratio between the size of the vesicle and the height of the channel),
- Recirculations of the external fluid flow takes place in a confined channel,
- The effective viscosity, in the presence of the vesicle, increases when increasing the vesicle reduced volume (for a given value of the degree of confinement) or by increasing the degree of confinement (for a given value of the reduced volume).

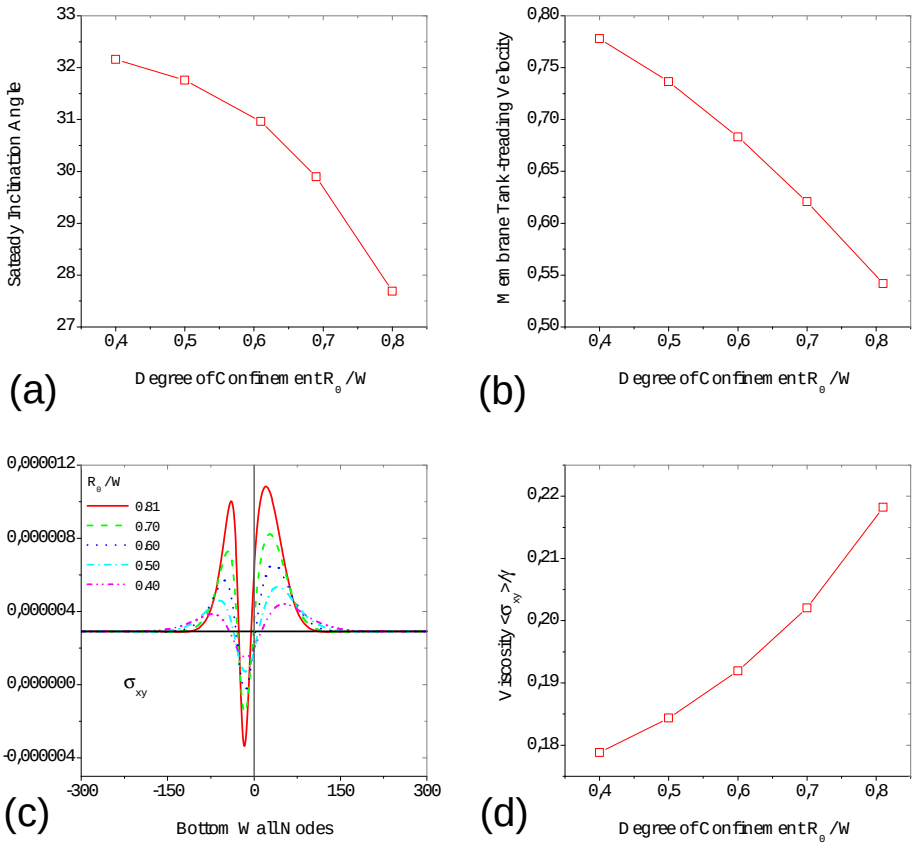

Fig. 4.13: Variation of the measured physical quantities associated to a vesicle performing tank-treading motion in confined geometries when varying the degree of confinement. (a) steady inclination angle, (b) the membrane tank-treading velocity, (c) the hydrodynamical stress field applied on the bottom wall and (d) the viscosity.

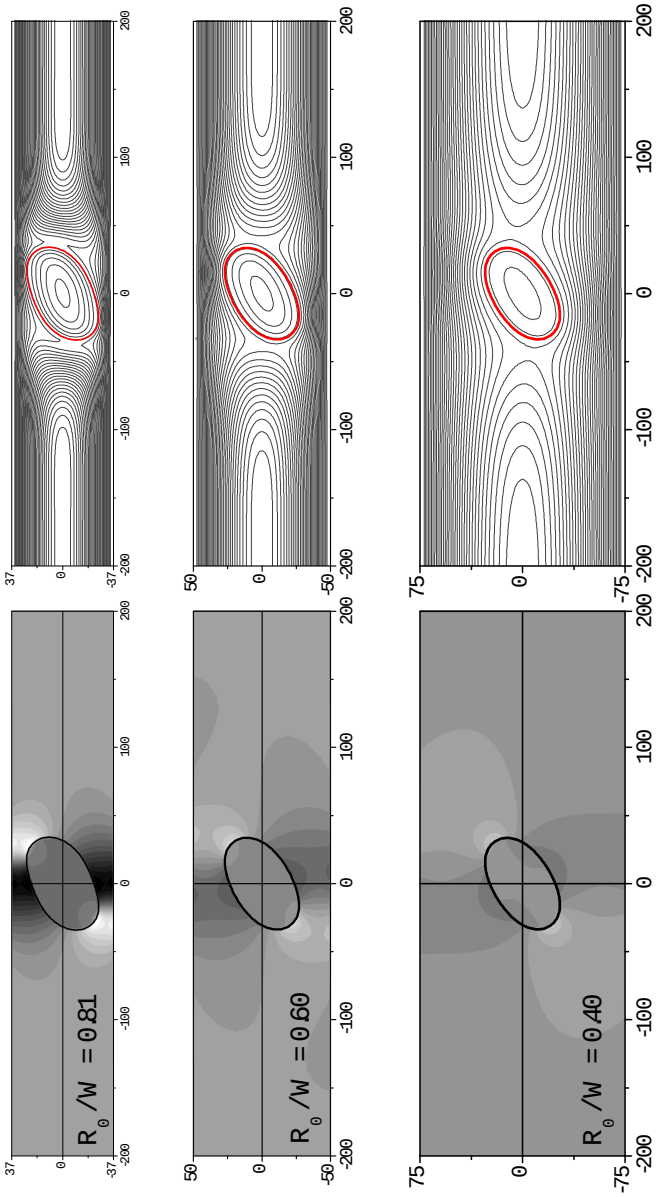

Fig. 4.14: Induced pressure field and streamlines for different values of the degree of confinement

5. VESICLE DYNAMICS UNDER POISEUILLE FLOW

In recent years there has been a great interest to design micro-fluidic devices with abilities to sort-out at the micro-scale particles such as living cells or vesicles based on their size, deformability or their enclosed fluid. One of the promising tricks is to exploit the properties of streamlines to guide particles. Micro-fluidic devices are mainly composed of straight channels where Poiseuille flow develops. Therefore it is interesting to understand how a vesicle reacts dynamically when it is subject to a such flow. Here we investigate numerically in two-dimensions the dynamical behavior and deformation of a single vesicle placed in a Poiseuille flow in the Stokes limit. This study is also motivated to understand how the macroscopic rheology of blood can be related to the deformation and migration of individual red blood cells, constituting it, under Poiseuille flow developing in capillaries and veinules. One of the interesting question in blood circulatory research concerns the Fahraeus-Lindqvist effect (decrease of the apparent blood viscosity in smaller vessels) [70]. We consider two cases: (1) the ambient fluid is unbounded (no bounding walls), in order to investigate only the effect of the Poiseuille flow (i.e. the flow curvature), or (2) bounded by a steady infinite solid wall, in order to investigate the interplay between the Poiseuille flow- and the wall-induced lift forces. To track the vesicle in such geometries we used the boundary integral method. Here we limited our study to vesicles without viscosity contrast between their internal and external fluids. Comparison and validation of a suggested similarity law, for the lateral migration velocity, with experimentally obtained data are also reported.

5.1 Poiseuille flow velocity profile

The applied plane Poiseuille flow $\mathbf{v}^{\infty}(\mathbf{r})$ in 2D has the following form

$$\begin{cases} v_{\mathrm{x}}^{\infty}(\mathbf{r}) = v_{\max}\left[1-\left(\frac{y}{w}\right)^2\right], \\ v_{\mathrm{y}}^{\infty}(\mathbf{r}) = 0, \end{cases} \tag{5.1}$$

where $v_{\max}$ is the maximum velocity at the centerline located at $y = 0$ and $2w$ is the distance from the centerline to the location where the velocity of

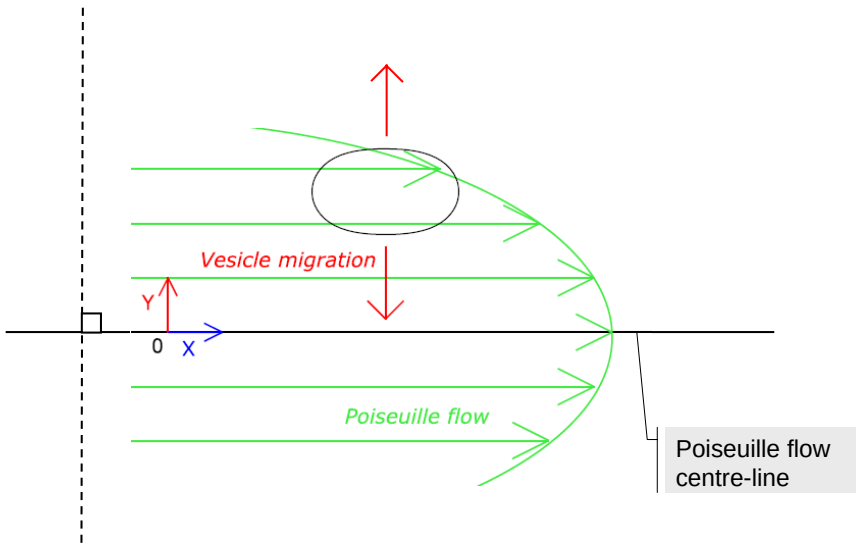

Fig. 5.1: Schematic showing a vesicle placed in unbounded Poiseuille flow

the flow vanishes. In all the simulations performed so far we take always the aspect ratio $R_0/w \ll 1$, with R_0 is the size of the vesicle, in order to keep $v_x^\infty(w) = v_x^\infty(-w) = 0$ practically unperturbed by the presence of the vesicle. Another important quantity characterizing the Poiseuille flow is its curvature c given by:

$$c = \partial^2 v_x^\infty / \partial^2 y = -2\frac{v_{\max}}{w^2}. \tag{5.2}$$

In the unbounded geometry this is the only parameter characterizing the flow, as discussed below. Moreover, the Poiseuille flow has non uniform shear rate, which depends on the position:

$$\gamma(\mathbf{r}) = \partial v_x^\infty / \partial y = -\left(2\frac{v_{\max}}{w^2}\right) y = cy. \tag{5.3}$$

5.2 Unbounded geometry

In this first part we focus our attention on describing the dynamics of a single vesicle placed in an unbounded plane Poiseuille flow (no bounding walls). In

such conditions we would like to suppress completely the effects of the walls (as discussed below) and to focus just on investigating the bulk effects of the Poiseuille flow on the vesicle dynamics. This situation corresponds in reality to a vesicle flowing in a channel (with a width which is large enough as compared to the vesicle size) at distances far away from the bounding walls. We consider the small Reynolds number limit (Re $<<$ 1), so that inertia can be neglected.

In an unbounded linear shear flow (of low Reynolds number) a vesicle does not exhibit any lateral migration with respect to the flow direction. The presence of a wall breaks the translational symmetry perpendicular to the flow direction and a vesicle is found to migrate away from the wall [18–21,53]. This is the so-called lift force caused by the flow induced upstream-downstream asymmetry of the vesicle [19]. More recently, it has been shown that even a spherical vesicle may execute a lift force as well, provided that the wall is flexible [13]. In that case, the wall deformability breaks the upstream-downstream symmetry.

A nonlinear shear flow (e.g. a Poiseuille flow) has a varying shear rate. It is therefore of certain importance to understand its possible contribution to a cross-streamline migration process. We consider neutrally buoyant vesicles so that gravity effect is suppressed. Fig. 5.1 shows the geometry of the studied problem.

As stated above dynamics is simulated by making use of the boundary integral method. Thus the velocity of each point belonging to the vesicle membrane is given by the integral equation:

$$v_j(\mathbf{r}) = \frac{1}{4\pi\eta} \oint_{\partial\Omega} G_{ji}(\mathbf{r}, \mathbf{r}') f_i(\mathbf{r}') ds(\mathbf{r}') + v_j^{\infty}(\mathbf{r}) \tag{5.4}$$

where $v_j^{\infty}(\mathbf{r})$ is substituted by Eq. (5.1) to implement the Poiseuille flow. G_{ji} is the two-dimensional free space Green's function and f_i is the force exerted by the membrane on its surrounding fluid. See chapter *Used resolution methods* for more details.

5.2.1 Lateral migration

Figure 5.2 shows the time evolution of the lateral position of a vesicle which has been released initially at five different vertical positions: $y_0 = 0$, ± 1, ± 2, ± 3 and ± 4. In most cases we have studied vesicles having a large enough reduced volume (small and moderate deviations from a circular shape) placed in a Poiseuille flow characterized by $v_{\max} = 800$ and $w = 10$. In all situations treated so far, vesicles migrate towards the centerline of the Poiseuille flow where no further lateral migration is observed. The position gives the

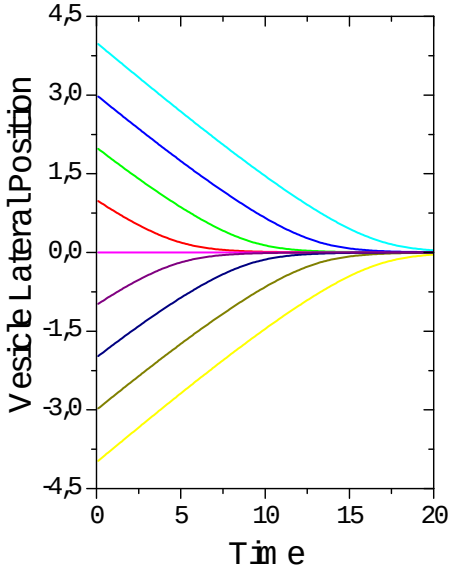

Fig. 5.2: The time evolution of the lateral position of a vesicle released initially at five different initial positions $y_0 = 0, \pm 1, \pm 2, \pm 3, \pm 4$.

distance from the centerline of the Poiseuille flow measured in units of the vesicle effective radius. All the curves are linear in a large range and deviations from this linear law occur only close to the center of the Poiseuille flow, in a range smaller than the vesicle size.
The curvature of the imposed velocity profile, together with the vesicle deformability, causes a systematic migration of a tank-treading vesicle perpendicularly to the parallel streamlines towards the flow center-line. Once it reaches this equilibrium lateral position, it stops tank-treading. It keeps moving just parallel to the flow direction.
Our results show that the lateral migration velocity increases with the curvature of the flow profile. This behavior (lateral migration towards the Poiseuille flow centerline) is different from a prediction made by L. G. Leal for droplets [71], according to which droplets should migrate away from the center of the Poiseuille flow towards the periphery. Actually, in Ref. [71] it is predicted that the direction of the lateral migration of a droplet depends on the viscosity contrast, between the internal and the external fluids. For values between 0.5 and 10 –and particularly in the absence of a viscosity contrast as treated here–, migration occurs towards the periphery, while for values smaller than 0.5 or greater than 10, it occurs towards the center line. We did not observe any of these scenarios neither from numerical studies,

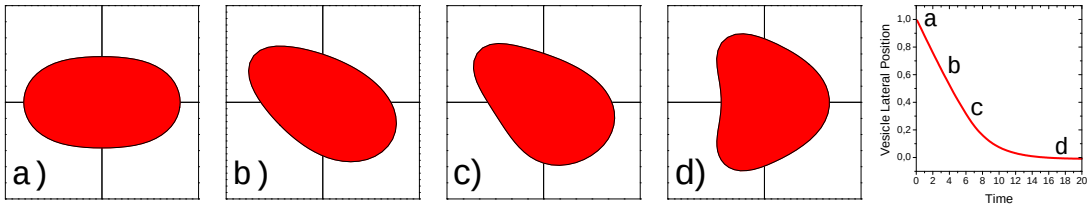

Fig. 5.3: The shape of the vesicle changes from an initially elliptical shape in part a) to the final axisymmetric parachute shape in d) when it migrates towards Poiseuille flow center-line, reduced area $\nu = 0.90$.

nor from analytical results [72].
As stated above, a drop (having no viscosity contrast with the ambient fluid) is predicted to drift towards the periphery [71]. Thus, vesicles and droplets behave quite differently. In chapter *Vesicle model and hydrodynamical equations* we have presented the main differences between vesicles and droplets, both from the physical and the mathematical point of view [1] . For vesicles, we have explored a large domain of parameter space and in all cases the vesicle migrate towards the center. This result is also confirmed by analytical calculations [72] in the quasi-spherical limit (following the spirit in Ref. [17]) in three spatial dimensions and experimentally [73]. This points to the fact that the migration direction does not depend on the dimensionality.

5.2.2 Vesicle shape deformation

During the migration, the vesicle shape undergoes deformations due to the hydrodynamic stresses imposed by the Poiseuille flow on the membrane. The vesicle is deformed and tilted until reaching a quasi-stationary orientation which is oblique with respect to the parallel streamlines. Figure 5.3 shows different vesicle shape deformations occurring in our simulations during the migration, from an initially elliptical shape at the initial position $y_0 = 1$ shown in Fig. 5.3(a), to a final parachute-like shape at the center of the Poiseuille flow as shown in Fig. 5.3(d). More or less similar parachute shapes are observed for capsules [75] and red blood cells [74, 76] as they have been observed also experimentally for vesicles in Ref. [29], but all these exam-

[1] A preliminary analytical calculation for drops actually show that the drop migrates always towards the centerline (G. Danker and C. Misbah (private communication)). The analytical result found by these authors is different from that of L. G. Leal.

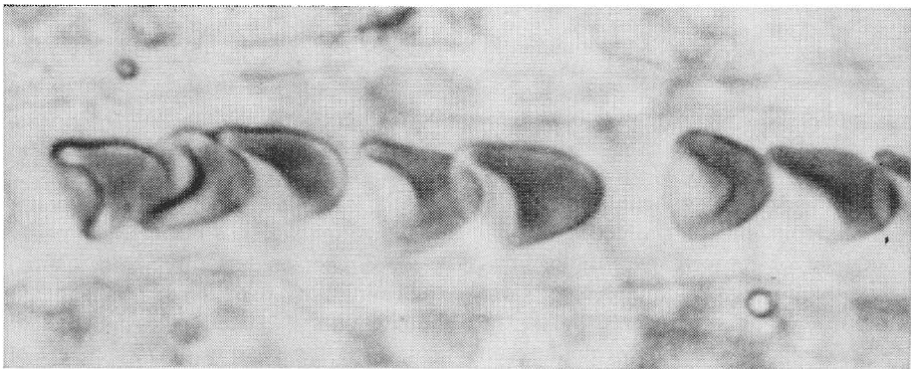

Fig. 5.4: Red blood cells flowing in vivo in a capillary showing parachute-like shape [74].

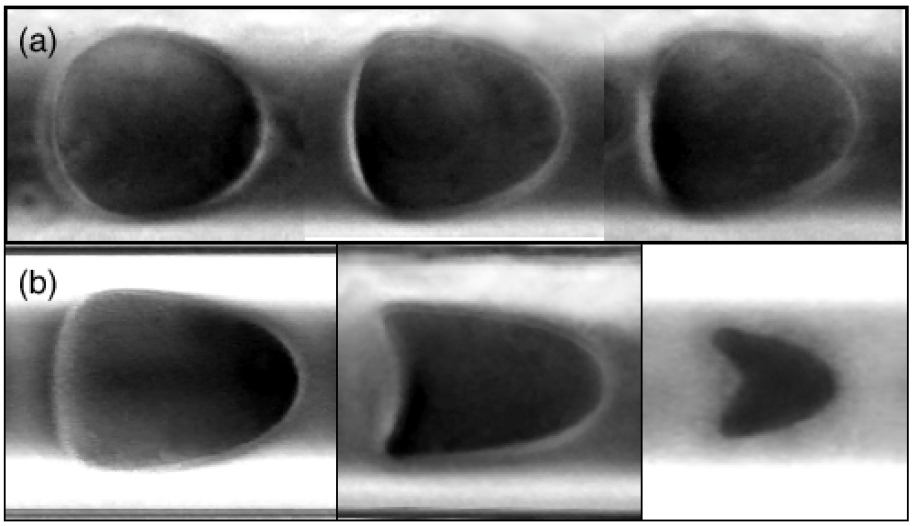

Fig. 5.5: Shapes of vesicles flowing in glass capillaries [29].

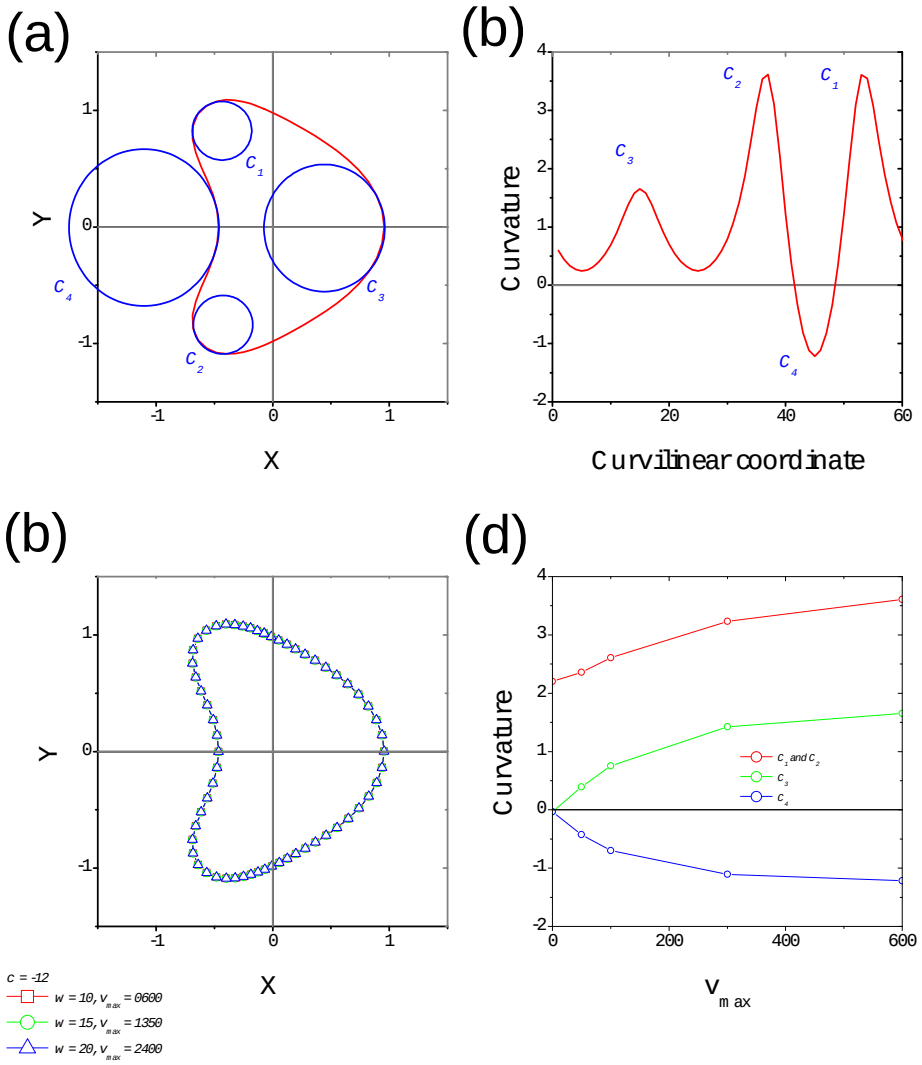

Fig. 5.6: The final steady parachute shape of a vesicle, with reduced volume $\tau = 0.90$, in different Poiseuille flows.

ples, unlike the present study, concern capillary flows. Before the vesicle reaches the center of the Poiseuille flow, it acquires an asymmetric shape as depicted in Fig. 5.3(b) and in Fig. 5.3(c). This asymmetry, which is caused by the non-uniform shear rate across the vesicle, is crucial for cross-stream line migration of vesicles in a plane Poiseuille flow. For the axisymmetric final steady prachute-like shape, it depends only on the values of the vesicle reduced volume and on the curvature of the imposed Poiseuille flow, as shown in Fig. 5.4b. Variation of geometrical quantities characterizing the parachute-like shape with the curvature is given in Fig. 5.4d.

5.2.3 Migration velocity

The lateral migration velocity depends on various parameters. Of particular importance are the curvature of the velocity profile of the Poiseuille flow and the local capillary number, defined as:

$$Ca(\mathbf{r}) = \frac{\eta R_0^3}{\kappa}\gamma(\mathbf{r}) \tag{5.5}$$

as discussed in the following. There should be, in the absence of a wall, no lateral migration in a linear shear flow. In the presence of a flow having a nonlinear shear gradient, migration becomes possible. Migration becomes significant if the flow curvature varies on the scale of the vesicle size. Therefore, curvature of the Poiseuille flow profile plays an essential role, but more precisely, the magnitude of the local capillary number, which determines essentially the vesicle deformation (which loses the up-down symmetry due to the shear gradient), is the most relevant quantity. The dependence of the migration velocity on the local capillary is shown in Fig. 5.7 for different values of $v_{\max}$, w and c, after the decay of an initial transient. In Fig. 5.7(a) and in Fig. 5.7(b) we kept the value of $v_{\max}$ fixed and we investigated the vesicle migration by varying the value of w. For smaller values of w, which corresponds to larger values of the curvature c, the vesicle migrates faster towards the center of the Poiseuille flow. Fig. 5.7(b) shows the data collapse by plotting the migration velocity normalized with the curvature versus the local capillary number. In Fig. 5.7(c) and in Fig. 5.7(d) we kept w fixed and we examined the effect of varying the value of $v_{\max}$ for each value of w. The vesicle migrates faster with increasing values of $v_{\max}$ for every fixed w, because the curvature c increases with $v_{\max}$. Data collapse is again obtained in Fig. 5.7(d) by plotting the normalized migration velocity versus the local capillary number. The data collapse is more pronounced for smaller values of the curvature. In Fig. 5.7(e) and Fig. 5.7(f) we have varied $v_{\max}$ and w in such a way to keep the curvature fixed. We find that the vesicle migrates in this case to the Poiseuille flow center-line for the three parameters

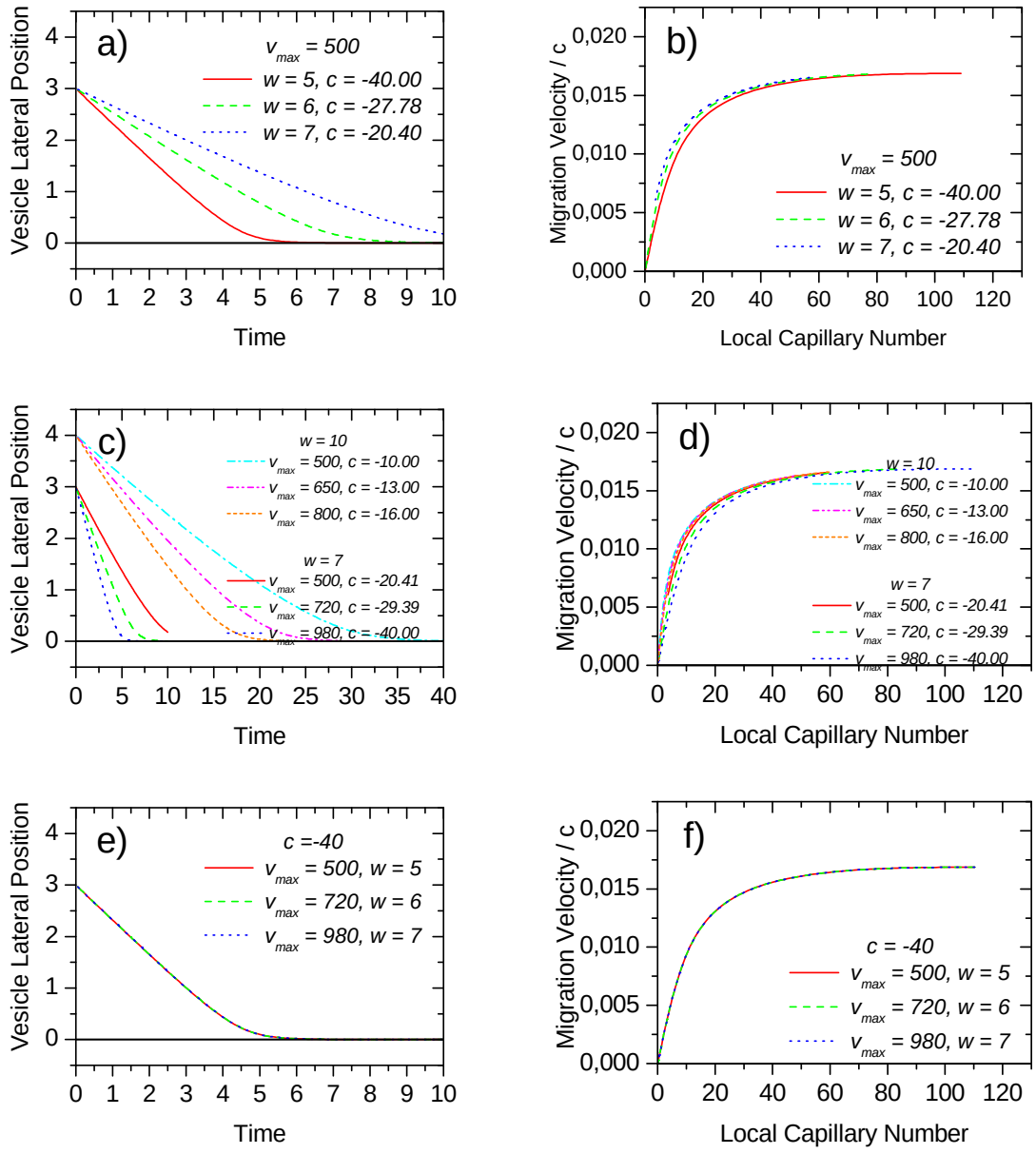

Fig. 5.7: Time evolution of the vesicle position in an unbounded Poiseuille flow and its corresponding normalized migration velocity versus the local capillary number for different values of $v_{\max}$, w and c (see text). The data correspond to situation where initial transients have decayed.

combinations exactly (i.e. quantitatively the same results) in the same manner, which emphasizes again the important role of the nonlinear shear field. From the above study, we can conclude that the migration velocity in an unbounded Poiseuille flow divided by the curvature c should be described by the following universal scaling law:

$$\frac{v_{\mathrm{m}}(y)}{c} \sim f\left[Ca(y)\right] . \tag{5.6}$$

The extraction of this law is based on results of Figs. 5.7b, 5.7d, and 5.7f. The function f is universal and depends only on Ca. The analytical form of the universal function is not at present.
If the initial vesicle shape is not quasi-circular but elliptical, we find a similar behavior as depicted in Fig. 5.7. The deformability of the vesicle, which depends on the bending rigidity κ, is a further ingredient for migration. By increasing the bending rigidity κ the local capillary number $Ca \propto \kappa^{-1}$ decreases and so does the migration velocity. This leads also to the conclusion that a rigid particle, corresponding to very large values of κ, will not exhibit a lateral migration in parabolic shear flow in the Stokes limit. It has been shown earlier that rigid spheres migrate only due to the contribution of $(v \cdot \nabla)v$ in the Navier-Stokes equation [77], which is beyond the Stokes limit. Similar trends as for a vesicle are obtained for deformable bead-spring models [78], where the migration velocity decreases with increasing rigidity of the tumbling object, corresponding also to increasing values of the spring constant. Indeed the vesicle deformability is, in addition to the nonlinear shear gradient, the main ingredient for the lateral migration in the Stokes limit. A vesicle in unbounded Poiseuille flow undergoes large deformations ($C_a \gg 1$, see Fig. 5.7) caused mainly by the curvature of the velocity profile.

5.3 Semi-bounded geometry

In this section we study the dynamics of a vesicle placed in a semi-bounded Poiseuille flow, it consists in placing a solid infinite plane wall at one of the locations where the Poiseuille flow velocity vanishes. The only difference with the above unbounded geometry situation is the appearance of an additional lift force caused by the presence of the bounding wall [19–21]. In our simulations we considered just one wall in order to be able to investigate the interplay between the Poiseuille curvature- and the wall-induced lift force. It should be noted also that there exists an explicit Green's function for a semi-infinite domain (see chapter *Used resolution methods*), and this is another motivation for considering one wall only. In the limit where the distance from the wall to the Poiseuille centerline is large enough (compared to

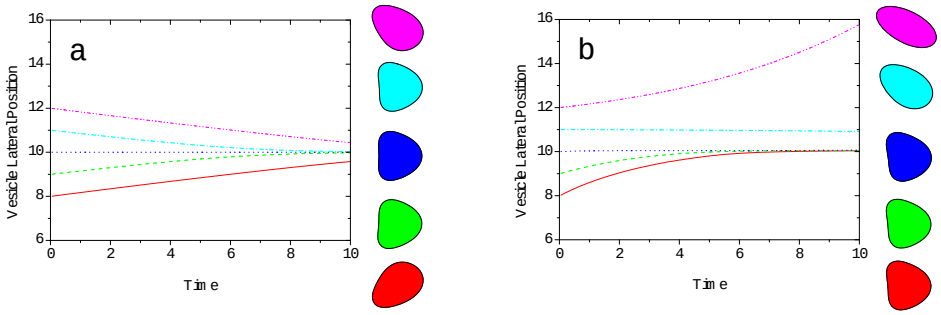

Fig. 5.8: Evolution in time of the vesicle lateral position in Poiseuille flow for five different initial lateral positions. (a) in unbounded fluid, (b) in a semi-infinite fluid bounded by a plane wall located at $y = 0$. In the both cases $v_{\max} = 600$, $w = 10$ and the vesicle has a reduced volume of $\tau = 0.95$. The Poiseuille flow centerline is located at $y = 10$. The vesicle shapes shown in the right side of every plot are the one taken at time 10 and their color correspond to the curve with same color.

the size of the vesicle; typically we have considered $R_0/w > 8$), the obtained simulations results agrees quite well with experiment in channel [73]. We have compared our results to the experimental data [73]. A similarity law giving the lateral migration velocity of a vesicle flowing in a micro-channel as a function of the geometry and vesicle parameters is derived.

5.3.1 Simulations results

Vesicles with the same size ($R_0 = 1$) and the same reduced volume ($\tau = 0.95$) are initially placed at five different lateral positions, one of them being intentionally placed at the flow center-line ($y = 10$). The imposed flow is characterized by $v_{\max}$ and w:

$$v_x = v_{\max}\left(2\left(\frac{y}{w}\right) - \left(\frac{y}{w}\right)^2\right) \qquad \text{with} \qquad 0 < y < 2w. \tag{5.7}$$

We have studied the effect of presence of a wall. For that purpose, we have considered two situations (i) the suspending fluid is unbounded, (ii) the suspending fluid is bounded by an infinite plane wall located at $y = 0$. For the unbounded case Fig. 5.8a, we find that vesicles migrate laterally towards the flow center-line as was reported in Ref. citeKaoui2008 and also in the previous section *Unbounded geometry*. The center-line correspond here to

the equilibrium lateral position; there the vesicle moves parallel to the flow direction with an axisymmetric shape (the blue colored shape in Fig. 5.8a). The final equilibrium lateral position location does not depend on the initial position of the vesicle, in this case. Moreover, the problem is symmetric with respect to the location of the flow center-line: a vesicle placed above or below this axis moves and deform in the same fashion (see the trajectories and their corresponding shapes in Fig. 5.8a). By placing a steady infinite plane wall at the position $y = 0$ (where the Poiseuille flow velocity vanishes), the evolution in time of the vesicle lateral position is affected (see Fig. 5.8b). In this case, the dynamics of the vesicle is sensitive to the initial lateral position as it is depicted in Fig. 5.8b. Vesicles initially placed below the center-line ($0 < y(t = 0) < w$) migrate laterally until reaching an equilibrium lateral position (with a slight shift above the center-line, which becomes negligible for $w > 8$). Here the vesicle reaches this position faster compared to the unbounded case (see for example the vesicle presented with the red line in the two Figs. 5.8a and 5.8b), due to the presence of an additional lift force, due to the presence of the wall. An interesting feature is that the vesicle, despite the fact that it is asymmetric (up down asymmetry) it ceases to drift laterally. (the blue colored shape in Fig. 5.8b). This seems to indicate that migration forces due to the curvature dominate over wall effects near the center-line.

In order to discuss the relative influence of the wall and of the curvature of the velocity profile, it is convenient to take advantage of the domain where no bounding wall exists in the simulations: vesicles initially placed above the center-line ($w < y(t = 0) < 2w$) move with negative inclination angles (the magenta and the cyan colored shapes in 5.8b) because of the shape of the Poiseuille velocity profile in this region. The vesicle presented by the cyan colored line moves very slowly towards the centerline while the one presented with the magenta colored line travels outward the center-line. It is noteworthy that in this region the two lift forces are in competition and have opposite signs: the curvature induced lift force tries to attract the vesicle toward the centerline, while the wall induced lift force even at such distance still pushes the vesicle far from the wall (due to the two-dimensionality of the space). However, their relative amplitude depends on the distance of the vesicle to the center-line. Close to the center-line, the shear rate tends to vanish and the wall induced lift force becomes weaker; this explains the inward migration of the cyan colored vesicle. Far from the center-line, the shear rates become greater which explains the outward migration of the magenta colored vesicle. More, when this vesicle travels away its shape undergoes larger deformations because it finds itself in regions with higher shear rates. Hereafter, we continue talking just about simulations performed for vesicles placed initially and

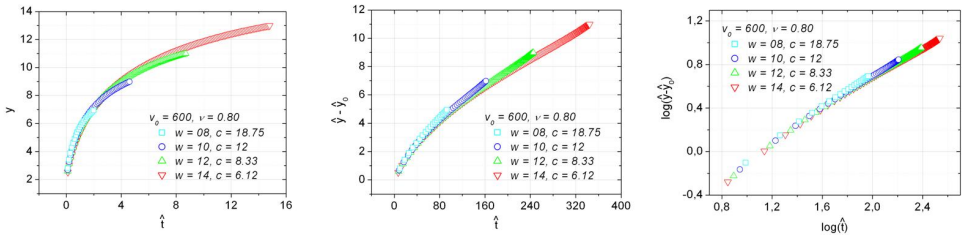

Fig. 5.9: (a) Evolution in time of the lateral position $y(t)$ of a vesicle with $\tau = 0.8$ in different Poiseuille flows, (b) with scaled space and time variables and (c) a log-log plot.

moving in the region between the wall and the flow centerline ($0 < y(t) < w$).

5.3.2 Similarity law

Figure 5.9a shows the evolution in time of a vesicle released initially near the wall ($y = 2$) and moving towards the Poiseuille center-line for different values of w. In this figure only the data of vesicles reaching an almost R_0 before the Poiseuille centreline (but not beyond) are presented. We did so since we are interested in extracting a law giving the lateral migration of a vesicle moving between the wall and the Poiseuille center-line location, in order to compare with experiments in a channel where it is observed that the vesicle does not cross the centreline. For a given value of the vesicle reduced volume (here $\tau = 0.8$) $y(t)$ depends a priori on the three parameters $(R_0, w, v_{\max})$. In order to determine the functional dependence of the migration velocity, space and time are rescaled. We take vesicle size R_0 as a spatial scale. The dimensionless spatial coordinate is thus written as:

$$\hat{y} = \frac{y}{R_0}, \tag{5.8}$$

for the vesicle lateral position and

$$\hat{w} = \frac{w}{R_0} \tag{5.9}$$

for the half-width of the Poiseuille flow.
However, the choice of a relevant time (or velocity) scale is less obvious. Indeed, while the inverse of the shear rate yields a natural scale in the case of simple shear flow, here this is not an adequate choice since the shear rate is not uniform in space and it varies along the vesicle trajectory. The trick is to rescale each infinitesimal time step dt around the time t by the local shear rate:

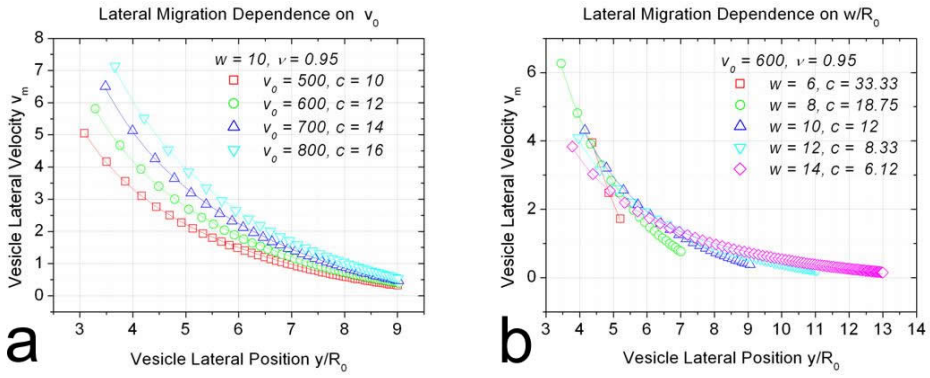

Fig. 5.10: The vesicle lateral velocity versus its lateral position for different values of $vmax$ (a) and w (b). Simulations data are represented by scatters while the colored solid curves are fits with the law Eq. (5.13).

$$\gamma(y) = \frac{\partial v_x^{\infty}}{\partial y} = c(w - y), \tag{5.10}$$

of the unperturbed flow at the position $y(t)$. Note that this amounts to saying that the migration velocity is controlled by the local flow, which is a reasonable assumption in a Stokes flow. The new dimensionless time-like variable is obtained by integrating the rescaled time steps:

$$\hat{t} = \int_0^t \gamma(y(\tau'))d\tau' = c\int_0^t [w - y(\tau')]\, d\tau', \tag{5.11}$$

$\hat{t}$ accounts for the history of the shear rates experienced by the vesicle along its trajectory. Interestingly, as shown in Fig. 5.9b, all the curves $\hat{y}(\hat{t}) - \hat{y}_0$ (with $\hat{y}_0$ is the intial lateral position) exhibit a quite reasonable collapse, whatever the value of w is. A log-log plot of $\hat{y}(\hat{t}) - \hat{y}_0$ is linear, a clear signature of a power law behavior of the forme:

$$\hat{y}(\hat{t}) - \hat{y}_0 = \beta \hat{t}^{\alpha}, \tag{5.12}$$

where the dimensionless parameters α and β, that are independent form R_0, w and $v_{\max}$, are obtained from the data fit. The lateral migration velocity v_m as a function of the position y and the triplet (R_0,w,$v_{\max}$) is then easily extracted:

$$v_m = \xi c R_0^2 \frac{\hat{w} - \hat{y}}{(\hat{y} - \hat{y}_0)^{\delta}} = \xi \frac{R_0 \gamma(y)}{(\hat{y} - \hat{y}_0)^{\delta}}, \tag{5.13}$$

with $\xi \equiv \alpha\beta^{1/\alpha}$ and $\delta \equiv 1/\alpha - 1$. Figures 5.10a and 5.10b presents fits of simulations data by the above law Eq. (5.13). The simulations data are well fitted by the law given Eq. (5.13) with $\delta \simeq 0.8$ and $\xi = 0.1$.

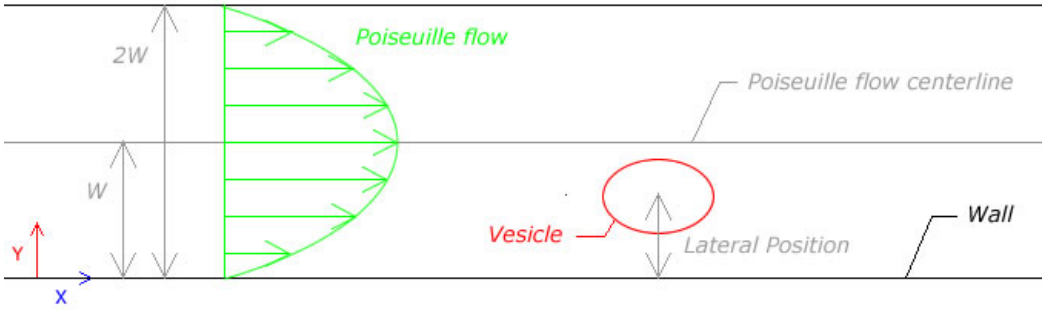

Fig. 5.11: A schematic showing the geometry of the problem of a vesicle placed in a micro-channel.

5.3.3 Comparison with experimental results

Here the similarity law obtained above (Eq. 5.13) for the lateral migration velocity is used to fit data obtained experimentally [73]. The micro-channel is straight and has a rectangular cross section (see the schematic presentation in Fig. 5.11). The flow direction is Ox and the lateral migration is along Oy, this means that migration is studied for a given position z. Let $2w$ denote the channel width in th y-direction with $R_0/W << 1$ and v_{max} the imposed flow velocity at the center of the channel in the absence of the vesicle. The two walls are located at $y = 0$ and $y = 2w$. The vesicle is characterized by two geometrical parameters: 1 - Its effective radius R_0, determined from its volume V by $R_0 = (3V/4\pi)^{1/3}$ and 2 - its reduced volume $\tau = V/\left(4\pi\left(S/4\pi\right)^{3/2}/3\right)$ characterizing vesicle deflation, with S being the surface of the vesicle.

Experimental set-up

The micro-fluidic device is composed of straight channels of height $h_0 = 66.6\mu m$ (in the direction of gravity z) and width $2w$ (rectangular cross section). The walls of the channels are made of the PDMS glued to a glass cover slide. The flow is induced by applying a pressure difference between the inlet and the outlet which are linked to reservoirs placed at different heights. Vesicles are prepared following the electroformation method [79]. They are made of a DOPC lipid bilayer enclosing an internal solution of sugar (sucrose or glucose) in water or in a 1:4 glycerol-water (w:w) mixture. Samples are diluted in a slightly hyperosmotic outer solution of the same type, in order to deflate them by osmosis. Dextran can be added to one of the solutions to modify the viscosity ratio λ.

Fig. 5.12: Experimental snapshots (taken at different times) showing the displacement of a single vesicle in a micro-channel

A particular design of the upstream channel creates an initial condition where incoming vesicles touch the $y = 0$ wall in the observation area and start to be lifted away from it. In particular, they have already developed a nearly ellipsoidal shape tilted with respect to the wall [19–21]. Moreover, the flow has been established for a long time, resulting in centering in the z-direction. In that case, the 2D fluid velocity profile in the xy-plane where the vesicle lies is nearly paraboloic, provided the rectangular cross section of the 3D channel obeys $2w/h_0 \leq 3$ [80].Therefore, as a first approximation, the vesicle is in a 2D plane Poiseuille flow, with reproducible initial condition $y(t = 0) = y_0$, where y_0 is the position of the vesicle center of mass just before the lift-off, which is close to R_0. as the vesicle is centered in the z-direction, the imposed profile is thus written as $v_x^{\infty}(\mathbf{r}) = c\,(yw - y^2/2)$ where $c = 2v_{max}/w^2$ is the curvature of the parabolic velocity profile. The vesicle is tracked along its trajectory with a phase-contrast microscope, and the position y of its center of mass is determined by image processing.

Experimental results

The same type of dynamical behavior of a vesicle regarding migration towards the Poiseuille centerline is observed also experimentally. Figure 5.12 shows snapshots of a vesicle while it is moving towards the center of the microchannel. Figure 5.13 shows the evolution in time of the lateral position of a vesicle for different set of parameters and the main steps as performed above to reach the power law:

$$\hat{y}(\hat{t}) - \hat{y}_0 = \beta \hat{t}^{\alpha}. \tag{5.14}$$

For the experimental data we found:

$$\xi \equiv \alpha\beta^{1/\alpha} = 1.3 \times 10^{-2} \pm 0.3 \times 10^{-2}, \tag{5.15}$$

and

$$\delta \equiv \frac{1}{\alpha} - 1 = 0.8 \pm 0.2. \tag{5.16}$$

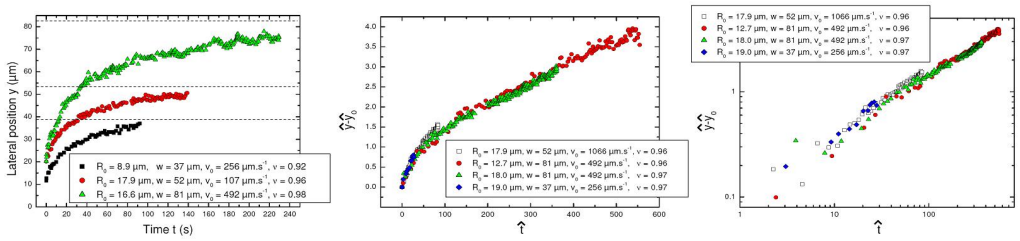

Fig. 5.13: (a) Evolution in time of the lateral position of a vesicle flowing in a microchannel for different values of the problem parameters, (b) with scaled space and time variables and (c) the log-log plot

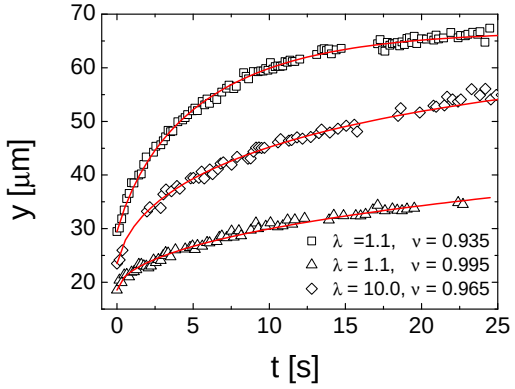

Fig. 5.14: Experimental data and fits with equation $\hat{y}(\hat{t}) - \hat{y}_0 = \beta \hat{t}^{\alpha}$

The errors bars for these cofficients can be linked with errors bars on y and w due to local defects on the PDMS walls, ans also (and mainly) with uncertainties on the measure of τ (the reduced volume), which requires a very precise determination of the mambrane position. For the experimental data, working directly with the velocity v_m instead of the position $y(t)$ is more problematic due to the noise caused by a discrete time derivation of the position, which is known with limited precision. For this reason we treat directly the data $y(t)$. Figure 5.14 reveal that the experimental data are well fitted with the proposed similarity law.
The agreement between experiments and simulations regarding the exponent δ is quite satisfactory. However, numerical studies overestimate the amplitude ξ. This is attributed to the 2D character (actually a translationally invariant form in the z-direction), causing an enhancement of the lift force due to a wider contact between the drifting entity (vesicle) and the ambient fluid.

Conclusions

- A single vesicle placed in an unbounded plane Poiseuille flow has been investigated numerically. We found that the vesicle migrates during its tank-treading motion towards the Poiseuille flow centerline.
- When the vesicle reaches this final equilibrium position, its tank-treading and lateral migration velocities vanish and it continues to move with an axisymmetric parachute-like shape parallel to the flow direction.
- The migration velocity is found to increase with the local capillary number, but reaches a plateau above a certain value of the capillary number. This plateau value increases with increasing the curvature of the parabolic flow profile c. We found that the migration velocity normalized with the curvature $v_{\text{migration}}/c$ follows essentially a universal law where the universal function depends on the local capillary number C_a, namely $v_{\text{migration}}/c \sim f(C_a)$.
- In the wall-bounded geometry, there is an additional lift force caused by the wall.
- We find that the closer the vesicle is to the centerline, the more the curvature induced lift force is dominant.
- Far from the center-line, the migration is mainly governed by the wall-induced lift force. Curvature-driven lift dominates when the distance is few times the vesicle size. However, both effects always coexist and couple in a non linear way, giving rise to a migration law which could not be directly inferred from already known laws of more simple cases (unbounded Poiseuille flow [81] or wall-bounded shear flow [19–21]).
- A similarity law for the lateral migration velocity of a vesicle in a bounded Poiseuille flow as a function of its distance to the walls and to the center-line, its effective radius, the channel's width and the flow velocity is suggested.
- Comparison with, and validation of this law by, experimental results has been undertaken and have revealed good agreement.

6. CONCLUSIONS

Along the present thesis we studied analytically and numerically the dynamical behavior and the deformation of a single vesicle under simple shear and Poiseuille flows. Two situations are considered for each type of the flow, the suspending fluid is unbounded (infinite fluid) or confined by bounding walls.

For the unbounded shear flow, the small deformation theory is used to derive two analytical dynamical equations governing the orientation and the deformation of a vesicle subject to simple unbounded shear flow. The phase-diagram giving the known vesicle dynamical regimes (tank-treading, tumbling and vacillating-breathing), under shear flow, as a function of the viscosity contrast (between the enclosed and the suspending fluids) and the capillary number (ratio between the flow time scale - inverse of shear rate - and that needed for the vesicle to relax to its equilibrium shape) is drawn. Effect of varying the excess area on bifurcation boundaries, in the phase-diagram, is investigated and good agreement is obtained with results reported in Ref. [60]. Importance of the vesicle excess area as an independent parameter controlling the dynamics (beside the viscosity contrast and the capillary number), under shear flow, is confirmed by a systematic analysis. Impact of varying one of the controlling parameters (while fixing the two others) on the evolution of various quantities characterizing each vesicle dynamical regime is reported. The behavior of the vacillating-breathing mode is emphasized since there is lack of quantitative measurements concerning this mode in literature.

For confined shear flow, the lattice-Boltzmann method is used. In the present thesis, we presented how we adapted the lattice-Boltzmann method to simulate dynamics of vesicles. The internal and the external fluids flow are computed using the lattice-Boltzmann approach on a fixed Eulerian regular mesh. While the vesicle membrane is presented by a moving Lagrangian mesh immersed in the previous fluid mesh. On the one hand the vesicle membrane finds itself advected by its surrounding fluid flow and on the other hand it exerts a reaction force in response to the applied hydrodynamical stresses and therefore it causes disturbance and modification on its nearby fluid flow. As benchmarkings, the known vesicle equilibrium shapes in a fluid at rest are recovered and the known dynamical behavior of a vesicle under

simple shear flow - tank-treading - is also captured. The next step was to focus on investigating the effect of the confinement on the vesicle dynamics. In particular, we analyzed the vesicle's steady inclination angle, membrane tank-treading velocity and the rheology. Significant dependencies on the degree of confinement (the size of the vesicle divided by the half-width of the channel) is revealed.

The boundary integral method is appropriate for simulation of dynamics of a vesicle suspended in infinite or semi-infinite fluids. It has thus been used to investigate lateral migration under Poiseuille flow. In the unbounded geometry case, we find that the nonlinear character of the Poiseuille flow (non spatially uniform shear rate) causes the lateral migration of the vesicles towards the flow centerline, which is in a marked contrast with the migration of droplets, on which it has been reported theoretically that they migrate outward the centerline in the absence of a viscosity contrast. Once the vesicles reach the centerline, their lateral migration and tank-treading velocities vanish. They then only move parallel to the flow direction with a steady parachute-like shape. We find that the lateral migration velocity normalized by the curvature of the Poiseuille flow velocity profile is a universal function of the local capillary number.

In the wall-bounded geometry, an additional lift force caused by the presence of the wall appears. Here we considered one wall in order to be able to investigate the interplay between the wall- and the Poiseuille flow curvature-induced lift forces. We find that the closer the vesicle is to the centerline, the more the curvature induced lift force is dominant over the wall induced one. The opposite situation prevails when the vesicle is far from the centreline. In such a geometry, even in the absence of an opposite bounding wall, for certain initial positions the vesicle migrate laterally to reach an equilibrium lateral position which is shifted slightly above the centerline. We find that this shift could be decreased by increasing the gap between the centerline and the wall. In this limit a law for the lateral migration velocity (as a function of relevant structural and flow parameters) is proposed and is compared and validated by experimental results. This similarity law markedly differs from its analogue in unbounded geometry.

APPENDIX

A. DERIVATION OF THE MEMBRANE FORCE

In a two spatial dimension the vesicle membrane is represented by a one-dimensional closed contour. The corresponding membrane energy is an integral over this contour,

$$E = \frac{\kappa}{2}\int_0^L H^2(\mathbf{r})ds(\mathbf{r}) + \int_0^L \zeta(\mathbf{r})ds(\mathbf{r}), \tag{A.1}$$

where L is the vesicle perimeter (i.e. the length of the contour) and $\mathbf{r}$ the membrane vector position. Let,

$$E_C = \frac{\kappa}{2}\int_0^L H^2(\mathbf{r})ds(\mathbf{r}), \tag{A.2}$$

and,

$$E_T = \int_0^L \zeta(\mathbf{r})ds(\mathbf{r}), \tag{A.3}$$

The counterclockwise tangent unit vector (see Fig. A.1) is given by,

$$\mathbf{t} = \frac{\partial \mathbf{r}}{\partial s}, \tag{A.4}$$

and its derivative with respect to s defines the curvature,

$$\frac{\partial \mathbf{t}}{\partial s} = -H\mathbf{n}, \tag{A.5}$$

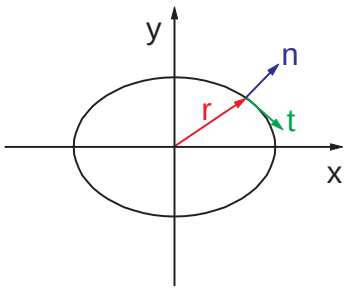

Fig. A.1: (Color) A schematic showing the vector position $\mathbf{r}$, the normal $\mathbf{n}$ and the tangent $\mathbf{t}$ unit vectors.

where $\mathbf{n}$ is the outward unit vector normal to the curve. The derivative of $\mathbf{n}$ with respect to s gives,

$$\frac{\partial \mathbf{n}}{\partial s} = H\mathbf{t}. \tag{A.6}$$

Using Eq. (A.4) and Eq. (A.5) we get the expression of the curvature,

$$H^2 = \left(\frac{\partial^2 \mathbf{r}}{\partial s^2}\right)^2. \tag{A.7}$$

The membrane force is deduced from the functional derivative of the energy $\delta E/\delta \mathbf{r}$, where $\delta \mathbf{r}$ is a local small displacement of the vesicle membrane. Due to the displacement of $\mathbf{r}$ by $\delta \mathbf{r}$, ds will undergo variations as well. It is convenient to introduce a fixed parametrization (instead of s) of the curve, which is denoted by α. α is a parameter that we can take to vary from 0 to 1. The correspondence with s is such that $s(\alpha = 0) = 0$ and $s(\alpha = 1) = L$. We then introduce the metric $g \equiv |\partial \mathbf{r}/\partial \alpha|^2$, so that $ds = \sqrt{g} d\alpha$. We convert the various terms in the energy by using now the variable α. The curvature assumes the following expression

$$H^2 = \left(\frac{\partial^2 \mathbf{r}}{\partial \alpha^2}\left(\frac{d\alpha}{ds}\right)^2 + \frac{\partial \mathbf{r}}{\partial \alpha}\frac{d^2 a}{ds^2}\right)^2, \tag{A.8}$$

$$= \frac{1}{g^2}\left(\frac{\partial^2 \mathbf{r}}{\partial \alpha^2} - \frac{\partial^2 s}{\partial \alpha^2}\mathbf{t}\right)^2. \tag{A.9}$$

Writing $\partial^2 \mathbf{r}/\partial \alpha^2$ in terms of the tangent and the normal vectors, it is straightforward to show that,

$$\frac{\partial^2 \mathbf{r}}{\partial \alpha^2} = \frac{d^2 s}{d\alpha^2}\mathbf{t} - gH\mathbf{n}, \tag{A.10}$$

This allows to eliminate s from the expression for H:

$$H^2 = \frac{1}{g^2}\left(\left(\frac{\partial^2 \mathbf{r}}{\partial \alpha^2}\right)^2 - \frac{1}{g}\left(\frac{\partial^2 \mathbf{r}}{\partial \alpha^2}\frac{\partial \mathbf{r}}{\partial \alpha}\right)^2\right). \tag{A.11}$$

The curvature force

Replacing in Eq. (A.2 H^2 by the expression given in Eq. (A.11) we obtain,

$$E_C = \frac{\kappa}{2}\int_0^1 \left(\ddot{\mathbf{r}}^2 - \frac{1}{g}\left(\ddot{\mathbf{r}}.\dot{\mathbf{r}}\right)^2\right) g^{-3/2} d\alpha\,. \tag{A.12}$$

The functional derivative of E_C reads (from classical variation results)

$$\frac{\delta E_C}{\delta \mathbf{r}} = \frac{\partial e_C}{\partial \mathbf{r}} - \frac{\partial}{\partial \alpha}\frac{\partial e_C}{\partial \dot{\mathbf{r}}} + \frac{\partial^2}{\partial \alpha^2}\frac{\partial e_C}{\partial \ddot{\mathbf{r}}}, \tag{A.13}$$

whith $e_C = (\kappa/2)\left(\ddot{\mathbf{r}}^2 - \frac{1}{g}\left(\ddot{\mathbf{r}}\dot{\mathbf{r}}\right)^2\right) g^{-3/2}$, $\dot{\mathbf{r}} = \partial \mathbf{r}/\partial\alpha$ and $\ddot{\mathbf{r}} = \partial^2\mathbf{r}/\partial\alpha^2$. Since e_C does not explicitly depend on $\mathbf{r}$, the first term on the right hand side of Eq. (A.13) vanishes. The second term gives,

$$\begin{aligned}
\frac{\partial}{\partial \alpha}\frac{\partial e_C}{\partial \dot{\mathbf{r}}} &= \kappa \frac{\partial}{\partial \alpha}\left(-\frac{1}{g^{5/2}}\left((\ddot{\mathbf{r}}\dot{\mathbf{r}})\ddot{\mathbf{r}} + \frac{3}{2}(\ddot{\mathbf{r}})^2\dot{\mathbf{r}} - \frac{5}{2g}(\ddot{\mathbf{r}}\dot{\mathbf{r}})^2\dot{\mathbf{r}}\right)\right), &\text{(A.14)}\\
&= -\kappa \frac{\partial}{\partial \alpha}\left(-\frac{\partial^2 s}{\partial \alpha^2}\frac{H}{g}\mathbf{n} + \frac{3}{2}H^2\mathbf{t}\right) &\text{(A.15)}
\end{aligned}$$

while the third one becomes,

$$\begin{aligned}
\frac{\partial^2}{\partial \alpha^2}\frac{\partial e_C}{\partial \ddot{\mathbf{r}}} &= \kappa \frac{\partial^2}{\partial \alpha^2}\left(\frac{1}{g^{3/2}}\ddot{\mathbf{r}} - \frac{1}{g^{5/2}}(\ddot{\mathbf{r}}\dot{\mathbf{r}})\dot{\mathbf{r}}\right), &\text{(A.16)}\\
&= \kappa \frac{\partial^2}{\partial \alpha^2}\left(-\frac{H}{\sqrt{g}}\mathbf{n}\right), &\text{(A.17)}\\
&= \kappa \frac{\partial}{\partial \alpha}\left(-\frac{\partial (H\mathbf{n})}{\partial s} + \frac{\partial^2 s}{\partial \alpha^2}\frac{H}{g}\mathbf{n}\right). &\text{(A.18)}
\end{aligned}$$

Reporting the above results into (A.13), we obtain the following expression for the functional derivative

$$\begin{aligned}
\frac{\delta E_C}{\delta \mathbf{r}} &= \kappa \frac{\partial}{\partial \alpha}\left(-\frac{\partial H}{\partial s}\mathbf{n} + \frac{1}{2}H^2\mathbf{t}\right), &\text{(A.19)}\\
&= -\sqrt{g}\kappa\left(\frac{\partial^2 H}{\partial s^2} + \frac{1}{2}H^3\right)\mathbf{n}, &\text{(A.20)}
\end{aligned}$$

Therefore, the membrane curvature force is given by,

$$\mathbf{f}_C = \kappa\left(\frac{\partial^2 H}{\partial s^2} + \frac{1}{2}H^3\right)\mathbf{n}, \tag{A.21}$$

where the factor $\sqrt{g}$ disappears from the physical force, since this one must be defined as $\mathbf{f}_C = -(1/\sqrt{g})\delta E_C/\delta \mathbf{r}$, as explained at the end of the appendix.

The tension force

Finally Eq. (A.3) takes the following form

$$E_T = \int_0^1 \zeta(\mathbf{r})\sqrt{g}d\alpha, \tag{A.22}$$

whose functional derivative is,

$$\frac{\delta E_T}{\delta \mathbf{r}} = -\frac{\partial}{\partial \alpha}\frac{\partial e_T}{\partial \dot{\mathbf{r}}} \tag{A.23}$$

with $e_T = \zeta(\mathbf{r})\sqrt{g}$. Note that e_T depends neither on $\mathbf{r}$ nor on $\ddot{\mathbf{r}}$. We easily find

$$\begin{aligned}
\frac{\delta E_T}{\delta \mathbf{r}} &= -\frac{\partial}{\partial \alpha}\left(\zeta(\mathbf{r})\frac{\dot{\mathbf{r}}}{\sqrt{g}}\right), && \text{(A.24)}\\
&= -\frac{\partial}{\partial \alpha}\left(\zeta(\mathbf{r})\mathbf{t}\right), && \text{(A.25)}\\
&= -\sqrt{g}\frac{\partial}{\partial s}\left(\zeta(\mathbf{r})\mathbf{t}\right), && \text{(A.26)}\\
&= -\sqrt{g}\left[\frac{\partial \zeta}{\partial s}\mathbf{t} - \zeta H\mathbf{n}\right]. && \text{(A.27)}
\end{aligned}$$

The membrane force associated with the Lagrange multiplier is then,

$$\mathbf{f}_T = -\left[\zeta H\mathbf{n} - \frac{\partial \zeta}{\partial s}\mathbf{t}\right]. \tag{A.28}$$

By adding Eqs. (A.21) and (A.28), we obtain the total membrane force,

$$\mathbf{f} = \left[\kappa\left(\frac{\partial^2 H}{\partial s^2} + \frac{H^3}{2}\right) - H\zeta\right]\mathbf{n} + \frac{\partial \zeta}{\partial s}\mathbf{t}, \tag{A.29}$$

Let us briefly explain why the force is given by $-\mathbf{f} = -(1/\sqrt{g})\delta E_T/\delta\mathbf{r}$ (and not just $-\delta E_T/\delta\mathbf{r}$). The reason is that what matters is a physical displacement of the curve element ds and not $d\alpha$ (which is a mathematical arbitrary parametrization). If one performs directly the variation on the integral, one finds (according to the previous results)

$$\begin{aligned}
\delta E &= -\int\left[\left[\kappa\left(\frac{\partial^2 H}{\partial s^2} + \frac{H^3}{2}\right) - H\zeta\right]\mathbf{n} + \frac{\partial \zeta}{\partial s}\mathbf{t}\right]\sqrt{g}d\alpha\delta\mathbf{r}, && \text{(A.30)}\\
&= -\int\left[\left[\kappa\left(\frac{\partial^2 H}{\partial s^2} + \frac{H^3}{2}\right) - H\zeta\right]\mathbf{n} + \frac{\partial \zeta}{\partial s}\mathbf{t}\right]ds\delta\mathbf{r} && \text{(A.31)}\\
&= -\int \mathbf{f}ds\delta\mathbf{r}. && \text{(A.32)}
\end{aligned}$$

B. DIMENSIONLIZING THE HYDRODYNAMICAL EQUATIONS

The Navier-Stokes equation, gouverning the flow of an incompressible Newtonian fluid, is given by:

$$\rho\left(\frac{\partial \mathbf{v}(\mathbf{r})}{\partial t}+\mathbf{v}(\mathbf{r})\cdot\nabla\mathbf{v}(\mathbf{r})\right)=-\nabla p(\mathbf{r})+\eta\nabla^2\mathbf{v}(\mathbf{r})+\mathbf{f}(\mathbf{r}), \tag{B.1}$$

where ρ and η are, respectively, the mass density and the viscosity of the fluid. The unknown solutions of this equation are the velocity $\mathbf{u}$ and the pressure p fields. $\mathbf{f}$ in the RHS of Eq. (B.1) represents an external force applied on the fluid. Hereafter we consider the situation that the flow of the considered fluid is disturbed at a point $\mathbf{r}$ by a singular force exerted by a point $\mathbf{r}'$ belonging to the vesicle membrane.

We write all the variables appearing in Eq. (B.1) in a dimensionless form:

- $\mathbf{r}^*=\mathbf{r}/R_0$,
- $t^*=t/T$,
- $\mathbf{v}^*=\mathbf{v}/U$,
- $p^*=pR_0/\eta U$,

where we used a characteristic length scale R_0 (here the effective radius of a vesicle), a characteristic time scale T and a characteristic velocity U of the flow. Substituting all these new variables in Eq. (B.1) and multiplying it by the quantity $(R_0^2/\eta U)$ gives:

$$\left(\frac{\rho R_0^2}{\eta T}\right)\frac{\partial \mathbf{v}^*}{\partial t^*}+\left(\frac{\rho U R_0}{\eta}\right)\mathbf{v}^*\cdot\nabla^*\mathbf{v}^*=-\nabla^* p^*+\nabla^{*2}\mathbf{v}^*, \tag{B.2}$$

which can be rewritten in the form:

$$\beta\frac{\partial \mathbf{v}^*}{\partial t^*}+\mathrm{Re}\,(\mathbf{v}^*\cdot\nabla^*\mathbf{v}^*)=-\nabla^* p^*+\nabla^{*2}\mathbf{v}^*, \tag{B.3}$$

with β is the *frequency number* and Re is the *Reynolds number*. We can take $T=R_0/U$ and thus $\beta=\mathrm{Re}$.

Now, we write the membrane force in a dimensionless form. The expression of the membrane force is given by:

$$\mathbf{f} = \left[\kappa\left(\frac{\partial^2 H}{\partial s^2} + \frac{H^3}{2}\right)\mathbf{n} + \frac{\partial \zeta}{\partial s}\mathbf{t} - \zeta H\mathbf{n}\right]\delta(\mathbf{r} - \mathbf{r}'). \tag{B.4}$$

where κ is the membrane rigidity, H the membrane local curvature and ζ a local Lagrange multiplier (or tension). $\mathbf{n}$ and $\mathbf{t}$ are respectively the unit normal and tangential vectors. This force has no zero value just on a point belonging to the vesicle membrane $\mathbf{r}' \in \partial\Omega$. We rewrite the variables in Eq. (B.4) in a dimensionless form:

- $H^* = H/H_0 = HR_0$,
- $s^* = s/R_0$,
- $\zeta^* = \zeta/\Gamma$ with Γ is the spring constant (see chapter *Model*),
- $\delta(\mathbf{r} - \mathbf{r}') = \delta(R_0(\mathbf{r}^* - \mathbf{r}'^*)) = \delta(\mathbf{r}^* - \mathbf{r}'^*)/R_0$[1],

Substituting all these variables in Eq. (B.4), multiplying it by $(R_0^2/\eta U)$ (as we did above) and taking $U/R_0 = \gamma$, with γ is the shear rate, this gives:

$$\begin{aligned}\frac{R_0^2}{\eta U}\mathbf{f} &= \frac{\kappa}{\eta\gamma R_0^3}\left(\frac{\partial^2 H^*}{\partial s^{*2}} + \frac{H^{*3}}{2}\right)\delta(\mathbf{r}^* - \mathbf{r}'^*)\mathbf{n} \\ &\quad + \frac{\Gamma}{\eta\gamma R_0}\left(\frac{\partial \zeta^*}{\partial s^*}\mathbf{t} - H^*\zeta^*\mathbf{n}\right)\delta(\mathbf{r}^* - \mathbf{r}'^*),\end{aligned} \tag{B.5}$$

where appear:

- The *capillary number*:

$$Ca = \frac{\eta\gamma R_0^3}{\kappa} \tag{B.6}$$

  that gives the ratio between the shear time $(1/\gamma)$ and the characteristic time needed by a vesicle (at an out-of-equilibrium state) to relax to its equilibrium shape,

- The *tension number*:

$$Ca_s = \frac{\eta\gamma R_0}{\Gamma} \tag{B.7}$$

  which is the ratio between the spring relaxation time and the shear time.

[1] Using one property of the Dirac's delta function $\delta(ax) = \frac{1}{|a|}\delta(x)$

Finally the dimensionless Navier-Stokes equation, with the membrane force term, is given by:

$$\begin{aligned} \mathrm{Re}\left(\frac{\partial \mathbf{v}^*}{\partial t^*} + \mathbf{v}^* \cdot \nabla^* \mathbf{v}^*\right) &= -\nabla^* p^* + \nabla^{*2}\mathbf{v}^* \\ &+ \frac{1}{Ca}\left(\frac{\partial^2 H^*}{\partial s^{*2}} + \frac{H^{*3}}{2}\right)\delta(\mathbf{r}^* - \mathbf{r}'^*)\mathbf{n} \\ &+ \frac{1}{Ca_s}\left(\frac{\partial \zeta^*}{\partial s^*}\mathbf{t} - H^*\zeta^*\mathbf{n}\right)\delta(\mathbf{r}^* - \mathbf{r}'^*). \end{aligned} \tag{B.8}$$

and its corresponding dimensionless Stokes equation by:

$$\begin{aligned} -\nabla^* p^* + \nabla^{*2}\mathbf{v}^* &= -\frac{1}{Ca}\left(\frac{\partial^2 H^*}{\partial s^{*2}} + \frac{H^{*3}}{2}\right)\delta(\mathbf{r}^* - \mathbf{r}'^*)\mathbf{n} \\ &- \frac{1}{Ca_s}\left(\frac{\partial \zeta^*}{\partial s^*}\mathbf{t} - H^*\zeta^*\mathbf{n}\right)\delta(\mathbf{r}^* - \mathbf{r}'^*). \end{aligned} \tag{B.9}$$

C. BOUNDARY INTEGRAL FORMULATION

Here we present the main steps needed to derive the boundary integral equation, giving the velocity field on the membrane of a vesicle placed in unbounded Stokes flow.

Flow due to a singular force

Exerting a singular unit force $\mathbf{f}$ at the point $\mathbf{r}'$, locally in the j-direction, induces at another point $\mathbf{r}$ of the fluid:

- The velocity in the i-direction:

$$u_i^*(\mathbf{r}) = \frac{1}{4\pi\eta^*} G_{ij}(\mathbf{r}, \mathbf{r}') f_j, \tag{C.1}$$

  where η^* is the viscosity of the considered fluid.

- The pressure:

$$p^*(\mathbf{r}) = \frac{1}{4\pi} Q_j(\mathbf{r}, \mathbf{r}') f_j, \tag{C.2}$$

- The stress tensor:

$$\sigma_{ij}^*(\mathbf{r}) = \frac{1}{4\pi} T_{ijk}(\mathbf{r}, \mathbf{r}') f_j, \tag{C.3}$$

G_{ij} and Q_j are *Green's functions* for a unbounded Stokes flow and are by definition solutions of the following set of equations:

$$\begin{aligned} \partial_{jj} G_{ik}(\mathbf{r}, \mathbf{r}') - \partial_i Q_k(\mathbf{r}, \mathbf{r}') &= -\delta_{ik}\delta(\mathbf{r}, \mathbf{r}'), \\ \partial_i G_{ik}(\mathbf{r}, \mathbf{r}') &= 0, \end{aligned} \tag{C.4}$$

where δ_{ij} is the Kronecker's delta and δ is the Dirac's delta function. T_{ijk} is the Green's function associated to the stress tensor and it is given by:

$$T_{ijk}(\mathbf{r}, \mathbf{r}') = (\partial_j G_{ik}(\mathbf{r}, \mathbf{r}') + \partial_i G_{jk}(\mathbf{r}, \mathbf{r}')) - Q_k(\mathbf{r}, \mathbf{r}')\delta_{ij}, \tag{C.5}$$

and its derivation satisfies:

$$\partial_j T_{ijk}(\mathbf{r}, \mathbf{r}') = -\delta_{ij}\delta(\mathbf{r}, \mathbf{r}'), \tag{C.6}$$

which allows to rewritte Eqs. C.4 in the form:

$$\begin{aligned} \partial_j T_{ijk}(\mathbf{r},\mathbf{r}') &= -\delta_{ij}\delta(\mathbf{r},\mathbf{r}'), \\ \partial_i G_{ik}(\mathbf{r},\mathbf{r}') &= 0. \end{aligned} \tag{C.7}$$

For the two-dimensional unbouned Stokes flow (i.e. a two-dimensionl free space) the Green's functions have the following expressions:

$$G_{ij} = -\delta_{ij} lnr + \frac{r_i r_j}{r^2}, \tag{C.8}$$

$$T_{ijk} = -4\frac{r_i r_j r_k}{r^4}, \tag{C.9}$$

$$Q_j = 2\frac{r_j}{r^2}. \tag{C.10}$$

where $r \equiv |\mathbf{r}-\mathbf{r}'|$ and r_i is the i^{th} component of the vector $\mathbf{r}-\mathbf{r}'$.

Flow of the external fluid

Now consider the Stokes equations of the vesicle external fluid:

$$\begin{aligned} \partial_j \sigma_{ij}^{ext}(\mathbf{r}) &= 0, \\ \partial_i v_i^{ext}(\mathbf{r}) &= 0. \end{aligned} \tag{C.11}$$

where $\mathbf{r} \in \Omega_{ext}$ and $\sigma_{ij}^{ext} = \eta^{ext}(\partial_i v_j^{ext} + \partial_j v_i^{ext}) - p^{ext}\delta_{ij}$ is the stress tensor.

Taking the divergence of the products $(\eta^* u_i^*(\mathbf{r}')\sigma_{ij}^{ext}(\mathbf{r}'))$ and $(\eta v_i(\mathbf{r}')\sigma_{ij}^*(\mathbf{r}'))$ and substracting one from another gives:

$$\partial_j(\eta^* u_i^*(\mathbf{r}')\sigma_{ij}^{ext}(\mathbf{r}')) - \partial_j(\eta v_i(\mathbf{r}')\sigma_{ij}^*(\mathbf{r}')) = \eta v_i(\mathbf{r}')\delta_{ij}\delta(\mathbf{r}',\mathbf{r}). \tag{C.12}$$

Substituting u_i^* and σ_{ij}^* by their respective expressions in Eq. C.12, integrating over the whole external fluid domaine Ω_{ext} and applying the *divergence theorem* on the membrane $\partial\Omega$ gives:

$$\begin{aligned} \int_{\Omega_{ext}} \eta_{ext} v_i(\mathbf{r}')\delta_{ij}\delta(\mathbf{r}',\mathbf{r})dv(\mathbf{r}') = &-\frac{1}{4\pi}\int_{\partial\Omega} G_{ij}(\mathbf{r},\mathbf{r}')\sigma_{ij}^{ext}(\mathbf{r}')n(\mathbf{r}')ds(\mathbf{r}') \\ &+\frac{1}{4\pi}\int_{\partial\Omega} v_i(\mathbf{r}')T_{ijk}(\mathbf{r},\mathbf{r}')n(\mathbf{r}')ds(\mathbf{r}') \end{aligned} \tag{C.13}$$

We have:

$$\int_{\Omega_{ext}} v_i(\mathbf{r}')\delta_{ij}\delta(\mathbf{r}',\mathbf{r})dv(\mathbf{r}') = \Delta v_j(\mathbf{r}') \tag{C.14}$$

with

$$\Delta = \begin{cases} 1 & \mathbf{r} \in \Omega_{\text{ext}} \\ 0 & \mathbf{r} \in \Omega_{\text{int}} \\ \frac{1}{2} & \mathbf{r} \in \partial\Omega \end{cases} \tag{C.15}$$

$$\eta^{ext}\Delta v_j(\mathbf{r}') = -\frac{1}{4\pi}\int_{\partial\Omega} G_{ij}(\mathbf{r},\mathbf{r}')\sigma_{ij}^{ext}(\mathbf{r}')n(\mathbf{r}')ds(\mathbf{r}') + \frac{\eta^{ext}}{4\pi}\int_{\partial\Omega} v_i(\mathbf{r}')T_{ijk}(\mathbf{r},\mathbf{r}')n(\mathbf{r}')ds(\mathbf{r}') \quad \text{(C.16)}$$

Flow of the internal fluid

Following the same procedure we derive the boundary integral equation for the the internal fluid flow:

$$\eta^{int}\Delta' v_j(\mathbf{r}') = -\frac{1}{4\pi}\int_{\partial\Omega} G_{ij}(\mathbf{r},\mathbf{r}')\sigma_{ij}^{int}(\mathbf{r}')n(\mathbf{r}')ds(\mathbf{r}') + \frac{\eta^{int}}{4\pi}\int_{\partial\Omega} v_i(\mathbf{r}')T_{ijk}(\mathbf{r},\mathbf{r}')n(\mathbf{r}')ds(\mathbf{r}') \quad \text{(C.17)}$$

with

$$\Delta' = \begin{cases} 1 & \mathbf{r}\in\Omega_{\text{int}} \\ 0 & \mathbf{r}\in\Omega_{\text{ext}} \\ \frac{1}{2} & \mathbf{r}\in\partial\Omega \end{cases} \quad \text{(C.18)}$$

The boundary integral equation at the membrane

At a point belonging to the membrane $\mathbf{r}\in\partial\Omega_m$, we have:

$$\frac{1}{2}v_k^{ext}(\mathbf{r}) = -\frac{1}{4\pi\eta_{ext}}\int_{\partial\Omega_m} G_{ik}(\mathbf{r},\mathbf{r}')\sigma_{ij}^{ext}(\mathbf{r}')n_j(\mathbf{r}')dS(\mathbf{r}') + \frac{1}{4\pi}\int_{\partial\Omega_m} v_i^{ext}(\mathbf{r}')T_{ijk}(\mathbf{r}',\mathbf{r})n_j(\mathbf{r}')dS(\mathbf{r}') \quad \text{(C.19)}$$

and

$$\frac{1}{2}v_k^{int}(\mathbf{r}) = \frac{1}{4\pi\eta_{int}}\int_{\partial\Omega_m} G_{ik}(\mathbf{r},\mathbf{r}')\sigma_{ij}^{int}(\mathbf{r}')n_j(\mathbf{r}')dS(\mathbf{r}') - \frac{1}{4\pi}\int_{\partial\Omega_m} v_i^{int}(\mathbf{r}')T_{ijk}(\mathbf{r}-\mathbf{r}')n_j(\mathbf{r}')dS(\mathbf{r}') \quad \text{(C.20)}$$

Taking advantage of the continuity velocity boundary condition on the membrane $v^{ext} = v^{int} = v$ and after addition of Eqs. (C.19) and (C.20):

$$\frac{\eta_{int}+\eta_{ext}}{2}v_k(\mathbf{r}) = -\int_{\partial\Omega_m} G_{ik}(\mathbf{r}-\mathbf{r}')\left[\sigma_{ij}^{ext}(\mathbf{r}') - \sigma_{ij}^{int}(\mathbf{r}')\right]n_j(\mathbf{r}')dS(\mathbf{r}') + (\eta_{int}-\eta_{ext})\int_{\partial\Omega_m} v_i(\mathbf{r}')T_{ijk}(\mathbf{r}',\mathbf{r})n_j(\mathbf{r}')dS(\mathbf{r}') \quad \text{(C.21)}$$

Expressing the stress jump across the membrane in term of the membrane force $\left[\sigma_{ij}^{ext}(\mathbf{r}') - \sigma_{ij}^{int}(\mathbf{r}')\right] n_j(\mathbf{r}') = -f_i(\mathbf{r}')$, the velocity field at the membrane is then given by:

$$\frac{\eta_{int} + \eta_{ext}}{2} v_k(\mathbf{r}) = \int_{\partial\Omega_m} G_{ik}(\mathbf{r}, \mathbf{r}') f_i n_j(\mathbf{r}') dS(\mathbf{r}') + (\eta_{int} - \eta_{ext}) \int_{\partial\Omega_m} v_i(\mathbf{r}') T_{ijk}(\mathbf{r}', \mathbf{r}) n_j(\mathbf{r}') dS(\mathbf{r}') \tag{C.22}$$

This is the integral equation that need to be solved to track the membrane dynamics. If we consider the case of a vescile placed in a semi-infinite fluid bounded by an infinite plane steady wall, then all the above mentioned Green's functions G_{ij}, Q_j, T_{ijk} have to be substituted by the ones taking into aacount the existence of the wall by fullfilling zero velocity field on the wall [**?**].

BIBLIOGRAPHY

[1] P. G. de Gennes, *Rev. Mod. Phys.* **57**, 827 (1985).

[2] H. A. Stone, *Annu. Rev. Fluid Mech.* **26**, 65 (1994).

[3] R. Lipowsky and E. Sackmann, *Structure and Dynamics of Membranes, from Cells to Vesicles*, North-Holland, 1995.

[4] P. L. Luisi and P. Walde, *Giant Vesicles (Perspectives in Supramolecular Chemistry)*, Wiley, 2000.

[5] C. Pozrikidis, *Modeling and Simulation of Capsules and Biological Cells*, CRC Press, 2003.

[6] S. S. Shevkoplyas, T. Yoshida, L. L. Munn, and M. W. Bitensky, *Analytical Chemistry* **77**, 933 (2005).

[7] N. Pamme, *Lab on a Chip* **7**, 1644 (2007).

[8] Z. Wu, B. Willing, J. Bjerketorp, J. K. Jansson, and K. Hjort, *Lab on a Chip* **9**, 1193 (2009).

[9] S. R. Quake and A. Scherer, *Science* **290**, 1536 (2000).

[10] G. M. Whitesides, *Nature* **442**, 368 (2006).

[11] M. Wilson, *Physics Today* (2006).

[12] S. R. Keller and R. Skalak, *J. Fluid Mech.* **120**, 27 (1982).

[13] J. Beaucourt, F. Rioual, T. Séon, T. Biben, and C. Misbah, *Phys. Rev. E* **69**, 011906 (2004).

[14] M.-A. Mader, V. Vitkova, M. Abkarian, A. Viallat, and T. Podgorski, *Eur. Phys. J. E* **19**, 389 (2006).

[15] V. Kantsler and V. Steinberg, *Phys. Rev. Lett.* **95**, 258101 (2005).

[16] V. Kantsler and V. Steinberg, *Phys. Rev. Lett.* **96**, 036001 (2006).

[17] C. Misbah, *Phys. Rev. Lett.* **96**, 028104 (2006).

[18] P. Olla, *J. Phys. II France* **7**, 1533 (1997).

[19] I. Cantat and C. Misbah, *Phys. Rev. Lett.* **83**, 880 (1999).

[20] S. Sukumaran and U. Seifert, *Phys. Rev. E* **64**, 011916 (2001).

[21] M. Abkarian, C. Lartigue, and A. Viallat., *Phys. Rev. Lett.* **88**, 8103 (2002).

[22] N. Callens, C. Minetti, G. Coupier, M.-A. Mader, F. Dubois, and C. Misbah, *Europhys. Lett.* **83**, 24002 (2008).

[23] G. Danker, T. Biben, T. Podgorski, C. Verdier, and C. Misbah, *Physical Review E (Statistical, Nonlinear, and Soft Matter Physics)* **76**, 041905 (2007).

[24] V. V. Lebedev, K. S. Turitsyn, and S. S. Vergeles, *Phys. Rev. Lett.* **99**, 218101 (2007).

[25] K. H. de Haas, C. Blom, D. van den Ende, M. H. G. Duits, and J. Mellema, *Physical Review E (Statistical, Nonlinear, and Soft Matter Physics)* **56**, 7132 (1997).

[26] J. Deschamps, V. Kantsler, and V. Steinberg, *Physical Review Letters* **102**, 118105 (2009).

[27] M. Abkarian and A. Viallat, *Biophysical Journal* **89**, 1055 (2005).

[28] R. Bruinsma, *Physica A* **234**, 249 (1996).

[29] V. Vitkova, M. Mader, and T. Podgorski, *Europhys. Lett.* **68**, 398 (2004).

[30] H. Noguchi and G. Gompper, *PNAS* **102**, 14159 (2005).

[31] H. Noguchi and G. Gompper, *J. Phys.: Condens. Matter* **17**, S3439 (2005).

[32] E. A. Disalvo and S. A. Simon, *Permeability and Stability of Lipid Bilayers*, CRC Press, 1995.

[33] W. Helfrich, *Z. Naturforsch. A* **28c**, 693 (1973).

[34] O.-Y. Zhong-can and W. Helfrich, *Phys. Rev. A* **39**, 5280 (1989).

[35] A. Laadhari, C. Misbah, and P. Saramito, *(unpublished)* .

[36] U. Seifert, K. Berndl, and R. Lipowsky, *Phys. Rev. A* **44**, 1182 (1991).

[37] B. Alberts, A. Johnson, J. Lewis, M. Raff, K. Roberts, and P. Walter, *Molecular Biology of the Cell*, Garland, New York, 2001.

[38] E. M. Purcell, *Am. J. Phys.* **45**, 3 (1977).

[39] J. Happel and H. Brenner, *Low Reynolds number hydrodynamics: with special applications to particulate media*, Englewood Cliffs, NJ: Prentice-Hall, 1965.

[40] I. Cantat, K. Kassner, and C. Misbah, *Eur. Phys. J. E* **10**, 175 (2003).

[41] C. Pozrikidis, *Boundary Integral and Singularity Methods for Linearized Viscous Flow*, Cambridge University Press, Cambridge, 1992.

[42] C. Pozrikidis, *A practical Guide to Boundary Element Methods with the Software Library BEMLIB*, Chapman & Hall/CRC, 2002.

[43] M. Kraus, W. Wintz, U. Seifert, and R. Lipowsky, *Phys. Rev. Lett.* **77**, 3685 (1996).

[44] U. Frisch, D. d'Humieres, B. Hasslacher, P. Lallemand, Y. Pomeau, and J. Rivet, *Complex Syst* **1**, 649 (1987).

[45] D. Raabe, *Modelling Simul. Mater. Sci. Eng.* **12**, R13 (2004).

[46] S. Succi, *The Lattice Boltzmann Equation for Fluid Mechanics and Beyond*, Clarendon Press, 2001.

[47] M. C. Sukop and J. D. T. Thorne, *Lattice Boltzmann Modeling. An Introductio for Geoscientists and Engineers*, Springer, 2006.

[48] P. E. Bhatnagar, P. E. Gross, and M. Krook, *Phys. Rev.* **94**, 511 (1954).

[49] A. J. C. Ladd, *J. Fluid Mech.* **271**, 285 (1994).

[50] C. S. Peskin, *Journal of Computational Physics* **25**, 220 (1977).

[51] R. Mittal and G. Iaccarino, *Annu. Rev. Fluid Mech.* **37**, 239 (2005).

[52] C. S. Peskin, *Acta Numerica* **11**, 479 (2002).

[53] U. Seifert, *Euro. Phys. J. B* **8**, 405 (1999).

[54] G. Cox, *J. Fluid Mech.* **37**, 601 (1969).

[55] N. A. Frankel and A. Acrivos, *J. Fluid Mech.* **44**, 65 (1970).

[56] D. Barthes-Biesel and J. M. Rallison, *J. Fluid Mech.* **113**, 251 (1981).

[57] S. Kessler, R. Finken, and U. Seifert, *J. Fluid Mech.* , 605 (2008).

[58] P. M. Vlahovska and R. S. Gracia, *Phys. Rev. E* **75**, 016313 (2007).

[59] H. Lamb, *Hydrodynamics*, Cambridge University Press, 6th edition, 1932.

[60] H. Noguchi and G. Gompper, *Phys. Rev. Lett.* **98**, 128103 (2007).

[61] T. Biben and C. Misbah, *Phys. Rev. E* **67**, 031908 (2003).

[62] F. Rioual, T. Biben, and C. Misbah, *Phys. Rev. E* **69**, 061914 (2004).

[63] G. B. Jeffery, *Proc. Roy. Soc. London Ser. A* **102**, 161 (1922).

[64] M. Abkarian, M. Faivre, and A. Viallat, *Phys. Rev. Lett.* **98**, 188302 (2007).

[65] M. C. T. Wilson, P. H. Gaskell, and M. D. Savage, *Physics of Fluids* **17**, 093601 (2005).

[66] E.-J. Ding and C. K. Aidun, *J. Fluid Mech.* **423**, 317 (2000).

[67] H. B. Li, H. H. Yi, X. W. Shan, and H. P. Fang, *EPL (Europhysics Letters)* **81**, 54002 (2008).

[68] P. J. A. Janssen and P. D. Anderson, *Physics of Fluids* **19**, 043602 (2007).

[69] H. Nirschl, H. A. Dwyer, and V. Denk, *J. Fluid Mech* **285**, 273 (1995).

[70] R. Fahraeus and T. Lindqvist, *Am. J. Physiol.* **96**, 562 (1931).

[71] L. G. Leal, *Annu. Rev. Fluid Mech.* **12**, 435 (1980).

[72] G. Danker, P. M. Vlahovska, and C. Misbah, *Physical Review Letters* **102**, 148102 (2009).

[73] G. Coupier, B. Kaoui, T. Podgorski, and C. Misbah, *Physics of Fluids* **20**, 111702 (2008).

[74] R. Skalak and P.-I. Branemark, *Science* **164**, 717 (1969).

[75] C. Quéguiner and D. Barthès-Biesel, *J. Fluid Mech.* **348**, 349 (1997).

[76] T. W. Secomb, R. Skalak, N. Ozkaya, and J. F. Gross, *J. Fluid Mech* **163**, 405 (1986).

[77] J. Feng, H. H. Hu, and D. D. Joseph, *J. Fluid Mech.* **277**, 271 (1994).

[78] A. Arend, J. Leonhard, D. Kienle, and W. Zimmermann, *(unpublished)* .

[79] M. I. Angelova, S. Soleau, P. Meleard, J. F. Faucon, and P. Bothorel, *Progr. Colloid. Polym. Sci.* **89**, 127 (1992).

[80] F. M. White, *Viscous Fluid Flow*, McGraw-Hill, New York, 1991.

[81] B. Kaoui, G. H. Ristow, I. Cantat, C. Misbah, and W. Zimmermann, *Phys. Rev. E* **77**, 021903 (2008).